DEVELOPMENT AND CHARACTERISATION OF A HYBRID MOCK CIRCULATORY LOOP WITH BARORECEPTOR RESPONSE

A thesis submitted for the degree of

DOCTOR OF PHILOSOPHY

by

FEMKE CAPPON

Biomedical Engineering

Department of Mechanical and Aerospace Engineering

College of Engineering, Design and Physical Sciences

Brunel University

May 2024

Abstract

In the UK alone, as of April 2020, 340 patients awaited a heart transplant, but only 172 transplants were available. Ventricular Assist Devices (VADs), which support the heart's pumping function and serve as a bridge-to-transplant or permanent support for heart failure patients, offer a solution. The Mock Circulatory Loop (MCL) facilitates the design, development, and evaluation of VADs by simulating the native cardiovascular system (CVS). However, current MCLs often lack the capability to simulate critical pressure regulatory mechanisms, specifically the baroreflex response, which adjusts cardiac output and systemic resistance to maintain CVS pressure. This thesis seeks to enhance MCL design by incorporating the baroreflex response. A control system, based on the velocity and acceleration of a linear motor, was designed to regulate heart rate in the left ventricle simulator, achieving a range of $0 - 120bpm$. A physical automated resistor, capable of adjusting resistance within the physiological range of $9 - 20.0mmHgmin/L$, was introduced. Following this, a numerical model of the baroreflex response was integrated with the hydraulic setup. Testing of the enhanced MCL under three dynamic scenarios - clamping, volume addition, and volume reduction - revealed promising outcomes. During the clamping test, the MCL sustained pressure for the initial $15s$ post-clamping. In the volume reduction experiment, removing $2L$ of water led to a mere $6mmHg$ drop in pressure, while adding $2L$ resulted in just a $3mmHg$ increase. The developed MCL offers an enhanced platform to test VADs, from resistance shifts and pressure fluctuations to the baroreflex mechanisms. Research following from this thesis should focus on improving the left ventricle simulator to control cardiac contractility, further integrating it into the MCL.

Acknowledgements

Here I am, writing the last page of this book, marking a journey that spanned more than three years of my life. I am deeply grateful to my mentors and friends who guided me towards this path long before this journey began. Without your lessons, I would not have embarked on this journey in the first place.

I want to extend my thanks to my academic supervisors, Dr. Xinli Du and Prof. Ashraf W. Khir, for their support and mentoring throughout my research. Their guidance kept me on track and helped me steer in the right direction when my mind wandered. Additionally, I express my gratitude to my supervisors and funders at MagAssist for providing me the opportunity to learn with them in their company for two months. Thank you for making me feel at home away from home.

The further and longer I ventured from my home in The Netherlands, the more friends became like family. To all those I met along the way, thank you. Whether we crossed paths briefly or you stayed with me longer, your unwavering support and lessons have been invaluable. I am incredibly grateful for every single one of you.

I want to extend a special thank you to my dear friends Jenny Starzetz and Ben Evans. Your endless support and social distractions have been a lifesaver. Thank you for taking care of me when I was both literally and figuratively broken. Your home has always been open to me in good times and bad, and I can never thank you enough for that.

Thank you to my friends Ioana Cretu and Barbara Draghi; you were there for me when I needed you most. And to my dear friends and colleagues Angel Naveenathayalan, Alessandro Giudici, Ylenia Rotalinti, Enrico Urru, Nauman Hafeez, and Shima Abdullateef, all of whom are incredible individuals: thank you for your friendship, support, lessons, and patience throughout this journey.

I would like to thank my friends back home, upon whom I know I can always rely, no matter where I am. Thank you to my family; your frequent visits to the big city always lifted

my spirits. My grandma who goes above and beyond trying to understand my academic journey. And above all, thank you, Aaron, for keeping my feet on the ground. Your love and support, although only halfway through my journey, have been invaluable. Thank you for your incredible patience on the challenging days. I look forward to the future to come.

Contents

List of Figures

List of Tables

List of Acronyms

η viscosity [Pas].

E_{es} Elasticity of the left ventricle [$mmHg/mL$].

E_{lv} cardiac contractility of the left ventricle [$mmHg/mL$].

I Inertance [$mHgmL/s^2$].

L length [mm].

P_{es} end-systolic pressure [$mmHg$].

R_{ep} resistanceextrasplanich pheriperal [$mmHgmin/L$].

R_{sp} resistance splanich peripheral [$mmHgmin/L$].

T_s heart period sympathetic neurological pathway [s].

T_v heart period vagal neurological pathway [s].

V Voltage [V].

f_{cs} the frequency of spikes in the afferent pathway [$spikes/s$].

f_{es} the frequency of spikes in the efferent sympathetic nerves [$spikes/s$].

f_{ev} the frequency of spikes in the efferent vagal fibers [$spikes/s$].

r radius [mm].

CAD cardiac assist devices.

CVD cardiovascular disease.

CVS cardio vascular system.

ECMO extracorporeal membrane oxygenation.

EDP end-diastolic pressure.

EDV end-diastolic volume.

ESPVR end-systolic pressure volume relationship.

ESV end-systolic volume.

GPR gaussian process regression.

H-MCL hybrid mock circulatory loop.

HR heart rate.

IABP intra aortic balloon pump.

MAE mean absolute error.

MCL mock circulatory loop.

MSE mean squared error.

PV-loop pressure-volume loop.

PVR pulmonary vascular resistance.

RMSE root mean square error.

SBP systolic blood pressure.

SV stroke volume.

SVR systemic vascular resistance.

TAH total artificial heart.

VAD ventricular assist device.

VI Virtual Instrument.

Chapter 1

Introduction

Heart failure, a widespread health issue affecting millions of individuals worldwide, has emerged as a global pandemic (figure 1.1).[1] While the condition primarily affects individuals aged 65 years and older, it poses a significant risk to people of all age groups due to various causes such as, abnormal heart rhythms, coronary artery disease, high blood pressure, valve disease, diabetes, and obesity. In August 2022, England witnessed a record-breaking cardiac waiting list of 346,000 individuals. This increased demand has resulted in extended waiting periods, with over 7,000 people waiting for a heart procedure for more than a year [2].The substantial financial implications of this situation extend to both the National Health Service (NHS) and society at large. In England, the decline of cardiovascular disease (CVD) is estimated to cost a significant £13 billion annually, while social care costs would reach £1.5 billion. Moreover, the value of informal care is projected to be approximately £8 billion, and the quantified loss of "quality adjusted life years" would equate to an estimated £32 billion [3]. Some people with severe progressive heart failure cannot be helped with any medication or dietary. For this group of patients their only treatment option would be a heart transplant. However, as of April 2021, in the UK solely, 304 patients were on the active heart transplant list, while only 159 transplants were available [4]. The number of patients referred for heart transplants continues to grow and, inevitably, the waiting time. Hence, extensive research efforts have been directed towards the advancement of cardiac assist devices (CADs) as an alternative for end-stage heart failure patients.

[1] Part of this chapter is published in F. Cappon, T. Wu, T. Papaioannou, X. Du, P.-L. Hsu, and A. W. Khir, "Mock circulatory loops used for testing cardiac assist devices: A review of computational and experimental models," The International Journal of Artificial Organs, vol. 44, no. 11, pp. 793–806,2021 [1]

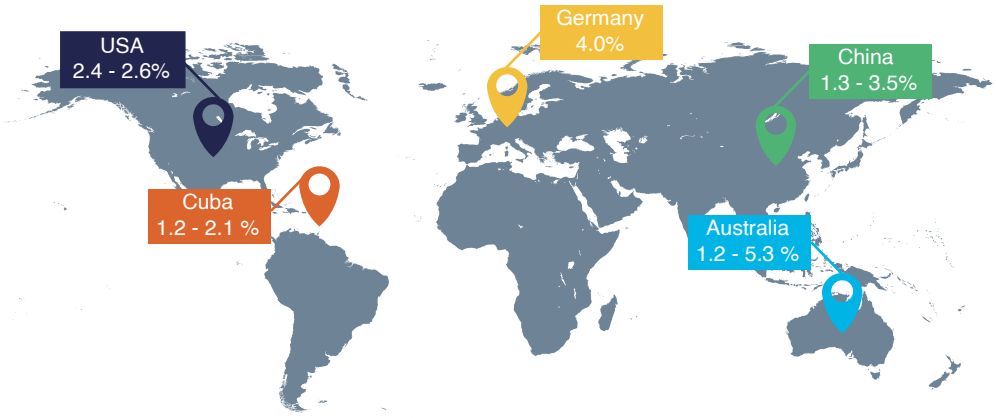

Figure 1.1: Percentage of heart failure in the population globally [1].

CADs are commonly classified based on the duration of support they provide. Several examples illustrated in figure 1.2. Certain devices, for example, the intra-aortic balloon pump (IABP) and extracorporeal membrane oxygenation ECMO, are employed for short-term stabilisation, spanning from hours to weeks, typically within one to four weeks following an operation [5]. Alternatively, CADs, such as the left ventricle assist device LVAD, may serve as a bridge-to-transplant for patients awaiting a heart transplant, with an average duration of up to two years. However, a unmet goal remains the development of a long-term or permanent cardiac support.

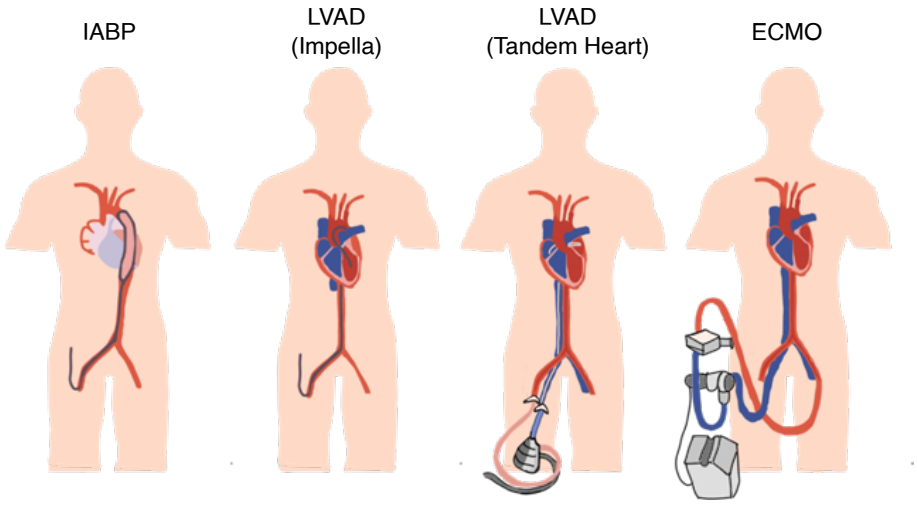

Figure 1.2: Different types of CAD, the IABP, the Impella left VAD, the TandemHeart left VAD and the ECMO (modified from [6])

An example of a short-term CAD is extracorporeal membrane oxygenation (ECMO), used for patients experiencing heart and lung failure. During ECMO support, blood is continuously withdrawn from the patient's body and passed through a sequence of de-

vices that enrich it with oxygen and eliminate carbon dioxide. Subsequently, the machine returns the oxygenated blood back into the patient's circulatory system. ECMO serves as a valuable tool in managing severe cardiac and pulmonary dysfunction in both adults and children. It finds application in various scenarios such as cardiogenic shock, post-cardiac surgery, and post-heart transplant, among others [7].

Another example of a short-term CAD is the intra-aortic balloon pump (IABP), which is inserted into the descending aorta. The balloon is inflated during ventricular diastole to increase diastolic pressure, coronary blood flow, and systemic perfusion. Conversely, it is deflated during systole to decrease cardiac afterload and increase cardiac output [8]. The IABP is commonly used in cases of acute congestive heart failure, arrhythmias, heart attacks, and coronary artery disease.

Moreover, the Total Artificial Hearts (TAH) is a CAD that replaces the lower chambers or ventricles of the native heart. Once implanted, the TAH pumps blood throughout the circulation, restoring a healthy circulation. The TAH is used to sustain a patients overall health until they become eligible for a heart transplant. A TAH can be used for patients with a congenital heart defect present at birth or the progressive decline of heart function resulting from heart failure.

Implantable Ventricular Assist Devices (VADs) assist the hearts pumping function by working alongside the native heart. VADs are used as a bridge-to-transplant or permanent support for severe heart failure patients with cardiogenic shock and multiple organ dysfunctions [9]. VADs support individuals whose heart has insufficient strength to pump. These implantable pumps play a crucial role in circulating the blood throughout the body. They have substantially improved survival rates for patients who are awaiting heart transplantation [10]. Due to recent technical advances of VAD, destination therapy became a genuine long-term solution for heart failure patients [11]. However, serious adverse events remain high after VAD implementation: between 2015-2019 causes of death in patients with VAD support were, for example, due to multi system organ failure (16.4%), neurologic dysfunction (15.6%) and heart failure (12.5%) [12]. A full overview can be seen in figure 1.3. Thus, ongoing research is needed to enhance VAD as a solution to the increasing donor shortage.

The Mock Circulatory Loop (MCL) is an essential component in the design, development, and in vitro evaluation of VADs and other CADs.

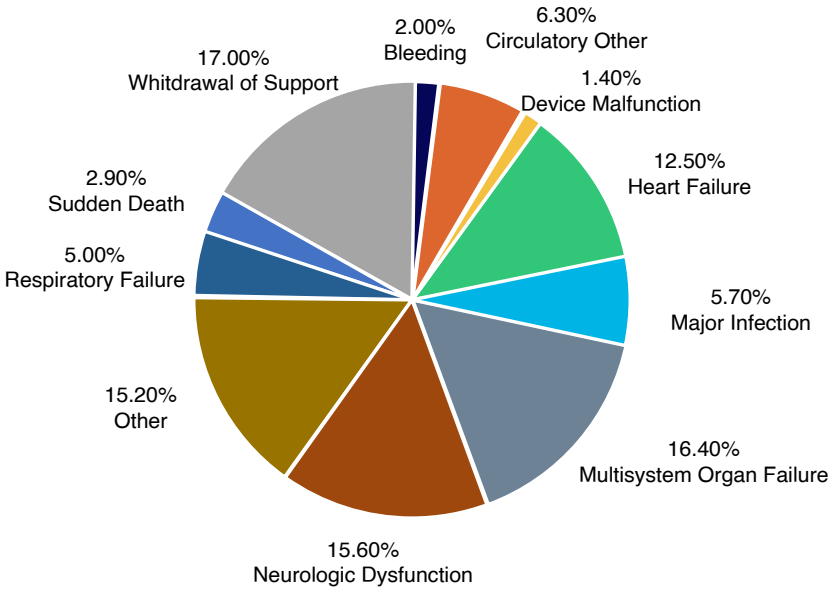

Figure 1.3: Primary Cause of Death in Patients on Isolated LVAD Support, data from [12].

The MCL aims to mimic the structure and functioning of the native cardiovascular system (CVS), providing a realistic testing environment for performance assessment. It simulates hemodynamic parameters such as heart rate (HR), ventricle contractility, peripheral resistance, arterial compliance and fluid inertance under healthy and various degrees of pathological conditions. These parameters are adapted to obtain physiological pressure and flow waveforms.

In vitro studies conducted using the MCL offer several advantages over in vivo studies, particularly when there is a need for quantitative investigation and the precise control of physiological parameters. Additionally, in vitro studies eliminate the requirement for ethical approval and are significantly more cost-effective than animal studies. Consequently, MCLs are extensively employed as a preliminary step prior to in vivo experimentation.

In order to evaluate the performance of CADs, it is crucial to incorporate relevant features of the CVS into the MCL. This ensures a comprehensive assessment of the devices' functionality. For example, it is necessary to include a model representing the pulmonary and systemic circulation within the MCL to study the fluid dynamics and interactions between these two circulatory systems. Similarly, to study the timing aspects of IABP, it is advisable to incorporate a model of the coronary circulation and aorta into the MCL. Since the IABP is positioned within the aorta and is specifically designed to enhance mean arterial pressure and myocardial perfusion, the inclusion of these components in the IABP

enables a comprehensive evaluation of the timing-related effects and efficacy of the IABP. Whilst a set-up for a artificial heart valve would require a accurate model of the hearts atria and ventricle [13]. Taking these factors into consideration when designing the MCL ensures for a more realistic simulation of the CVS and accurate assessment of the CAD. However, the majority of the MCL do not accommodate important pressure regulatory functions into their test set-up. Adding this feature into a MCL would enhance the representation of the native CVS and accuracy of CAD testing.

1.1 The cardiovascular system

The MCL aims to replicate the function and structure of the native CVS as closely as possible. The cardiovascular system is responsible for pumping and transporting blood throughout the body. It consists of the heart, blood vessels, and blood, and is essential for maintaining the delivery of oxygen and nutrients to the body's tissues and the removal of waste products.

1.1.0.1 The heart

The heart, illustrated in figure 1.4, is a muscular organ that consists of two pumps, the right and left ventricles. These pumps are filled with blood from the reservoirs known as the atria. The right ventricle pumps deoxygenated blood through the pulmonary trunk to the lungs, where it is oxygenated and returned to the left side of the heart via the pulmonary veins (the pulmonary circulation). The left ventricle pumps oxygenated blood to the tissues of the body. Some of the oxygen is used by the tissues, and the partially deoxygenated blood is returned to the right atrium via the superior and inferior vena cava, completing the long, high-pressure systemic circulation. The movement of blood through the heart and veins is regulated by one-way valves, ensuring that the blood follows a circular pathway.

The ventricle is primarily composed of cardiac muscle and fills with blood during muscle relaxation, a process called diastole. During contraction, or systole, the left ventricle pumps blood into the aorta, the largest artery in the body, at high pressure. From the aorta, the blood branches into smaller arteries and eventually reaches millions of thin-walled capillaries, where metabolites can diffuse between the capillary blood and the

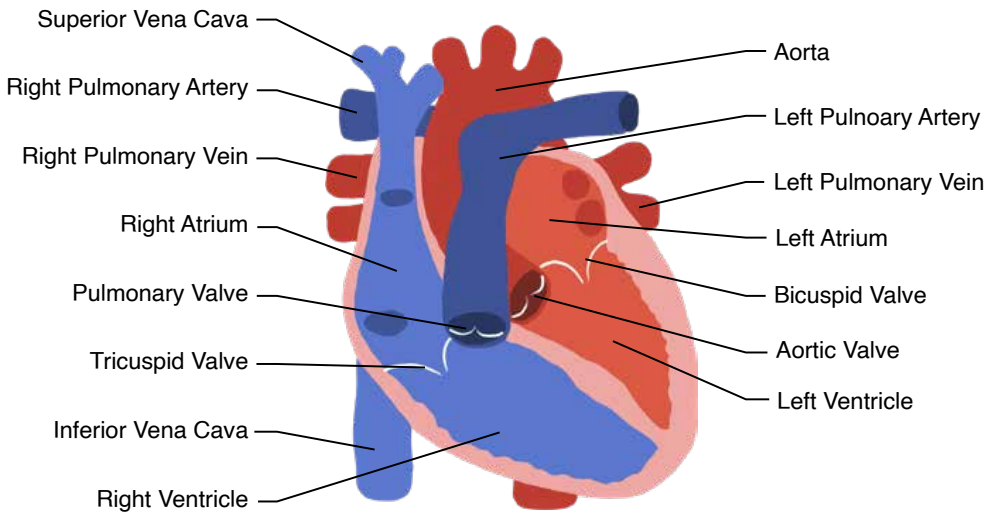

Figure 1.4: An illustration of the heart and the main arteries and veins.

cells of the body. One complete contraction and relaxation of the ventricles is called the cardiac cycle, i.e. the period of one heart beat.

The cardiac cycle is characterised by its change in pressure and volume of the ventricle over time as shown in figure 1.5. Prior to the closing of the mitral valve (the valve between the left atria and left ventricle) the heart is in diastolic state. Electrical activation of the heart initiates contraction, the pressure inside the chamber rises and the mitral valve closes preventing any blood from entering or leaving the ventricle during this time. This period is known as the isovolumic contraction. As the pressure rises, the aortic valve (positioned between the left ventricle and the aorta) opens and blood is injected into the aorta. As contraction reaches its maximum, ejection slows down and the aortic valve closes. This marks the end of the ejection phase where the ventricle is at its lowest volume. The isovolumic relaxation process continues as the pressure within the ventricle declines, and the mitral valve eventually opens, allowing blood to flow into the ventricle during filling phase. The total amount of blood ejected by the ventricle is what we call the stroke volume (SV). The SV is effected by three factors, the cardiac contractility, preload and afterload. Contractility is defined as force of the contraction of the heart muscle. Preload is the force (load) on the heart muscle prior to its being activated to contract [14]. Afterload is defined as the resistance to ventricular ejection, in other words the load that the heart must eject against [15].

There are many advantages on plotting the left ventricle pressure as function of the

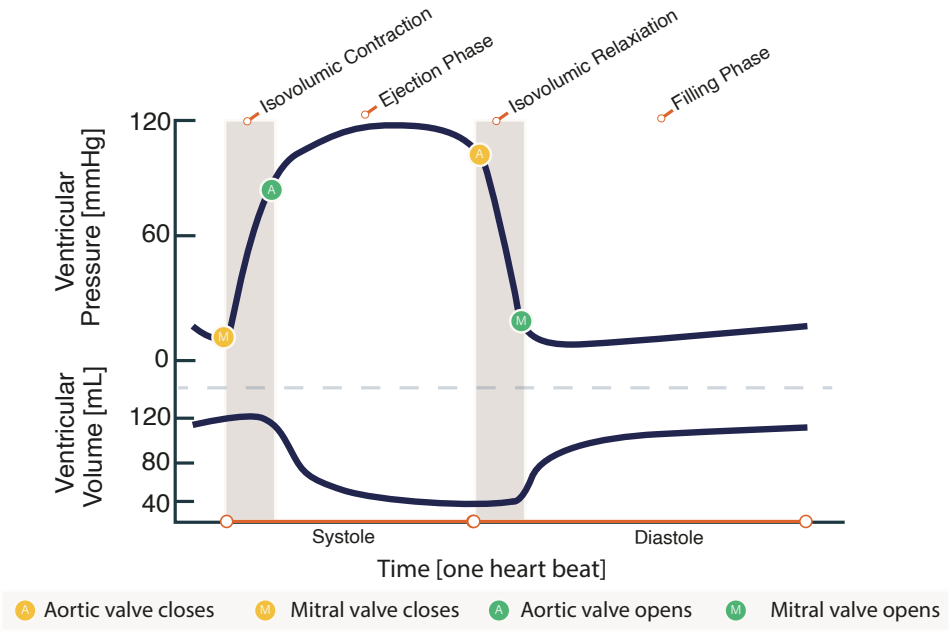

Figure 1.5: The pressure and volume over time of the cardiac cycle.

volume on a pressure-volume diagram. The resulting curve forms a loop, called the pressure-volume loop (PV-loop), as shown in figure1.6. The PV-loop traces a counter-clockwise path as time progresses. The onset of systole corresponds to the point at the bottom right corner, after which the isovolumic contraction, ejection and isovolumic relaxation and filling phases follow. The PV-loop is a useful tool for understanding the changes in left ventricular volume and pressure during the cardiac cycle, and allows for the analysis of several important features of cardiac function. The details of the PV-loop and its cardiac parameters will be explained in section 2.1.1.

1.1.0.2 Resistance

The hydraulic resistance of a blood vessel refers to the opposition that the vessel offers to blood flow. This resistance can be quantified using Darcy's Law of flow, which states that resistance is the difference in mean pressure needed to drive one unit of flow in the steady state and its units are $mmHg \cdot mL/min$. The resistance of a blood vessel is inversely related to its conductance and is influenced by various factors, including the vessel's diameter, length, and the viscosity of the blood. Among these factors, the vessel's diameter has the greatest impact on resistance. In general, wider vessels such as arteries and veins have a lower resistance to blood flow compared to narrower vessels

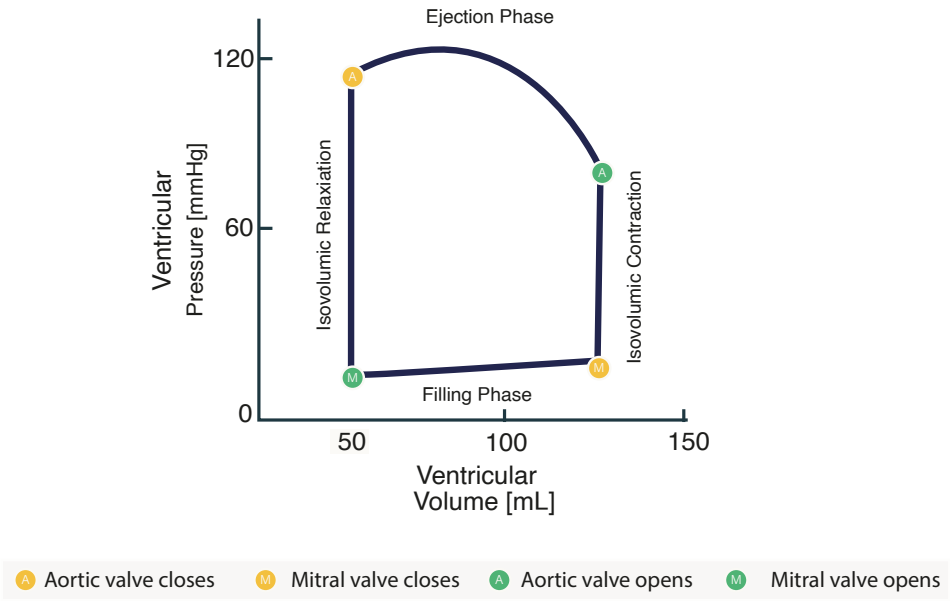

Figure 1.6: The pressure volume loop.

like arterioles, which have a higher resistance. The larger the resistance, the lower the blood flow and the larger the decrease in bloodflow, illustrated in figure 1.7. The overall resistance of the systemic circulation (i.e. systemic vascular resistance (SVR)) in a resting human is determined by the resistance of the various classes of blood vessels, with the large arteries contributing only 2% to the total resistance, the smallest arteries and arterioles contributing approximately 60%, the capillaries contributing 20%, and the venous system contributing 15%. Darcy's Law can be applied to understand how blood flow to a specific organ or tissue is regulated. Changes in vascular resistance caused by the contraction and relaxation of the arterial system's terminal branches play a crucial role in regulating local blood flow.

1.1.0.3 Blood flow regulators

Multiple regulatory mechanisms of the CVS are able to respond to changes in the body's demands, such as exercise, standing and stress. Such as the Frank Starling response, which is the physiological ability of the heart to change its contraction force in response to changes in venous return. Among the various mechanisms involved in blood pressure regulation, the baroreflex response plays a prominent role. Baroreceptors are sensitive to even minute changes in blood pressure, effectively detecting alterations in the circu-

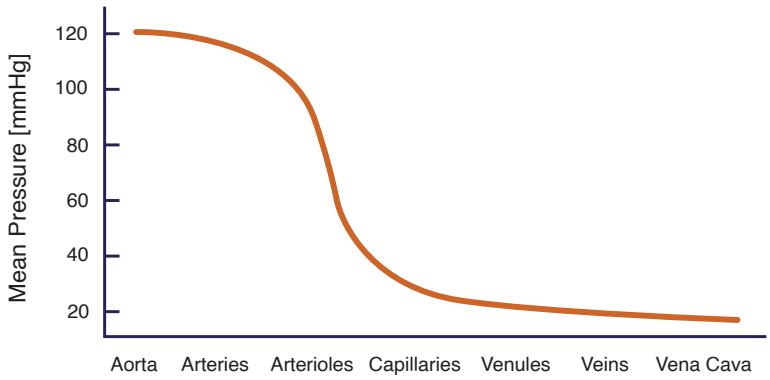

Figure 1.7: The mean pressure in the systemic circulation of a resting human.

lation. Consider, for example, the transition from sitting to a standing posture, which induces a decrease in blood pressure; this shift is expeditiously detected by the baroreceptors, which immediately activate reflex mechanisms to mitigate pressure reductions in cerebral and upper body circulation. Positioned in the walls of the carotid sinus and aortic arch, these stretch receptors serve as a sensor for blood pressure fluctuations. An elevation in blood pressure tightens the stretch on the baroreceptors, prompting them to send an electrical signal in the afferent nerves towards the central nervous system at an accelerated rate. This signal is then transmitted via both sympathetic and parasympathetic (vagal) efferent pathways targeting the blood vessels and the heart, and the pacemaker cells of the heart, respectively. Subsequently, the autonomic nervous system processes these signals and modulates cardiac output, peripheral resistance and venous capacitance to stabilise blood pressure. A graphical representation of the baroreceptors' response to changes in mean arterial blood pressure is depicted in figure 1.8.

1.1.1 Models of the cardiovascular system

Three different types of MCLs exist. Firstly, the mechanical MCLs (M-MCLs), which simulates the CVS using mechanical and hydraulic components. M-MCLs were the first type of MCLs developed. M-MCLs represent the ventricles with hydraulic pumps, the arterial compliance by water and air-filled reservoirs (or flexible tubes), and the resistance is simulated by obstructions of the flow path. M-MCLs can test various CADs and pathological conditions. However, the fixed design limits the range of applications. Numerical models of the CVS develop in parallel to M-MCLs, in which the CVS is described with mathematical

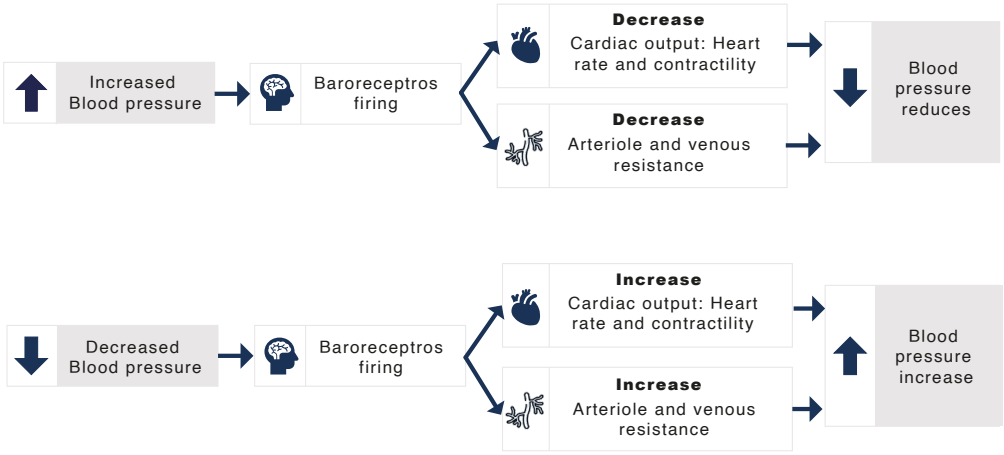

Figure 1.8: The parameters of the baroreflex.

expressions. All numerical MCLs (N-MCL) reviewed in this thesis are lumped parameter models. They have absolute reproducibility, controllability and are more flexible than M-MCLs. However, they neglect or simplify physiological aspects and complex properties of the CVS (e.g. wave travel and turbulence).

Merging N-MCLs and M-MCLs defines a third group of MCLs: hybrid MCLs (H-MCLs) [16]. In an H-MCL the numerical and mechanical parts run alongside and communicate with each other in real-time using a numerical-hydraulic interface. The H-MCL can describe cardiovascular characteristics using computer algorithms that are too difficult to represent with mechanical components and provides a hydraulic platform to connect the physical prototypes of CADs. Within the next few years, H-MCLs are likely to become an essential test-bench for CADs development.

Part of the CVS in an H-MCL is modelled numerically. The numerical modelling of the CVS can range from 0D to 3D models, depending on the specific goals and desired level of accuracy. Figure 1.9 illustrates the different dimensional models employed in cardiovascular simulations. In 0D models, also known as lumped parameter models, the components of the CVS are simplified into electrical elements [17], [18]. 1D models enable the description of pulse wave transmission within the vasculature and are particularly useful for studying blood flow around stents and similar applications [19]. 2D models are employed to investigate local flow velocities in axisymmetric domains, which prove valuable in the study of CADs such as prosthetic valves [20]. Finally, 3D models allow for the anal-

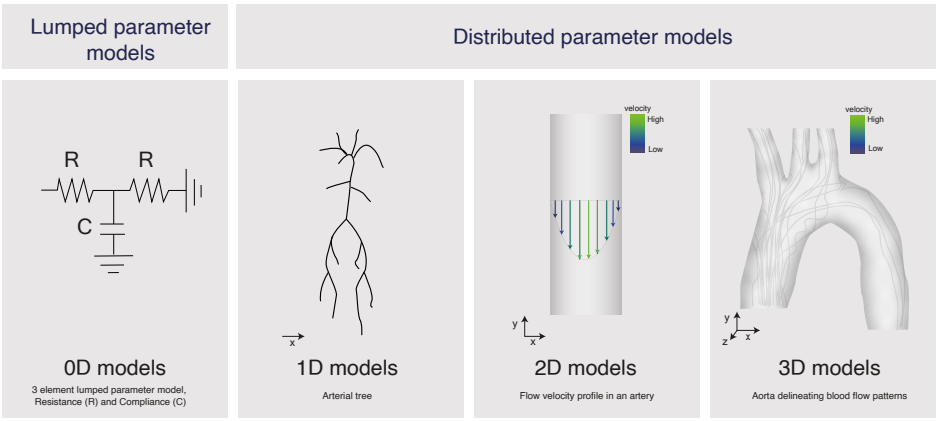

Figure 1.9: Different dimensional models of the cardiovascular system.

ysis of complex flow patterns, but their use typically demands substantial computational resources [21].The choice of dimensional models in cardiovascular simulations depends on the specific research objectives and computational resources.

The models of the CVS have evolved over the years. Hales [22] was the first to introduce a conceptual lumped parameter model of the arterial tree in 1733. He observed that the variation of pressure in the arterial system is related to the elasticity of large arteries. Weber [23] was the first to compare the elasticity of the arteries with the Windkessel, in which the pulsatile pump is damped by an air chamber. Frank [24] was the first to mathematically describe the arterial response with a so-called two-element Windkessel model, using an electrical resistor and a capacitor to represent the SVR and the total arterial compliance, respectively. Later, three and four-element Windkessel models were developed to increase the accuracy of the impedance [25]. While the Windkessel elements do not replicate a specific vessel, they exhibit favorable arterial impedance characteristics across a broad spectrum of physiological HR frequencies [26]. Therefore, these lumped parameter models offer a better computational efficiency while providing valuable insights into the overall hemodynamic behaviour.

1.2 Mock Circulatory Loops: Early Beginnings

The M-MCLs is lumped parameter modelling in a physical test rig: electrical components are replaced by their hydraulic equivalents, illustrated in figure 1.10. The compliance of vessels is modelled with Windkessel chambers, a closed water reservoir with a trapped volume of air above the water level [13], [27], [28], occasionally using spring capacitors [29], [30] or flexible tubes [31], [32]. The resistance of arteries is replicated by occluding the flow path using for example, swing check valves [28] or throttles [33] to mimic vasoconstriction. The heart is often represented using pneumatic [13], [34] or hydraulic pumps [35], [36]. The inertance of the M-MCL is dependent on its dimensions and the working fluid density.

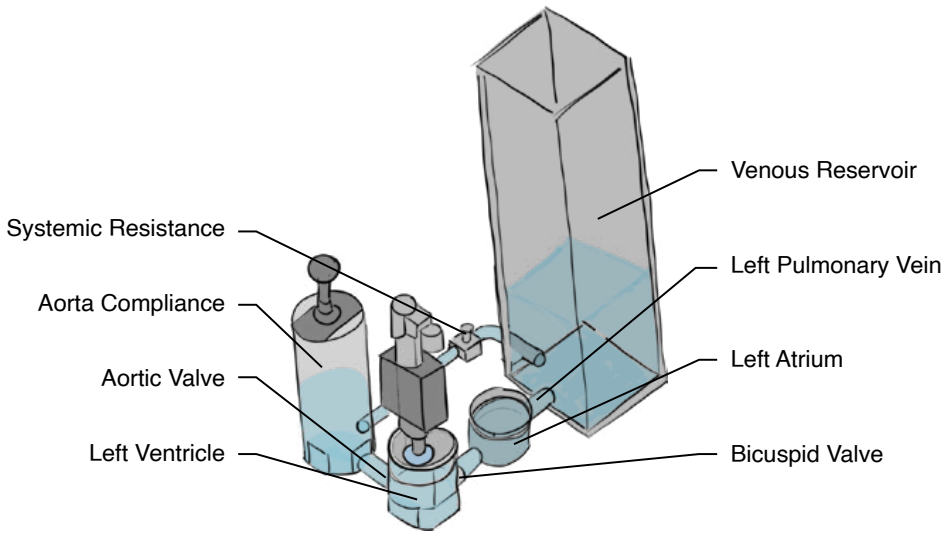

Figure 1.10: Illustration of a typical M-MCL.

Preliminary M-MCLs were test rigs for artificial heart valves [13] and TAHs [28], [37], [38]. Donovan et al. developed a compact M-MCL simulating the systemic and pulmonary circulations using a two-element Windkessel model for each [28], illustrated in figure 1.11, a design that continues to be adopted by many others [38]–[43]. They were also the first to attempt implementation of a simplified version of the baroreceptor response by automatically controlling SVR and pulmonary vascular resistance (PVR) with bellow operated valves [28].

The abstracted M-MCL proved to be a valuable in-vitro tool to test artificial blood pumps and heart valves. However, due to its simplistic nature it does not allow the study

of wave propagation, a limitation of 0D modelling. Early pioneers, Reul et al, developed a hydromechanical model of the arterial systemic circulation with approximated geometry and elastic properties of arteries [43]. Although the model was unusable for testing CADs, it does allow for studying haemodynamic properties of the arterial system in an in vitro setting.

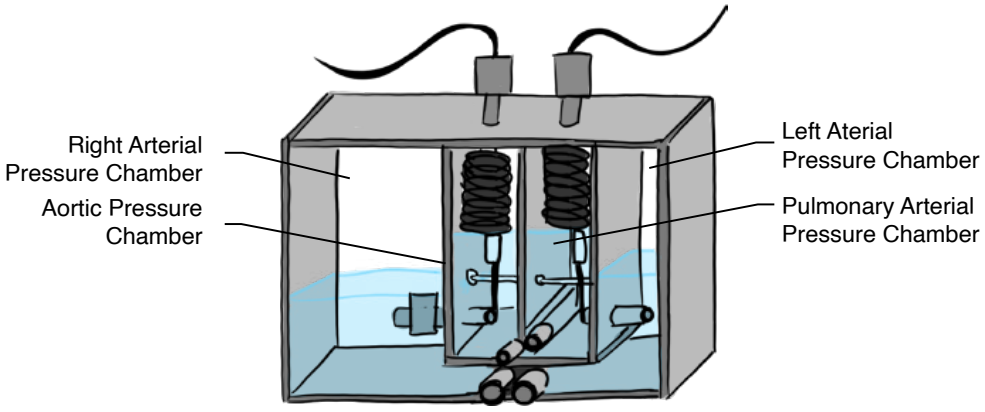

Figure 1.11: Illustration of the Donovan et al. M-MCL. (modified from [28])

1.3 Recent Advances of Mock Circulatory Loops

One of the advances in recent MCLs is the driving system. Verdonck et al. developed a computer controlled in vitro model of the left heart for artificial heart valve testing. The silicon model of the atrium and ventricle were placed within a water-filled housing, where the amount of pressure in the housing was controlled by a feedback system. The system was able to regulate filling pressure, contraction, relaxation and HR. In other systems Left Ventricular Assist Devices (LVAD) were used to generate physiological flow conditions controlled by a pneumatic apparatus [44].

With computer controlled heart, researchers gained the ability to alter cardiac output which allowed simulation of exercising conditions [45]–[47] and pathological conditions such as congestive left heart failure [34], [48]–[51], right heart failure [52], valve regurgitation [53] and cardiac arrhythmia's [54]. Timms et al. used a pneumatic ventricle in an M-MCL to simulate normal and heart failure at rest by adjusting mean arterial pressure, HR, contractility, SVR, PVR and arterial compliance [55]. Cardiac output was reduced from

5.15 L/min to 2.7 L/min for healthy and left heart failure patients, respectively. The M-MCL was later used for VADs performance assessment [56], [57]. Similar conditions were reproduced by Pantalos et al. who manipulated driveline pressure and SVR resulting in a reduction of cardiac output from 5.0 L/min to 3.0 L/min [29], whilst Tsuboko et al. simulated right heart failure by regulating the atrioventricular interaction [58]. Similar heart conditions were simulated in N-MCLs by reducing compliance in the left ventricle [59].

1.3.1 The Frank Starling Mechanism

The Frank-Starling response could be simulated with computer controllable ventricles [29], [60], [61]. MCLs including the Frank-Starling mechanism describe the interaction of the CADs with the CVS more closely [62], whilst MCLs without preload and afterload response will produce unphysiological results [63]. In early MCLs [63]–[67] the Frank-Starling mechanism using the time-varying elastance model of Suga-Sagawa [68]. Baloa et al. were amongst the earliest to implement the elastance model into an M-MCL [63]. In this model, the elastance of the left ventricle is linearly related to ventricle volume and pressure. Baloa et al. reported a left ventricle elastence (i.e. the gradient of the end-systolic pressure-volume curve) in the range of 2.14 mmHg/ml to 2.27 mmHg/mL/ Yokoyama et al. reported a linear elastance curve ranging from 1.75 mmHg/ml to 0.56 mmHg/ml in their M-MCL, which can therefore simulate healthy and heart failure conditions [69].

Burkhoff et al. questioned the assumption of the linear end-systolic-pressure-volume relationship in humans and noted that the time-varying elastance model inadequately describes the contractility of the left ventricle under diseased and cardiac support conditions [70]. Furthermore, Vandenberghe et al. showed in an in vivo experiment that the time-varying elastance model insufficiently represented the left ventricle under mechanical support [71]. Moreover, in MCLs using the linear elastance model, the end-systolic-pressure-volume curve crosses the volume axis at a negative value, which suggests a negative unstressed ventricle volume [63], [65], [72].

Colacino et al. adapted the linear time-varying elastance model to a non-linear elastance variant and proved through a numerical and experimental verification that the non-linear elastance model can simulate the preload and afterload sensitivity of the natural ventricle more closely [73]. Other researchers used a natural logarithmic elastance model

[74] and look-up tables [75].

1.3.2 Physical Anatomical Models

In parallel with the development of the mock ventricles, researchers implemented anatomical models for flow visualisation studies and higher-order Windkessel models of the systemic and pulmonary circulations. Five-element Windkessels models were introduced to simulate both systemic and pulmonary circulations [76]. Anatomical models of arterial beds [77], [78] and pulmonary trunks [79] were developed to study haemodynamics of CADs. Patient-specific left ventricles were developed to asses intraventricular balloon pump [80] and for in vitro flow visualization studies [81]–[84]. Several studies include anatomical models of the aortic arch [81], [83], [84]. Firstly, Litwak et al. used an anatomical model of the ascending and descending aorta to study the aortic blood flow of continues flow and pulsatile flow VADs [85]. Geier et al. used an aortic model to study different cannulation types of extracorporeal membrane oxygenation [86]. Whilst Peter et al. [87] developed an anatomical model of the aorta including renal circulation to study wave travel.

More complete anatomical models of the systemic circulation have been developed by Kolyva et al. [77] and Gehron et al. [88] Kolyva et al. tested an IABP on an M-MCL with an anatomical model of the aorta and twelve of its largest branches [77], [89]. Local compliance and resistance were simulated using syringes of varying air volume and capillary tubes of different sizing at the outlet of the branches. Gehron et al. [88] made a life-sized arterial bed of the venous and arterial circulation which allowed visualisation and quantification of flow phenomena of the CVS under extracorporeal life support. In this study the local compliance values could not be changed; however, resistance could be adjusted using variable Hoffman clamps which increased or decreased vessels diameter.

Refinement of the anatomical models of the pulmonary circulation was achieved by Knoops et al. [79], Mueller et al. [90], and D'Souza et al. [91]. Knoops et al. [79] analysed the pulmonary hemodynamics by recreating an anatomical model of the pulmonary trunk with two generations of bifurcations. Their research showed the possibility of recreating patient-and pathology-specific models for haemodynamic investigations. Mueller et al. [90] developed a pulmonary M-MCL with an anatomical model of the right heart to study the effects of CADs on the pulmonary circulation. The M-MCL was able to mimic a

healthy pulmonary condition, mild and severe pulmonary hypertension and right heart failure. D'Souza et al. [91] recreated a patient-specific 3D model of the proximal pulmonary artery used as a vascular test device. The model was evaluated in an M-MCL of the pulmonary circulation to evaluate hemodynamics. The pulmonary circulation has been redefined in a numerical model by King et al. [92]. In this study, a numerical Windkessel model was developed to simulate patient-specific pulmonary conditions.

1.3.3 Coronary, Cerebral and Renal Circulation Models

Another important development of MCL is the implementation of the coronary circulation. Geven et al. [93] were amongst the first to accurately mimic this. The native coronary circulation supplies the heart muscle with blood during diastole, whereas in systole the coronary vessels are compressed due to the high ventricular pressure. The heart can regulate the amount of blood flow into the coronary arteries via vasoconstriction or vasodilation. Geven et al. [93] simulated the coronary vessel with a tube that collapses under ventricular pressure. The autoregulation of the coronary blood flow was presented as a clamp between the myocardial circulation and the coronary artery. Other researchers simulated the coronary circulation using a dynamic resistor in M-MCLs [29] or in N-MCL by connecting left ventricle output with right atrium input [94], [95].

Rezaienia et al. [96] implemented the coronary circulation with autoregulatory mechanism and aortic anatomical model in an M-MCL. The M-MCL also included the haemodynamic response of the cerebral autoregulation while operating a mechanical circulatory support device in the descending aorta. The dilation and constriction of the cerebrovascular system and coronary system was mimicked with pinch valves. Similar techniques have been used to simulate the autoregulation of the renal circuit in M-MCL as well [97].

More recently, Gregory et al. [98] managed to replicate physiological accurate waveforms with an M-MCL that simulates; systemic, pulmonary, cerebral and coronary circulations. The haemodynamic response of the M-MCL was validated using impedance cardiography data from healthy humans. The Frank-Starling response of the ventricles and the cerebral and coronary autoregulation were included. Furthermore, Clark et al. [99] introduced the cerebral circulation in an N-MCL and M-MCL to study the effect of thromboembolism and Bozkurt [100] modelled the cerebral circulation including the circle of Willis in an N-MCL.

1.3.4 Hybrid Mock Circulatory Loops

Numerical models of the CVS form the basis of the H-MCL, part of the model is presented by a hydraulic [101] or an electrical section [102], [103]. The difficulty in the development of H-MCLs is achieving a fast and accurate numerical-physical interface, i.e. the interaction between the numerical and physical model and the CAD. This interaction is achieved with sensors, actuators and fast responding control systems. In electrical-numerical MCLs, the interface is achieved by voltage-controlled current and voltage generators [104]. Ferrari et al. created a numerical-hydraulic interface using DC motor driven gear pumps; atrial and arterial pressure were acquired from the hydraulic circuit and are used as two input variables for the numerical part [104]. Output flow is computed in the numerical model and sent to a DC motor and servo amplifier to control the flow of the gear pump in the hydraulic circuit. The same interface has been adopted by others [105]. This H-MCL was used to test VADs and IABPs, in which the CADs were connected to a physical arterial tree or aorta [31].

Alternatively, Ochsner used two pressure-controlled reservoirs and a flow probe as a numerical-hydraulic interface to test TAHs [106]. This interface is similar to others, except that SVR was adjusted to elicit changes in vasculature pressure [107]–[109]. Recently, Mirzaei et al. [110] studied the coupling of a physical experiment with multiple branches with a lumped parameter numerical simulation. The numerical-hydraulic interface has been tested to show its applicability but has not been used to study CADs yet. Others have developed an H-MCL to test cardiac compression devices; an apparatus that wraps around the heart to provide beating assistance [111], [112]. The mechanical ventricles, interacted with a numerical model of the CVS. The contraction of the CAD is measured with a force sensor, which is used as input to the numerical model. The numerical model uses the force measurement to calculate the cardiac output and venous return of the heart. The diameter of the simulated ventricles was calculated, from the cardiac output and venous return, and adjusted in the physical system using a swing-arm actuator.

The Frank-Starling mechanism has also been widely adopted in H-MCL using Sagawa's [68] variable elastance model [103] or using a time-varying wall stress function [111]. Ochsner et al. [106] used the non-linear elastance model of Colacino et al. [73] in their H-MCL, while Hanson et al. [111] used a numerical heart model of Urbaszek and Schaldach [113]. H-MCL were also able to simulate pathological states, such as reduced left ventricular elastance

[104], [114], [115] and reduced ventricular contractility [106], [111].

1.3.5 Baroreceptor Response

Ochsner et al. [106] evaluated the performance of VADs on an H-MCL with baroreceptor response. The baroreceptor response adapted SVR and PVR when the pressure in the arterial system changed while keeping the HR constant. Fresiello et al. studied IABP timing on baroreceptor activity and the VAD's performance [116] with an H-MCL. The baroreceptor response was based on the mathematical description by Ursino [117], change in mean pressure affected; HR, SVR and venous volume. Cuenca-Navalon et al. used an H-MCL to study TAHs which included a numerical model of the baroreceptor response [118] in which SVR and venous volume were adopted to maintain mean arterial pressure. HR changes and contractility were not included in this model, as the TAH to be tested should be able to replicate these native feedback mechanisms.

The baroreceptor response has been studied in M-MCLs as well. Mushi et al. adopted Ursino's model [119] into a continuous flow M-MCL [120]. The numerical model, calculated HR, ventricular contractility and SVR from mean arterial pressure. HR and ventricular contractility were changed in the physical model by adapting the speed of the centrifugal pump. SVR was adjusted with a pressure valve [120]. Jansen-Park et al. managed to fully implement the Frank-Starling mechanism and baroreceptor response into an M-MCL [121]. The mean arterial pressure was regulated by changing the HR, contractility, SVR and unstressed venous volume. The baroreflex response implemented by Vaes et al. [122] was based on a mathematical model by van Roon et al. [123] in which the baroreceptor response readjusted systemic pressure by changing the HR.

Lastly, Bozkurt et al. investigated their newly developed continuous flow LVAD using an N-MCL including baroreceptor response and healthy and pathological hemodynamics [124]. Similarly, Bonnemain et al. used an N-MCL including baroreceptor response to study the hemodynamics of a continues flow LVAD on the location of the anastomosis [125]. An overview of MCLs that included the baroreflex mechanism is given in table 1.1.

Ever since the development of one of the first MCL[37], their numbers and complexity rapidly rose over the years. MCLs play a key role in the development of a wide range of CADs. The MCLs's repeatability, flexibility and controllability make it a valuable platform to access CADs performance preliminary to in vitro studies. An increasing number

Table 1.1: Overview of the baroreflex mechanisms implemented in MCL. The table specifies which parameters of the baroreflex mechanism are considered: resistance, contractility, unstressed volume and HR.

First Author	Year	Type	Resistance	Contractility	Unstressed volume	Heart rate
F.M. Donovan	1975	M-MCL	X	✓	X	✓
X. Ding	2014	N-MCL	X	✓	X	✓
M. Vaes	2007	M-MCL	X	X	X	✓
F.M. Colacino	2008	M-MCL	X	✓	X	X
S. Mushi	2008	M-MCL	✓	✓	X	✓
S. Bozkurt	2013	N-MCL	X	X	X	✓
J. Bonnemain	2013	N-MCL	✓	✓	✓	✓
G. Ochsner	2012	H-MCL	X	✓	✓	X
E. Cuenca-Navalon	2014	H-MCL	✓	✓	✓	✓
L. Fresiello	2011	H-MCL	✓	✓	✓	✓
S. Schampaert	2014	M-MCL	X	X	X	✓
S.H. Jansen-Park	2016	M-MCL	✓	✓	✓	✓
A. Petrou	2019	H-MCL	✓	✓	✓	✓

of researchers have developed a system which is capable of reproducing a wide variety of patient conditions including; rest [55], exercise [46], different degrees of heart failure [50], [126], hypertension [52] and valve insufficiencies [127]. The recent study of Gregory et al. [98] showed the excellent controllability and flexibility of the M-MCL. They studied the hemodynamics of simulated patients in resting, exercise and left heart failure conditions with and without ventricular support. However, the M-MCL lacked implementation of the baroreceptor response. Alternatively, Shi et al. studied the hemodynamics responses of different VADs in their N-MCL, with the limitation of the numerical model preventing the study of complex hemodynamic effects[64]. Thus, the solely hydraulic or numerical-based platform does not always provide the flexibility that is required for a full performance assessment of CADs.

Table 1.2: Comparison table between the different MCLs: N-MCL, H-MCL and M-MCL.

	M-MCL	N-MCL	H-MCL
High flexibility	X	✓	✓
Compact	X	✓	✓
Physical prototype	✓	X	✓
Numerical prototype	X	✓	✓
High reproducibility	X	✓	✓
Complex hemodynamic effects	✓	X	✓

The hybrid platform allows interaction between the physical prototype and the numerical model of the CVS. The hybrid platform offers advantages over systems that are solely mechanical or solely numerical-based. A comparison of these systems is provided

in Table 1.2. The H-MCL of Petrou et al. showed the unique versatility of the hybrid platform [127]. The numerical part of the H-MCL can easily be changed from the native CVS to the Fontan circulation. Moreover, the mechanical valves can be removed making the hybrid platform sufficient to study both biVADs and TAHs. However, the numerical models used by Petrou et al. lack validation, due to the absence of relevant clinical data [127].

The lack of validation is a recurring problem in mock circulatory studies. Often, researchers compare their static haemodynamic magnitudes against a range defined in the literature. For example, Mueller et al. compared their static haemodynamic parameters against a range of literature data from clinical and mock circulatory studies [90]. In another study, the effect of arterial compliance on IABP performance was studied both in an MCL and in patients [128]. However, it is important to evaluate the time response of the MCL as well, to study the performance of CADs during postural changes or exercise [98]. This problem has only recently been recognised and addressed in the study of Gregory et al. who validated their acquired data from an M-MCL against clinical data [98]. Unfortunately, clinical data of pathological conditions was not available to them, and thus validation has only been done for healthy patients. A complete validation of an MCL is still absent in the available literature.

MCLs have been developed with additional subparts of the CVS such as the coronary, carotid and renal circulations[93], [96], [98], [129]. By expanding the MCL, more physiological parameters can be investigated such as renal perfusion, which often leads to complications in patients with LVAD [130]. Moreover, a module of the coronary circulation would allow evaluation of specific pathologies like myocardial infarction [93]. Some MCLs only consider the left heart and systemic part of the CVS [48], [121] or the pulmonary circulation[90]. However, since a CAD interacts with the entire CVS it is essential to model the complete circulation. Moreover, it is important to study the fluid balance between the pulmonary and the systemic circulation for physiological and pathological states [131]. The cerebral circulation has solely been modelled in an N-MCL [100], with a hydraulic representation of it, up to this date, limited to only the carotid arteries. A hydraulic model of the cerebral circulation would provide valuable insight into the interaction between the CAD and the cerebral circulation. The regulatory mechanisms of the renal and cerebral arteries have only been partly implemented into a few MCLs [96], [98]. The renal arteries can constrict afferent arterioles, reducing renal blood flow. The effect

of CAD on renal pathology is complex and not yet well understood [132]. An MCL could be used as a tool to understand the hemodynamics of the renal circulation. Furthermore, the brain responds to an increase in carbon dioxide or hydrogen ions, which causes dilation in the cerebral vessels, allowing the waste products to wash out. This autoregulatory mechanism has not been assessed in MCLs yet.

The Frank-Starling mechanism has been implemented in several MCLs [66], [129], [133], [134], however, in some MCLs this mechanism is still absent, resulting in unrealistic representations of the response of the native heart [46], [88], [107]. Moreover, the linear approximation of the elasticity of the heart seems to be outdated and needs to be replaced with a non-linear variant [73]. The baroreceptor response, which affects HR, contractility, venous volume and SVR, has been introduced in MCLs as well [106], [120], [121]. Most of the MCLs simulating the baroreceptor response kept the HR constant [135], [136] or only considered the change of HR [137]. Jansen-Park et al. were able to implement the complete baroreceptor response in an M-MCL. The baroreceptor response was evaluated with a bleeding test where 450mL was dispensed from the system. The M-MCL was able to compensate for some of the pressure drops, mean arterial pressure dropped from 90 mmHg to 72.5 mmHg and was increased to 82.5 mmHg. However, it was not able to fully recover to the mean arterial pressure.

Lastly, within MCLs, pressure and flow are frequently measured parameters of interest. However, certain vascular parameters, including ventricle volume and arterial compliance, are often overlooked. While some of these parameters may pose challenges in measurement due to sensor limitations or practical considerations, others may be inaccurately assumed to exhibit linear behaviour. In recent years, machine learning techniques have been applied to predict cardiovascular parameters, such as blood pressure waveforms [138], thereby warranting further exploration of their use within MCL setups. Moreover, machine learning could potentially facilitate the design of control systems that simulate patient-specific pressure and flow waveforms based on individual data [139].

For future MCLs, it is imperative to address these limitations of current MCLs. Integrating fully automated compliance chambers [140] and resistance devices [141] allows the implementation of the necessary autoregulation of the CVS. Parts of the CVS that are too difficult to model hydraulically can be implemented into the MCL with a numerical model, obtaining a flexible and cost-effective H-MCL.

1.4 Research Objectives

This thesis aims to address the limited representation of pressure regulatory mechanisms in MCLs. The primary purpose of this thesis is to advance the development of next-generation MCL with a baroreflex response, this is divided into three objectives:

Objective 1: Cardiac Output Control: Control of Heart Rate and Contractility The cardiac output is controlled in the baroreflex response via by both the sympathetic and parasympathetic pathways. Thus, for the implementation of the baroreflex in a MCL it is necessary to develop a control system of the left ventricle simulator for the HR and ventricle contractility. Therefore, this objective aims to develop a control system for HR and ventricle contractility of the left ventricle simulator.

Objective 2: Development and Characterisation of a Fully Automated Vascular Resistor Furthermore, the sympathetic pathway controls the SVR. Therefore, the second objective is to develop a physical automated vascular resistor that can be integrated into the MCL.

Objective 3: Implementation of the Baroreceptor Response Moreover, a numerical model of the baroreflex is integrated with the left ventricle simulator and the automated resistor within the MCL. The key objective is to assess how effectively this integrated system can sustain pressure. The primary focus is on the implementation of the baroreceptor response and its proficiency in regulating and maintaining pressure within the MCL.

By addressing these research objectives, this study aims to advance the development of the next generation MCL and enhance its capabilities in simulating the CVS.

1.4.1 Thesis Outline

The thesis is structured into several chapters that contribute to the development of the next generation MCL.

Chapter 2 describes the building blocks and theory that are needed to develop the MCL of this thesis. It describes the analytical and experimental methodologies. It covers the PV-loop and physiological parameters like contractility, resistance, and compliance. It

also describes lumped parameter modelling of blood flow and the mathematical model of the baroreflex response. The latter part of the chapter details a description of the experimental equipment, including the left ventricle simulator and the automated vascular resistor, as well as the complete hybrid set-up for the MCL.

Chapter 3 addresses the control of cardiac output. It offers insights into both HR control and contractility control. The structure follows a logical progression: introduction, methodology (covering HR control, ventricle volume, and contractility), results, discussion, and conclusion.

Chapter 4 focuses on the characterization of the automated vascular resistor. Following an introductory section, the methodology for characterization and step response experiments is delineated. Subsequent sections present results, delve into a discussion of these findings, and conclude the chapter.

Chapter 5 focuses on the baroreflex response. Within the MCL, the chapter tests the baroreflex dynamic response. After an introduction, it discusses the methodology for various test scenarios, presents results, and concludes with a discussion and final thoughts.

Chapter 6 concludes the thesis, offering a general discussion about the research's findings, their significance, and how they align with the study's goals. It closes with an overview of the primary conclusions and potential areas for future research.

Chapter 2

Methodology

This chapter describes the building blocks and theory that are needed to develop the MCL of this thesis. It is broken down in two sections, the analytical and experimental methods, respectively.

2.1 Analytical Methods

Analytical methods play a vital role in the field of biomedical engineering, allowing researchers to simulate and analyse biological systems and phenomena. This section describes the physiological parameters, lumped parameter modelling of the CVS and a mathematical model of the baroreflex.

2.1.1 The Cardiac Cycle: Analysis of the Pressure-Volume Loop and its Physiological Parameters

As mentioned earlier in section 1.1, the ventricular PV-loop demonstrates the connection between intraventricular pressure and volume throughout the cardiac cycle. This representation allows for the determination of several important physiological parameters and variables.

Let us consider the volume axis in figure 2.1. From the PV-loop the maximum volume of the cardiac cycle, EDV, and the minimum volume referred to as the end-systolic volume (ESV) can be identified. The difference between the EDV and the ESV is theSV. At the pressure axis the point of highest pressure on the loop, known as the systolic blood

pressure (SBP) can be found. Moreover, the end-systolic pressure (P_{es}) is in the upper left corner of the loop. In the lower portion of the loop the end-diastolic pressure (EDP), which is the pressure in the ventricle at the end of the cardiac cycle, can be found.

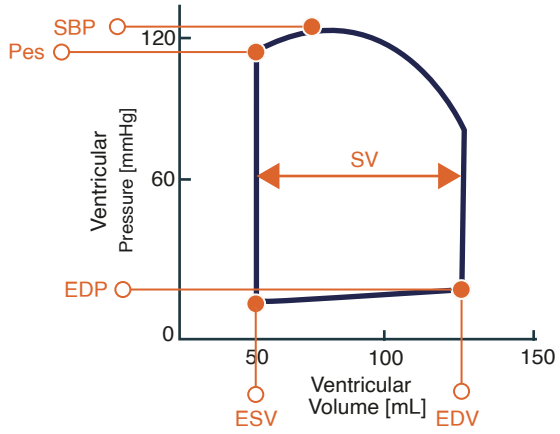

Figure 2.1: The physiological parameters on the PV-loop. In which, SBP is systolic blood pressure, P_{es} is end-systolic pressure, EDP is end-diastolic pressure, ESV is end-systolic volume, stroke volume is SV and EDV is end-diastolic volume

Often the effect of preload and afterload changes on the left ventricle are studied to determine ventricular function. When afterload is increased by raising SVR, the isovolumic contraction phase is prolonged and there is an increase in SBP. This is a result of the increase in the aortic pressure, thus the ventricle must generate a greater pressure to overcome the aortic pressure to initiate ejection. Consequently, this leads to a decrease in SV and increase of ESV (orange loop in figure 2.2, (a)). On the contrary, when afterload is decreased there is an increase in SV and decrease in ESV (yellow loop in figure 2.2, (a)).

Reducing the preload causes a shift in the PV-loop to the left and a decrease in the loop size, as well as a reduction in SV. Additionally, SBP decreases as a result of the decline in cardiac output and fall in arterial pressure (yellow loop figure 2.2, (b)). When preload is increased the contrary result is seen, increase in loop size, SV and SBP.

In figure 2.2 (a) and (b) a line can be drawn which hit the PV-loop at the end of systole. This line is known as the end-systolic pressure volume relationship (ESPVR), which can be assumed to be linear, following from experimental observation, with a slope equal to the elasticity (E_{es}) of the ventricle [142], so that:

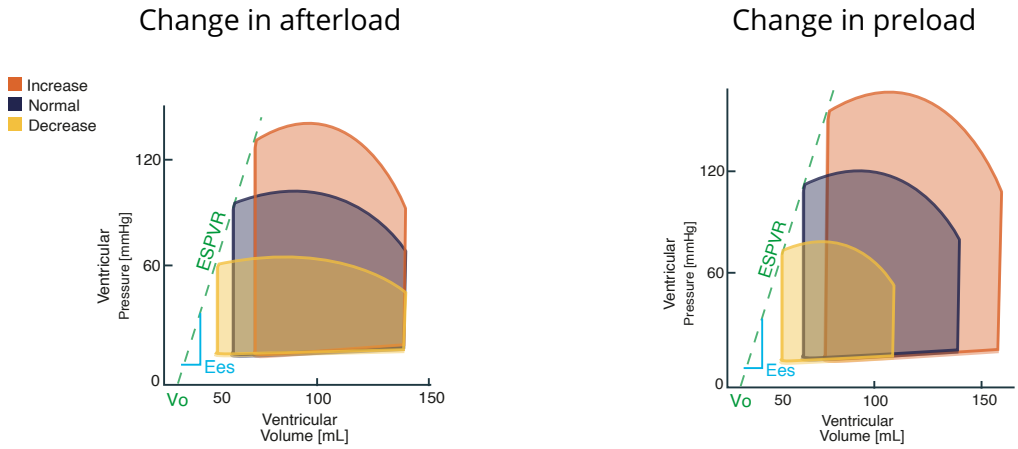

Figure 2.2: Pressure volume loop changes as a result of an increase and decrease of the afterload. Connecting the P_{es} of each loop we can find the End Systolic Pressure Volume Relationship (ESPVR), of which the slope is the elasticity E_{es}

$$P_{es} = E_{es} \cdot (ESV - V_0) \tag{2.1}$$

In which, V_0 is the volume axis intercept.

2.1.1.1 Contractility

The baroreflex modulates the ventricular contractility in order to maintain mean arterial pressure. Contractility is the intrinsic strength of contraction of the ventricle. Sympathetic stimulation can result in a more forceful and shorter contraction which leads to a n increase in ventricular pressure,stroke volume and a reduction in diastolic volume and systole duration [143]. However it is not a well-quantified concept. For example, looking at the PV-loops in figure 2.2 (a), it can be observed that the amount of pressure generated by the ventricle and the SV vary as a result of changing the arterial system, not altering the ventricle. Therefore, the changes in pressure and volume in this figure do not reflect changes in contractility solely. Similarly, the changes on the right side of the figure were caused by modifying the EDV of the ventricle. Thus, pressure and SV are not reliable indices of contractility. However, the changes in the ESPVR does give an indication in the change in contractility [70].

Empirical evidence demonstrated that an increase in contractility, induced by inotropic agents, results in an increase of end-systolic elastance, E_{es} as illustrated in figure 2.3.

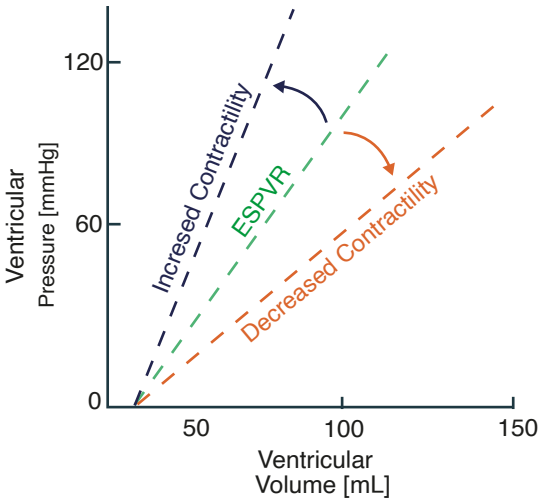

Figure 2.3: Changes in contractility as a result of applying positive contractility agents and negative contractility agents to the heart

Conversely, the use of negative inotropic agents causes a decrease in E_{es} [142]. Due to its independence of load and sensitivity to inotropic agents, E_{es} has been adopted as an index of ventricular contractility [144], one of the parameters that is modulated by the baroreflex.

2.1.1.2 Resistance

Another parameter that the baroreflex controls to maintain blood pressure is arterial resistance. The resistance is equal to the change in pressure (ΔP) divided by the flow rate (Q) [36], which is the hydraulic equivalent of Ohm's law. For continuous flow experiments the mean of the pressure difference is divided by the mean of the flow.

$$R = \frac{\Delta P}{Q} \tag{2.2}$$

For pulsatile flow the resistance can be calculated using equation 2.3.

$$R_{pulsatile} = \frac{P_{mean\,arterial} - P_{mean\,right\,atrial}}{CO} \tag{2.3}$$

In which the cardiac output (CO), is equal to the SV multiplied by HR.

$$CO = SV \times HR \tag{2.4}$$

In other words resistance can be calculated using equation 2.5.

$$R_{pulsatile} = \frac{P_{mean\,arterial} - P_{mean\,right\,atrial}}{SV \times HR} \tag{2.5}$$

2.1.1.3 Compliance

During the ejection phase of the cardiac cycle, a significant portion of the SV is temporarily stored in the arteries. This occurs as the ventricle discharges blood at a faster rate than it can flow through the resistance vessels. The resulting increase in arterial volume leads to distension of the arteries, increasing blood pressure. The magnitude of this pressure rise depends upon both the SV and the compliance of the arterial system. Compliance is quantified as the ratio of volume change to pressure change, $C = \frac{\Delta V}{\Delta P}$

The heart, resistance, and compliance components collectively form the fundamental elements of a lumped parameter model of the CVS.

2.1.2 Lumped Parameter Modelling of Blood Flow and Pressure Distribution in the Cardiovascular System

Lumped parameter modelling is commonly used in the field of engineering to analyse the behaviour of a system with multiple components. It is based on the assumption that a complex system can be represented by a small number of "lumped" parameters such as mass, stiffness and damping, rather than considering the behaviour of each individual component. This approach is often used to model the dynamics of systems that are too complex to analyse using more detailed methods, such as finite element analysis. One of the key benefits of lumped parameter modelling is its simplicity, which allows for fast and efficient analysis of the system's behaviour. However, this simplicity comes at the cost of accuracy, as the lumped parameter model may not accurately capture the behaviour of the system at all points in time.

In cardiovascular engineering lumped parameter modelling is used to analyse the blood flow and pressure distribution in the CVS. The CVS is represented as a series of interconnected systems, each with its own volume, and inertance. Using this representation we can analyse the behaviour of a system as a whole, such as how the blood flow in the peripheral arteries is affected by changes in aortic diameter [145].

To form the CVS lumped parameter model an analogy between the blood flow in the CVS and the current in an electric circuit is applied. The left ventricle, in this analogy, is the pump that drives the blood through the body, while the blood vessels are the electrical conductors. The resistance to flow provided by the blood vessels can be thought of as the resistance of an electrical conductor in a circuit. The blood pressure, which is formed as a result of the interaction between the heart's pumping action and the resistance of the blood vessels, can be thought of as the voltage in the electrical circuit. The compliance of the vessels that allow them to store large amounts of blood can be thought of as capacitors, and the inertia of the blood can be represented with inductors.

An analog of the CVS has been presented by Ursino [119], figure 2.4. The equations describing the pressure and volumes in different points of the vascular bed are written by imposing the conservation of mass and moment and the balance of forces. The pressure drop across a resistance is not dependent on time, but solely on the flow going through it. The flow into the capacitor can be described using equation 2.6.

$$Q = C \cdot \frac{dP}{dt} \tag{2.6}$$

In which Q is the flow in L/min, C the capacitance $ml/mmHg$ and t the time in s. The pressure drop across the inductor is described in equation 2.7.

$$P = I \cdot \frac{dQ}{dt} \tag{2.7}$$

In which I is the inertance in $mHg \cdot ml/s^2$.

Ursino's model was replicated in Simulink, the code can be found in appendix A.

2.1.3 Mathematical modelling of the Baroreflex Response

One of the objectives of this study is to replicate the systemic component of the baroreflex, specifically by considering the parameters of resistance, HR, and contractility. The mathematical models describing these parameters were adapted from the work of Ursino, who incorporated the concept of elasticity as a measure of ventricular contractility [119]. His derivation of the baroreflex model is based on experimental research.

The experimental study conducted by Chapleau et al. [146] demonstrated that the afferent pathway of the baroreflex can be characterised as a linear derivative first-order

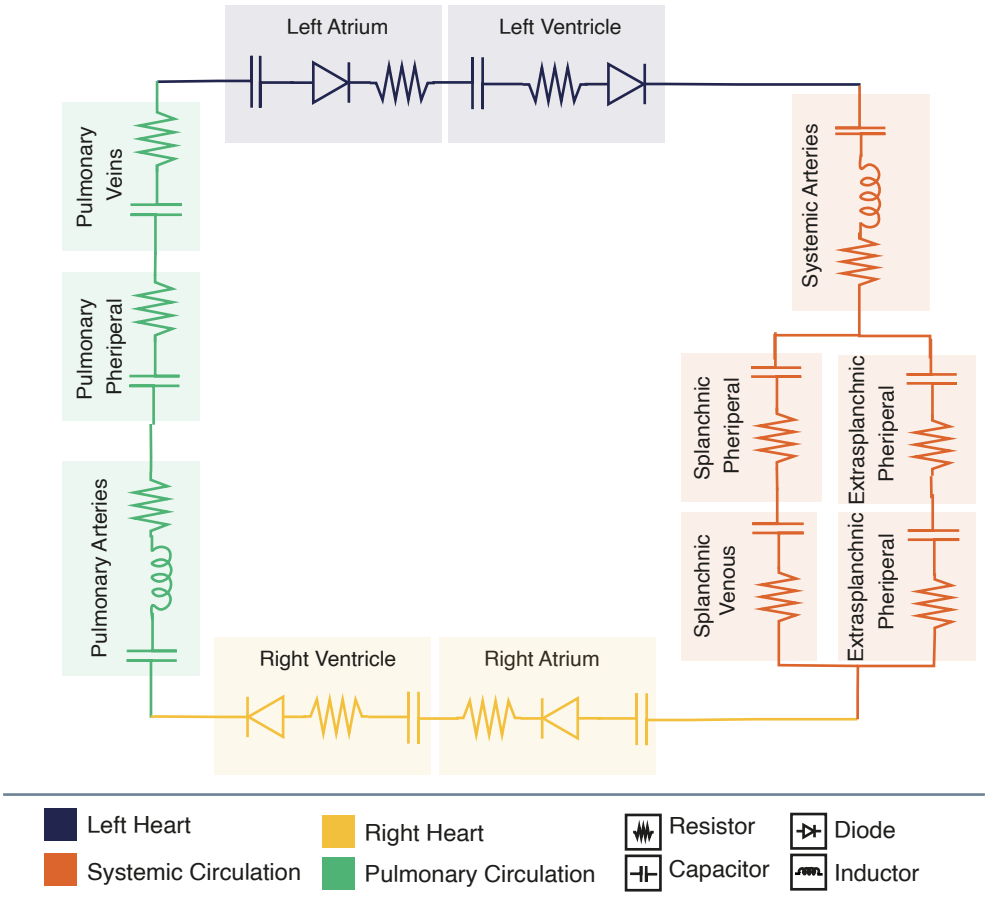

Figure 2.4: Ursino's analog model of the cardiovascular system, adapted from [119].

dynamic block, of which the input is carotid sinus pressure, in a series configuration with a sigmoidal static characteristic:

$$\tau_p \cdot \frac{P_{l,out}}{dt} = P_{cs} + \tau_z \cdot \frac{dP_{cs}}{dt} - P_{l,out} \tag{2.8}$$

In which, τ_z and τ_p are the time constants of the real zero and real pole which are $6.37s$ and $2.076s$ respectively, $P_{l,out}$ the output variable of the linear dynamic block which has the unit of pressure ($mmHg$) and P_{cs} is the carotid sinus pressure. As for the sigmoidal static characteristic:

$$f_{cs} = [f_{min} + f_{max} \cdot \exp(\frac{P_{l,out} - P_n}{k_a})]/[1 + \exp(\frac{P_{l,out} - P_n}{k_a})] \tag{2.9}$$

In which, f_{cs} is the frequency of spikes in the afferent pathway, f_{max} and f_{min} are the upper and lower limits of the frequency of neural discharge with values of $47.78spikes/s$ and $2.52spikes/s$ respectively, P_n represents the intrasinus pressure at the central point of the sigmoidal functional relationship with a value of $92mmHg$ and k_a is the slope of the sigmoidal function at the central point which is $11.158mmHg$.

The relationship between the activity levels of the afferent and efferent neural pathways (i.e. the efferent sympathetic pathway) of the baroreflex response follow a negative monotonic function, characterised by an exponential trend as established through experimental research [147]:

$$f_{es} = f_{es\infty} + (f_{es0} - f_{es\infty}) \cdot \exp(-k_{es} \cdot f_{cs}) \tag{2.10}$$

In which f_{es} is the frequency of spikes in the efferent sympathetic nerves and k_{es}, $f_{es}\infty$ and $f_{es,0}$ are constants of value $0.0675s$, $2.10spikes/s$ and $16.11spikes/s$ respectively.

The activity of the efferent vagal pathway shows a monotonic increase in relation to the activity in the sinus nerve, until an upper limit is reached. As a result, a sigmoidal equation has been employed to model this relationship:

$$f_{ev} = [f_{ev} + f_{ev\infty} \cdot \exp(\frac{f_{cs} - f_{cs0}}{k_{ev}})]/[1 + \exp(\frac{f_{cs} - f_{cs0}}{k_{ev}})] \tag{2.11}$$

In which f_{ev} is the frequency of spikes in the efferent vagal fibers and k_{ev}, $f_{ev,0}$, f_ev, ∞

and $f_{cs,0}$ are constant parameters with a value of $7.06 spikes/s$, $3.2 spikes/s$, $6.3 spikes/s$ and $2.5 spikes/s$ respectively.

The response of resistance (R_{sp}, resistance splanich peripheral and R_{ep}, resistance in the extrasplanich pheriperal), and cardiac elastance of the left ventricle (E_{lv}) to the activity in the efferent sympathetic pathway is characterised by a simple latency (i.e. the time delay between the onset of the detection of change in blood pressure and the initiation of neural activity), a monotonic logarithmic static function, and a low pass first-order dynamic component. Therefore, the following equation holds true:

$$\Theta(t) = \begin{cases} G_\Theta \cdot ln(f_{es}(t - D_\Theta) - f_{es,min} + 1), & \text{if } f_{es} \geq f_{es,min} \\ 0, & \text{if } f_{es} < f_{es,min} \end{cases} \tag{2.12}$$

In which Θ is the controlled parameter (resistance or cardiac elastance), σ_Θ is the output of the static function, D_Θ is the latency, respectively and G_Θ is the gain factor. The change, $\Delta\Theta$, of the parameter caused by sympathetic simulation is described as:

$$\frac{d\Delta\Theta}{dt}(t) = \frac{1}{\tau_\Theta} \cdot (-\Delta\Theta(t) + \sigma_\Theta(t)) \tag{2.13}$$

$$\Theta(t) = \Delta\Theta(t) + \Theta_0 \tag{2.14}$$

In which τ_Θ is the time constant of the controlled parameters.

The response of heart period is a result of the balance between vagal (T_v) and sympathetic (T_s) activities. The changes in heart period induced by sympathetic stimulation are derived similar to equations 2.12 and 2.13:

$$\sigma_{T,s}(t) = \begin{cases} G_{T,s} \cdot ln(f_{es}(t - D_{T,s}) - f_{es,min} + 1), & \text{if } f_{es} \geq f_{es,min} \\ 0, & \text{if } f_{es} < f_{es,min} \end{cases} \tag{2.15}$$

$$\frac{d\Delta T_s}{dt}(t) = \frac{1}{\tau_{T,s}} \cdot (-\Delta T_s(t) + \sigma_{T,s}(t)) \tag{2.16}$$

Following from Parker et al. [148] the HR change via vagal activity is given by:

$$\sigma_{T,v}(t) = G_{T,v} \cdot f_{ev}(t - D_{T,v}) \tag{2.17}$$

Table 2.1: Parameters of the Mathematical Model of the Baroreflex taken from Ursino [117].

Gain	Time Constant	Time Delay	Baseline Value
$G_{E_{lv}} = 0.475 mmHg/ml$	$\tau_{E_{lv}} = 8s$	$D_{E_{lv}} = 2s$	$E_{lv_0} = 2.392 mmHg/ml$
$G_{R_{sp}} = 0.695 mmHg \cdot s/ml$	$\tau_{R_{sp}} = 6s$	$D_{R_{sp}} = 2s$	$R_{sp_0} = 2.49 mmHg \cdot s/ml$
$G_{R_{ep}} = 0.53 mmHg \cdot s/ml$	$\tau_{R_{ep}} = 6s$	$D_{R_{ep}} = 2s$	$R_{ep_0} = 0.78 mmHg/ml$
$G_{T_s} = -0.13s$	$\tau_{T_s} = 2s$	$D_{T_s} = 2s$	$T_0 = 0.58 mmHg/ml$
$G_{T_v} = 0.09s$	$\tau_{T_v} = 1.5s$	$D_{T_v} = 0.2s$	

$$\frac{d\Delta T_V}{dt}(t) = \frac{1}{\tau_{T,V}} \cdot (-\Delta T_V(t) + \sigma_{T,V}(t)) \tag{2.18}$$

Assumed is a linear relationship between the sympathetic and vagal activities hence the total HR is calculated as:

$$T = \Delta T_s + \Delta T_V + T_0 \tag{2.19}$$

The parameters of the regulators are given in table 2.1, taken from Ursino [119].

The aforementioned equations have been adapted and integrated, as part of this study, into a LabVIEW model (the simulation and control toolbox is required to implement this model). The full program can be found in appendix B.

2.1.4 Machine learning techniques

As part of the development of the MCL machine learning was used to estimate cardiovascular parameters. Machine learning is a computational technique that allows machine learning algorithms to acquire information directly from data. A schematic of a typical machine learning workflow is presented in figure 2.5, which begins with data collection and importation. The performance of the machine learning algorithm improves as more data are provided. Following data collection, the data are explored, and features are extracted. A feature is an individual measurable property or characteristic of a phenomenon. After data exploration and feature extraction, appropriate models are constructed and evaluated. This process is repeated until the optimal model is identified, which is subsequently deployed for use.

Two primary categories of machine learning techniques exist: supervised learning and unsupervised learning. Supervised learning employs known input-output pairs to

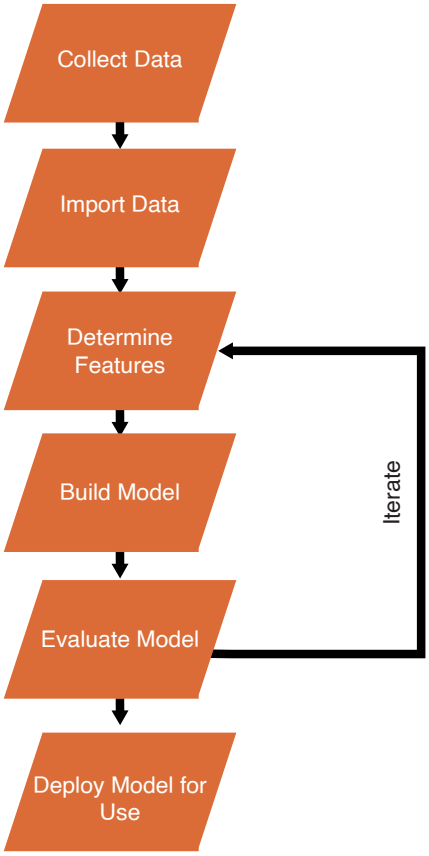

Figure 2.5: Typical classification workflow: data collection, exploration, feature extraction, model construction, training and evaluation, iterative improvement for optimal model, used for classification tasks.

train a model for future output prediction. On the other hand, unsupervised learning aims to discover patterns and structures in data without any pre-specified output. The present work focuses on supervised techniques, specifically regression techniques, which predicts continuous responses.

Linear regression Linear regression models describe the relation between a dependent variable y and one or more independent variables, x. Linear regression plays a key role in statistics by providing a simple yet powerful method for modelling the relationship between variables and making predictions based on that relationship. Simple linear regression includes only one predictor variable and its estimated regression model can be represented with:

$$y = \beta_0 + \beta_1 X_{1i} \tag{2.20}$$

A multiple linear regression model is described as:

$$y_i = \beta_0 + \beta_1 X_{i1} + \cdots + \beta_p X_{ip} + \epsilon_i, i = 1, \cdots, n \tag{2.21}$$

In which y_i is the ith response, β_k is the kth coefficient, where β_0 is the constant term in the model, X_{ij} is the ith observation on the jth predictor variable ($j = 1, \cdots, p$) and ϵ_i is the ith noise term, random error.

Gaussian process regression Regression techniques can be used to fill in the gaps between data points and obtain a continuous function representation that can be used for further analysis. Linear regression is a commonly used example of these techniques, but it is limited to low-dimensional data and cases where the observations have low noise.

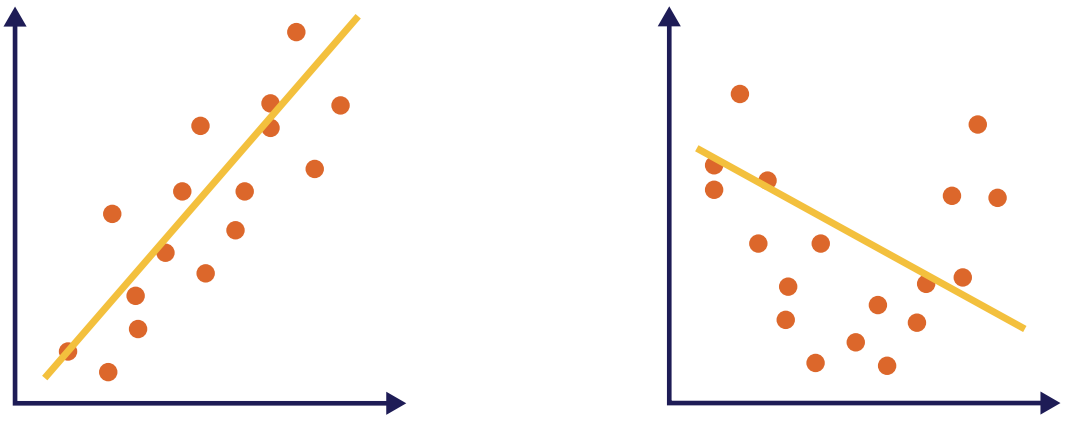

(a) Example data one (b) Example data two

Figure 2.6: Two examples in which the data are assumed to follow a linear relationship.

Gaussian process regression (GPR) is a nonparametric and nonlinear regression tool that is useful for interpolating between data points in high-dimensional input spaces. Unlike linear regression, which assumes a specific formula and finds the best fitting coefficients, GPR finds a distribution over the possible functions that are consistent with the observed data.

For instance, in figure 2.6, it is evident that the data in (a) follows a linear trend, while the data in (b) should follow parabolic trend. One can change the regression model to a parabolic trend and repeat the process to find the correct relationship. However, it would be preferable to avoid making assumptions about the formula and let the regres-

sion find the best function automatically, which is precisely what GPR does. GPR has several benefits, including its ability to work well on small data sets and provide uncertainty measurements on the predictions [149].

Support vector regression Support vector regression is a linear model for regression problems. It can handle both linear and non-linear problems and is widely used in practical applications. The algorithm creates a line or a hyperplane to divide the data into classes. There are frequently several hyperplanes that can achieve the separation required for support vector regression. These hyperplanes are illustrated in Figure 2.7. In order to identify the optimal hyperplane, support vector regression identifies the points closest to the hyperplane from both classes, which are referred to as support vectors. The distance between the hyperplane and the support vectors is called the margin, and the objective of support vector regression is to maximise this margin. Therefore, the hyperplane that maximises the margin is chosen as the optimal hyperplane for separating the two classes.

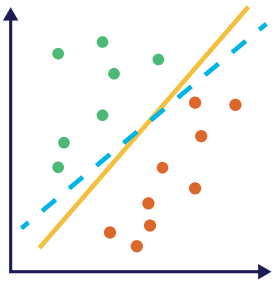

Figure 2.7: The data can be seperated with multiple hyperplanes.

The thesis does not provide detailed mathematical equations for GPR and support vector regression, as it is not within its scope. Additionally, the use of the MATLAB toolbox allowed for practical implementation without the need for diving into mathematical details.

Feature selection The goal of feature selection techniques in machine learning is to find the best set of features that allow us to build optimised models of the studied phenomena.

Correlation Correlation is a measure of the linear relationship between two or more variables. Through correlation, we can predict one variable from the other. The logic behind using correlation for feature selection is that good variables correlate highly with the target. Furthermore, variables should be correlated with the target but uncorrelated among themselves. If two variables are correlated, we can predict one from the other. Therefore, if two features are correlated, the model only needs one, as the second does not add additional information.

Forward Feature Selection Using forward feature selection, the most optimal features are selected. Forward feature selection is an iterative method wherein we start with the performing features against the target features. Next, we select another variable that gives the best performance in combination with the first selected variable. This process continues until the preset criterion is achieved.

2.2 Experimental Methods

The MCL is a carefully designed test bench used to understand and verify theoretical concepts of the CVS and to evaluate the performance of CADs. The MCL consists of a closed loop system of instruments and sensors that are used to resemble physiological parameters, such as blood flow and pressure. The data collected from these sensors are collected and processed using a data acquisition system. Additionally, a program is required to enable the user to control the instrumentation, and visualise and record the data. This 'experimental' section contains a detailed description of the instruments and sensors used in the MCL for this study, the calibration process for the sensors, and a description of the various components of the MCL.

2.2.1 Measurement and Calibration of Pressure and Flow Sensors

To ensure the accuracy and reliability of the MCL, it is important to carefully consider the specifications of the instrumentation and sensors. It is important to recognise that there may be uncertainty in these sensors, potentially due to errors in the calibration process or the assumption of a linear relationship between the input and output of the

measurement system. To minimise these errors, it is important to carefully calibrate the sensors and to consider any potential sources of systematic error in the data.

2.2.1.1 Errors

The error is defined as the difference between the true and measured value. $error = measuredvalue - truevalue$. The relative error provides a measure of the error in relation to the true value and is expressed as a percentage: $relativeerror = \frac{error}{truevalue} 100\%$ The uncertainty is the margin of doubt existing in the measurand as well as the significance of it.

2.2.1.2 Calibration

In the MCL, the sensors are calibrated to convert their output values into numerical values that accurately reflect the physiological parameters being measured. This is done by creating a calibration curve, which is a graphical representation of the relationship between the "true" value of the measurand and the output value of the measuring system. The true value of the measurand is determined independently of the MCL, and is used as a reference point for the calibration process. Once the true values and the output values have been recorded, a curve is fitted to the data, and this curve is then used to convert the output values of the measurement system into numerical values.

2.2.1.3 Pressure calibration

The pressure inside the MCL is measured using pressure catheters from Gaeltec (Gaeltec Devices Ltd, UK). The pressure catheter senses pressure upon the deformation strain or change in length of a copper wire. The output of the pressure catheters is in voltage, thus a calibration curve is needed to convert this voltage into pressure.

The pressure catheters were calibrated using hydrostatic pressure which is defined as:

$$P = h \cdot g \cdot \rho \tag{2.22}$$

In which h is the height in meters, g the gravitational acceleration constant, ρ the density in kg/m^3 and P the hydrostatic pressure in Pascal.

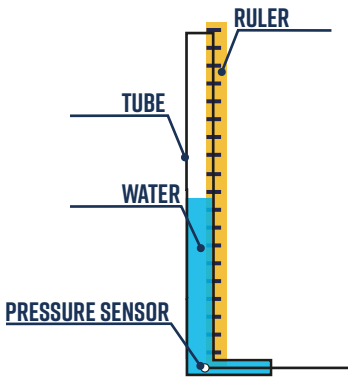

Figure 2.8: Calibration set-up of the pressure sensor.

The pressure sensors were calibrated using the experimental set-up from figure 2.8 which comprises a tube filled with water and a ruler. The pressure sensor was inserted at the bottom of the tube. Numerous ($N > 10$) measurements were taken at different water heights. The true pressure value was calculated using equation 2.22 and converted to millimeters mercury using the ration $1Pa : 0.0075mmHg$.

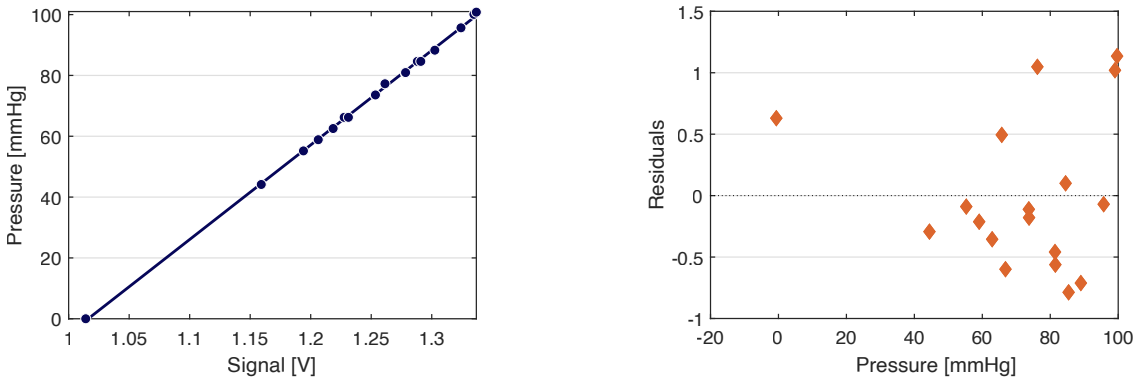

(a) Calibration curve (b) Residual plot

Figure 2.9: Calibration curve and residual plot of the pressure sensor Gaeltec model F6 (y = ax+b, R-squared 0.99).

Figure 2.9 shows the calibration curve (a) and residual (b) of one of the 6F Gaeltec pressure sensor. The accuracy of the ruler used to determine the hydrostatic pressure is up to $\pm 2.5cm$. This means that the uncertainty in the pressure sensors calibration is $\pm 1.8mmHg$.

For the experiments two pressure sensors were used the Gaeltech F6 and X04, calibrated in the same manner, with calibration curves of $P = 305 * V - 308$ and $P = 296 * V - 299$ respectively. In which P is the pressure in $mmHg$ and V is the measured

signal. These sensors were chosen simply because they were available in the lab.

2.2.1.4 Flow calibration

The flow is measured using ultrasonic flow probes (Transonic,USA) which measure the flow using transit-time ultrasound technology. The flow probe has four transducers, two upstream and two downstream. An electrical excitation causes the downstream transducers to emit an ultrasound wave to the upstream transducers where it is converted into an electrical signal. The same cycle is repeated for the upstream transducer. The flow is determined from the transit time difference between the upstream and downstream cycle.

Two different types of flow probes were used: in-line and clamp-on. The in-line flow probes are inserted into the MCL in series by connecting the inlet and outlet of the flow probe with tubing. The clamp-on flow probes are clamped on the outside of the tube. As the transit time for the clamp-on flow probes differs for different tube, the flow probe needs to be recalibrated when a different tube is used.

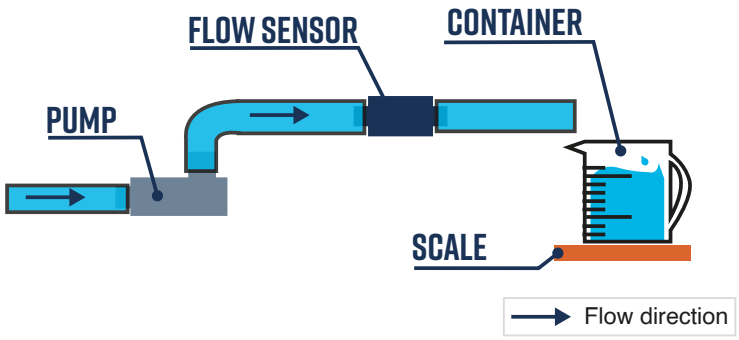

Figure 2.10: Experimental set-up to calibrate flow meters comprising of the continuous flow pump, the flow meter, a reservoir and a scale.

The flow probes were calibrated using a static calibration method in which fluid was collected in a container via a tube and the volume of fluid was determined using a scale. The flow meters were connected to the tube and the tube was connected to a centrifugal flow pump. The flow was calculated from the time it takes to fill to the container. The experimental set-up is illustrated in figure 2.10.

A scale (10877SSDR, Salter, UK) was used to determine the volume of water. As the

error of the scale was unknown it was determined by comparison method to a high precision scale (Ranger OHAUS, uncertainty = $0.5g$). Figure 2.11 shows the residuals of the Salter scale. The Salter scale shows a maximum error of $10g$.

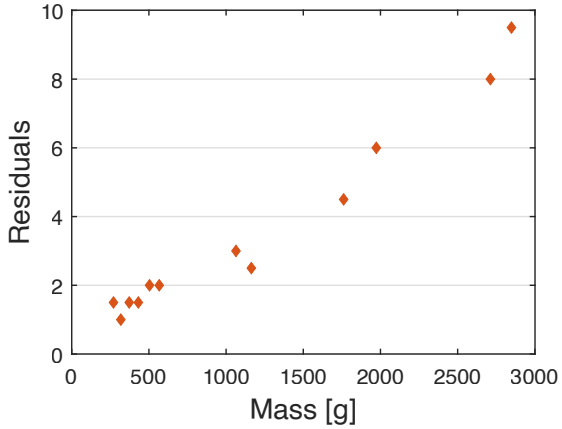

Figure 2.11: Residuals of the Salter scale.

Figure 2.12 shows the calibration curve (a) and residuals (b) of one of the PXN 25 Transonic flow meter. From the Transonic website it was found that the flow meters's relative error is $\pm 10\%$.

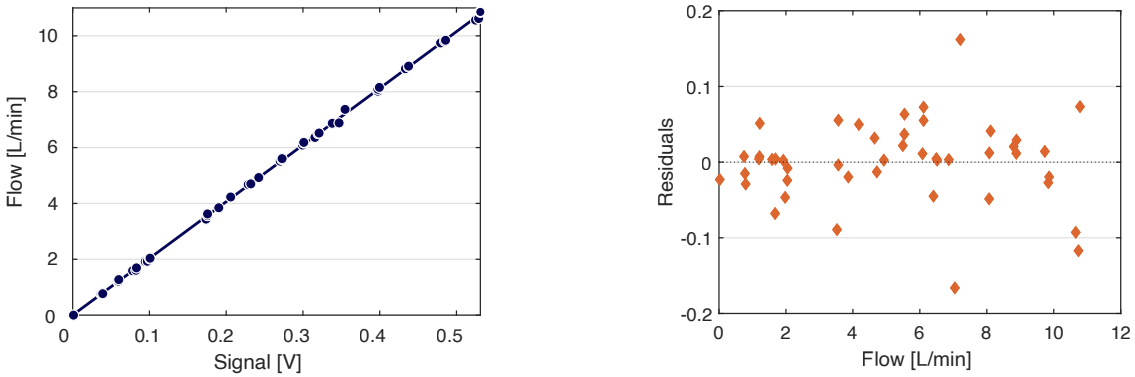

(a) Calibration curve

(b) Residual plot

Figure 2.12: Calibration curve (left) and residual plot (right) of Transonic flow meter (model:PXN25) fitted with a linear regression model (y = ax+b, R-squared 1).

For the experiments two flow sensors were used the transonic PXN25 an 16A9442 with calibration curves of $Q = 20 * V$ and $Q = 1.2 * V + 0.2$ respectively. In which Q is the flow in L/min and V is the measured signal.

2.2.2 Experimental Equipment: The Building Blocks of the Mock Loop

Experimental equipment of the MCL typically includes components such as pumps, reservoirs, and tubing, which are used to create a closed-loop system that mimics the flow of blood through the human body. This section contains detailed information on the equipment used to build the MCL.

2.2.2.1 The Left Ventricle Simulator

The left ventricle simulator comprises of a reservoir, two one-way valves, and a linear motor (P01, LinMot & MagSpring, Switzerland) developed by MagAssist China, illustrated in figure 2.13. The reservoir has a diameter of $75mm$ and a height of $70mm$. The inlet and outlet of a diameter of $22mm$. The reservoir is closed off using a flexible membrane. The linear motor pushes on the membrane to force liquid out of the reservoir via the aortic valve. Upon raising the linear motor, the reservoir fills via the mitral valve. The end diastolic volume (EDV) of the ventricle is $310ml$, the linear motor can move up to a stroke length (i.e. the distance the linear motor travels from the top of the membrane to the end of systole) of $30mm$.

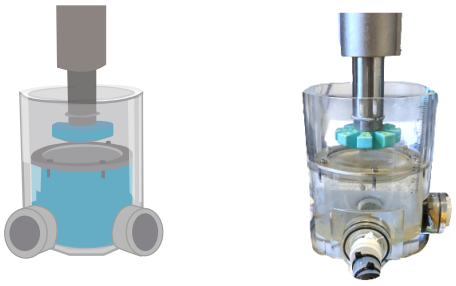

(a) Schematics (b) Photograph

Figure 2.13: The left ventricle simulator comprising of a reservoir closed off by a flexible membrane, two one-way valves and a linear motor.

In order to operate the linear motor with a cycle motion profile, a LabVIEW program was developed as part of this study. This program allows for the control of both HR and stroke length. The flowchart for the program is shown in figure 2.14. The program begins by establishing a connection between the linear motor and LabVIEW. Following this, the linear motor is "homed," meaning moved to a reference position to establish a reference

point for subsequent motion. Once the linear motor has been initialised, it is ready to initiate motion. Input parameters for HR and stroke length are provided to the program, which subsequently calculates the required velocity and acceleration. The motor then moves to its diastolic and systolic positions as part of the cycle motion. If a user selects the "stop" button in the user interface, the motion will terminate and the linear motor will be disconnected from LabVIEW. The LabVIEW code of this program is given in appendix C.

2.2.2.2 The Automated Vascular Resistor

The blood vessel resistance, which is regulated by a change in vessels diameter, plays a critical role in the baroreflex response to help regulate blood pressure, as described in section 1.1.0.3. Therefore an automated vascular resistor was designed in this study to control the resistance in the MCL. The M-122 Precision Micro-Translation Stage (Physik Instrumente, Germany) is a key component of the automated vascular resistor. This device can move over one axis in a range of 25 mm with a minimum incremental motion of 0.2 μm. It is connected to the PC via the C-863 Mercury Controller (Physik Instrumente, Germany). The manufacturer provides numerous LabVIEW virtual instruments (VIs) to control the position and movement of the translation stage, these VIs are incorporated into our code.

To hold the translation stage in place, a 3D-printed case was designed. The top section of the case holds the translation stage and the bottom section houses the tube. Attached to the mounting plate of the translation stage is a pusher, which will push into the tube, reducing the cross-sectional area and increasing the resistance (or vice versa). The case and pusher were printed using VeroWhite resin on a Polyjet (objet) printer. The assembly can be seen in figure 2.16. The technical drawings for both can be found in appendix D.

In order to control the resistance in the MCL, a control program was developed using LabVIEW. This program is designed to continuously monitor the pressure and flow through the MCL and adjust the resistor as needed to maintain the desired set point. The control program for continuous flow, figure 2.17, differs slightly from that used for pulsatile flow, figure E.1. When the program is started, measurements of pressure and flow are taken from the MCL setup. Two pressure measurements are recorded, one upstream and one downstream from the resistor, while the flow is measured upstream

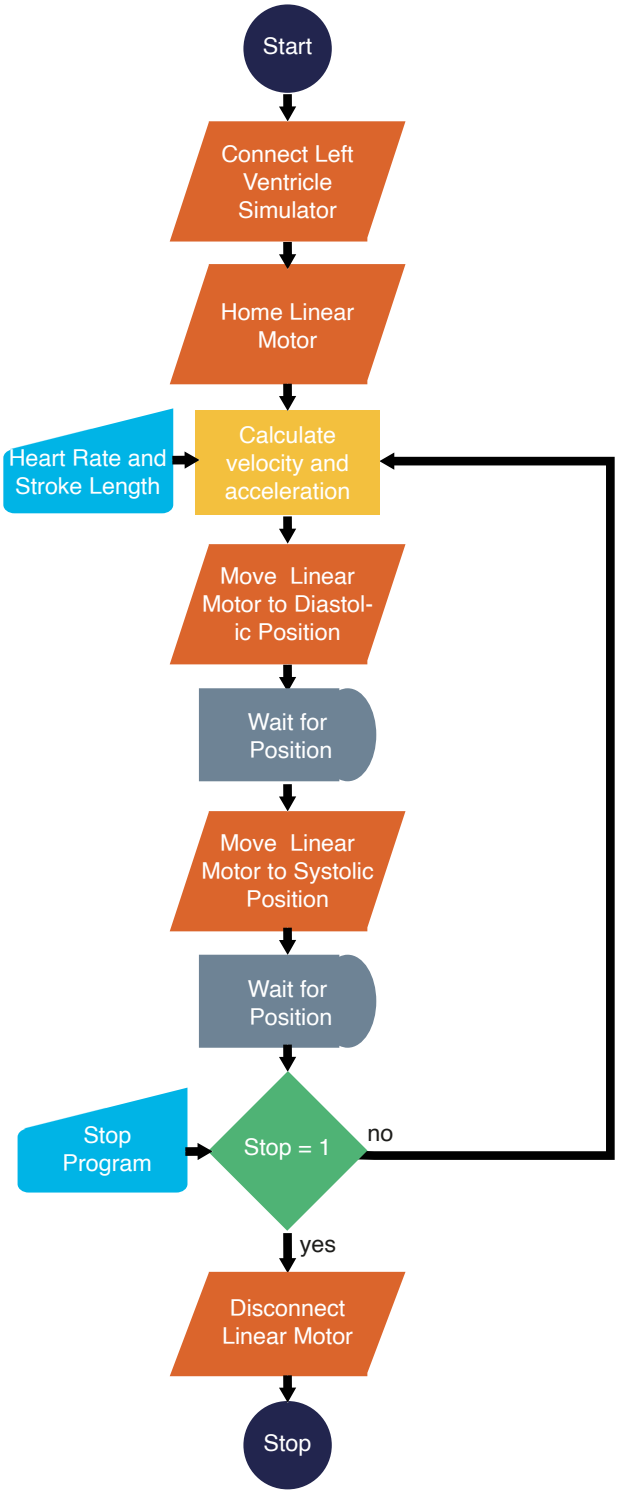

Figure 2.14: Flow chart of the LabVIEW program to operate the linear motor in a cyclic motion profile.

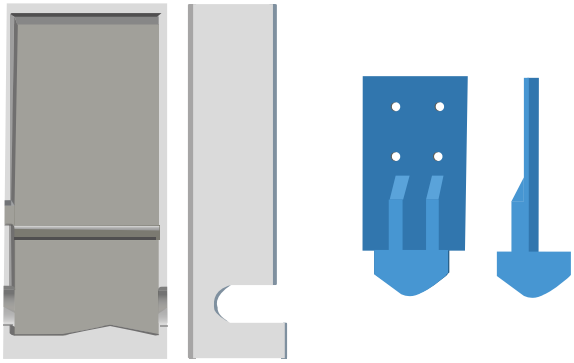

Figure 2.15: Image of the case and pusher of the resistor

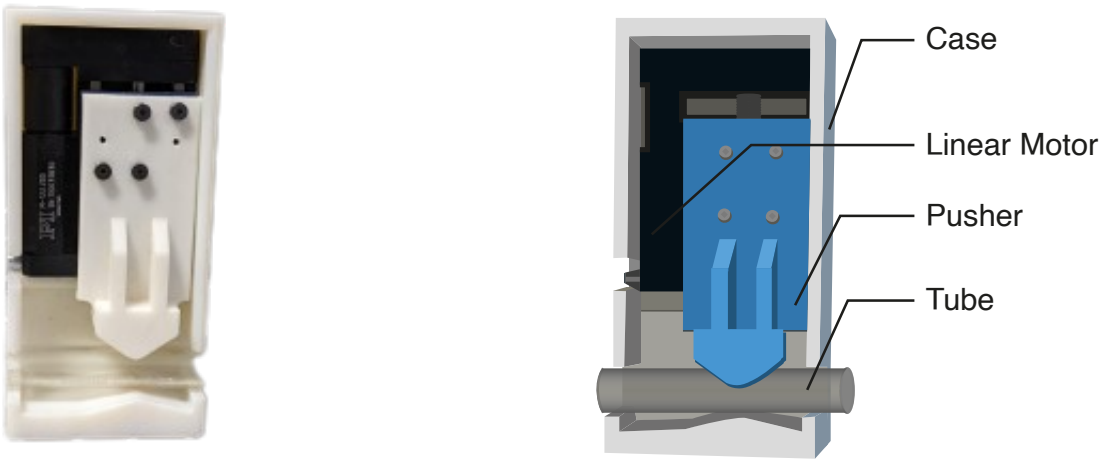

(a) Photograph of the assembled resistor. (b) Example data two

Figure 2.16: Image of the assembled design of the resistor.

from the resistor using an inline flow probe. The resistance is then calculated using these measurements (equation 2.2), and the error between the current resistance and the set-point resistance is determined. The set-point resistance can be user-defined or obtained from a numerical model. In order to minimise errors, the resistor will only be adjusted if the difference between the set-point resistance and the current resistance is greater than 12% of the set-point value, taking into account the uncertainty of the pressure sensors ($\pm 2\%$) and the relative error of the inline flow meter ($\pm 10\%$).

If the error is greater than 12%, the control program will adjust the size of the resistor in order to correct the error. If the error is positive, meaning the current resistance in the MCL is bigger than the set-point, the program will increase the diameter of the tube. Depending on the size of the relative error the resistor will move with 0.5, 0.2, 0.1 or $0.05mm$. While if the error is negative, it will decrease the diameter in a similar manner. A full overview of the control system is given in figure 2.18. For pulsatile flow, the resistance

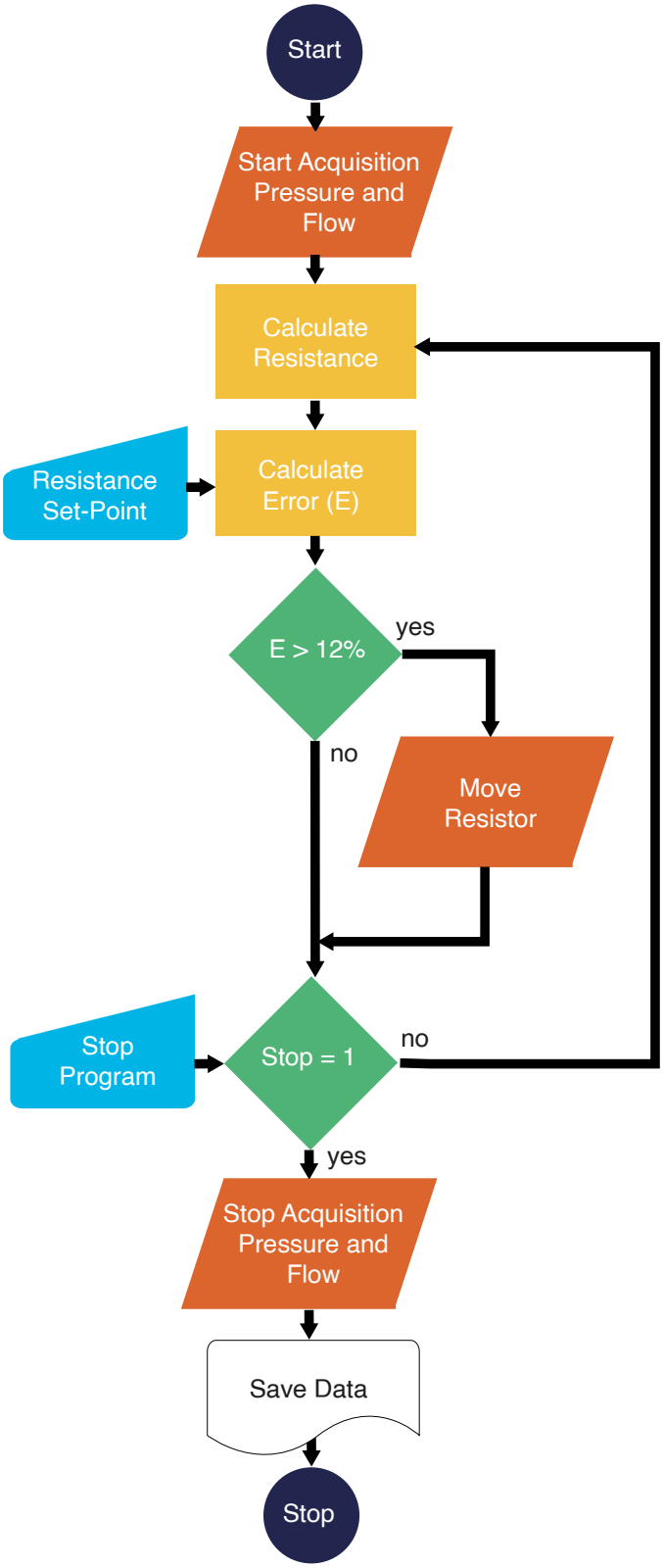

Figure 2.17: Flowchart for the control program of the resistor during continuous flow conditions.

is calculated per heart beat by taking the mean pressure difference and the mean flow, which can be seen in appendix E.The LabVIEW code of the resistor is shown in appendix F.

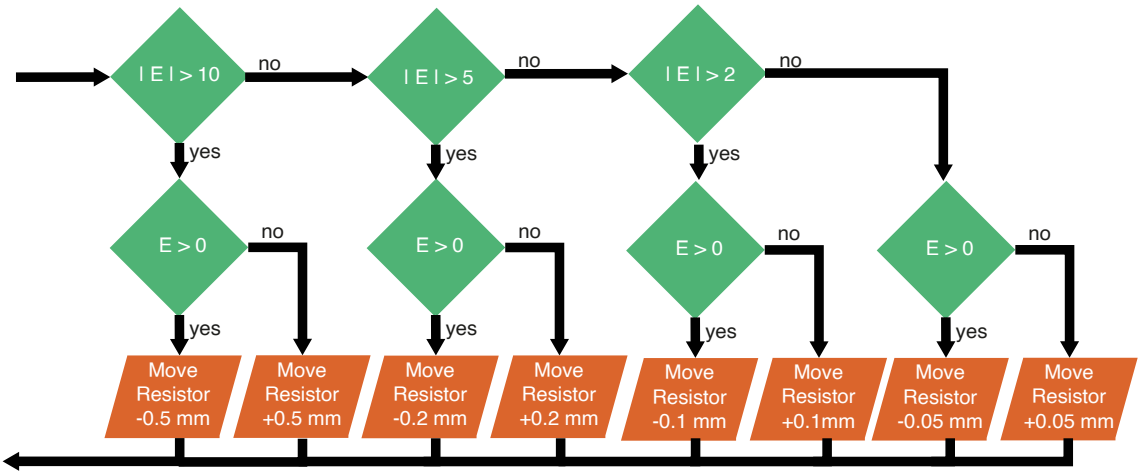

Figure 2.18: The magnitude of displacement of the resistor depends on the absolute size of the error. The larger the error the larger the displacement or vice versa.

2.2.2.3 Other Laboratory Equipment

Table 2.2 provides an overview of other experimental equipment used to build the MCL. Firstly, the open reservoir is used as atria. The open reservoir has a diameter of $25cm$ and a height of $24cm$. The initial pressure in the system can be adjusted by adding water to this reservoir. Furthermore, an upside down bottle is used as a closed compliance chamber. The diameter of this bottle is $6cm$ and it is $8cm$ in height. The compliance can be adjusted by adding or reducing the water to air ratio. Lastly, the components are connected via flexible tubing. There are various sizes of tubes made out of different materials in the lab.

2.3 The Full Hybrid Set-Up

A hybrid testing platform will be established through the integration of a hydraulic MCL and the numerical baroreflex model programmed in LabVIEW. A schematic representation of the hydraulic component of the MCL is provided in figure 2.19. the MCL depicted

Table 2.2: Other Experimental Equipment

Open reservoir	Compliance chamber	Various flexible tubes
		

in the figure consists of the following fundamental elements, the left ventricle simulator, the automated vascular resistance, a compliance, and a reservoir. The left ventricle simulator and the resistance are computer-controlled, thus capable of communicating with the numerical baroreflex model. The pressure and flow within the system will be continuously monitored using the earlier described pressure catheters and inline flow probe.

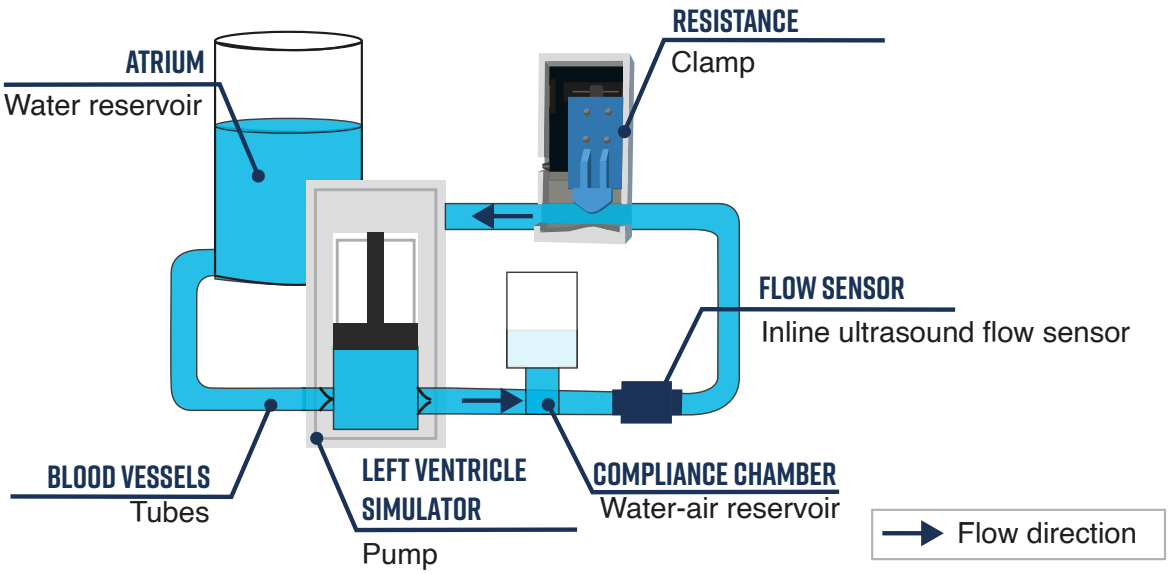

Figure 2.19: The hybrid mock loop

The components are connected with silicon tubes. The tube connecting the left ventricle to the flow sensor and compliance chamber has a length of $240mm$ and a diameter of $12mm$. From the flow probe follows a series of tubes with length of $1400mm$, $180mm$ and $800mm$ and diameter of $25mm$, $15mm$ and $12mm$, respectively. Similar to the diameter of

the aortic root ($25mm$) and large arteries ($1-2cm$) [143].

The resistance of these series of tubes can be calculated using the Hagen-Poiseuille equation, which is valid for Newtonian fluids in straight, uniform tube whose length is larger than the width. Using equation 2.2, the Hagen-Poiseille equation can be rewritten to:

$$R = \frac{8 \cdot \eta \cdot L}{\pi \cdot r^4} \tag{2.23}$$

In which η is the viscosity of the fluid, which for water at 20 degrees Celsius is approximately $0.001 Pa \cdot s$ [150], L the length of the tube in mm and r the radius of the tube in mm. The total resistance of the series of tubes is the sum of the resistance of each individual tube. Therefore total resistance of the tubes is approximately equal to $2.3 \cdot 10^6 Pa/m^3$ which is equal to $2.9 \cdot 10^{-4} mmHg \cdot min/mL$. Similar to our CVS system the resistance of the larger arteries are negligible [143].

Positioned on the last tube ($L = 800mm, D = 12mm$) sits the automated hydraulic resistor. The resistor is able to reduce the inner diameter of the tube with steps as little as 0.2 μm. Therefore, the theoretical resistance can be varied over a range from $2.9 \cdot 10^{-4} mmHg \cdot min/mL$ (open) to $\infty\ mmHg \cdot min/mL$ (fully closed). Given that the systemic resistance of the CVS at rest is $0.02 mmHg \cdot min/mL$ this set of tubes and the resistor are suitable to represent the systemic arteries.

The flow sensor was placed immediately after the aortic compliance chamber, resulting in a smoother wave pattern compared to when it was positioned before the chamber. A pressure sensor was positioned between the aortic compliance chamber and the flow sensor to accurately measure the arterial pressure which serves as the input parameter to the baroreflex model. Additionally, a pressure sensor was positioned in close proximity to the reservoir to assess the pressure downstream from the hydraulic resistor. The magnitude of the hydraulic resistance was calculated as the difference between the readings obtained from the downstream pressure sensor and the aortic pressure sensor. This value was used to regulate and control the automated hydraulic resistor.

The analogue signals were collected with a rack-mount BNC-2090 (National Instruments, USA) and converted to digital signals using the USB-6361 (National Instruments, USA). The sampling rate was regulated by placing the NI-DAQmx data read inside a time-based loop, which was controlled by the system's time sources to run at the desired

frequency. This method allowed the data acquisition to run at a higher frequency and priority compared to data logging and visualization. Using parallel timed loops and while loops will enhance the execution speed and break down the program into smaller processes. This will increase the processing speed of each small process, leading to an overall increase in the application's execution rate, as opposed to having the entire program run in a single loop. Therefore, other subVIs such as the control of the resistor and left ventricle simulator are positioned in separate time-based loops so they are time aligned and prioritised accordingly.

The data acquisition loop, left ventricle simulator and the baroreflex model are given the highest priority, as they are required to run in real-time at a frequency of 100Hz to accurately model and capture the response of the CVS. The data visualisation, data logging and control of the resistor are positioned in a lower priority loop, executing once a heart beat has finished. This gives the system time to settle, to not affect the stability of the control system of the resistor.

Under optimal conditions, the data collection needs to be carried out at a frequency of 1000Hz in order to obtain precise recordings of the pressure and flow wave forms. Nevertheless, when the baroreflex model was activated, the performance of the computer proved adequate in terms of processing the incoming data.

The user interface of the mock loop was develop in LabVIEW and shown in figure 2.20 and 2.21. The interface includes detailed description on how to set-up the mock loop for use. The full set-up in the lab is shown in figure 2.22 and 2.23.

The Main User Interface of the Developed LabVIEW Program

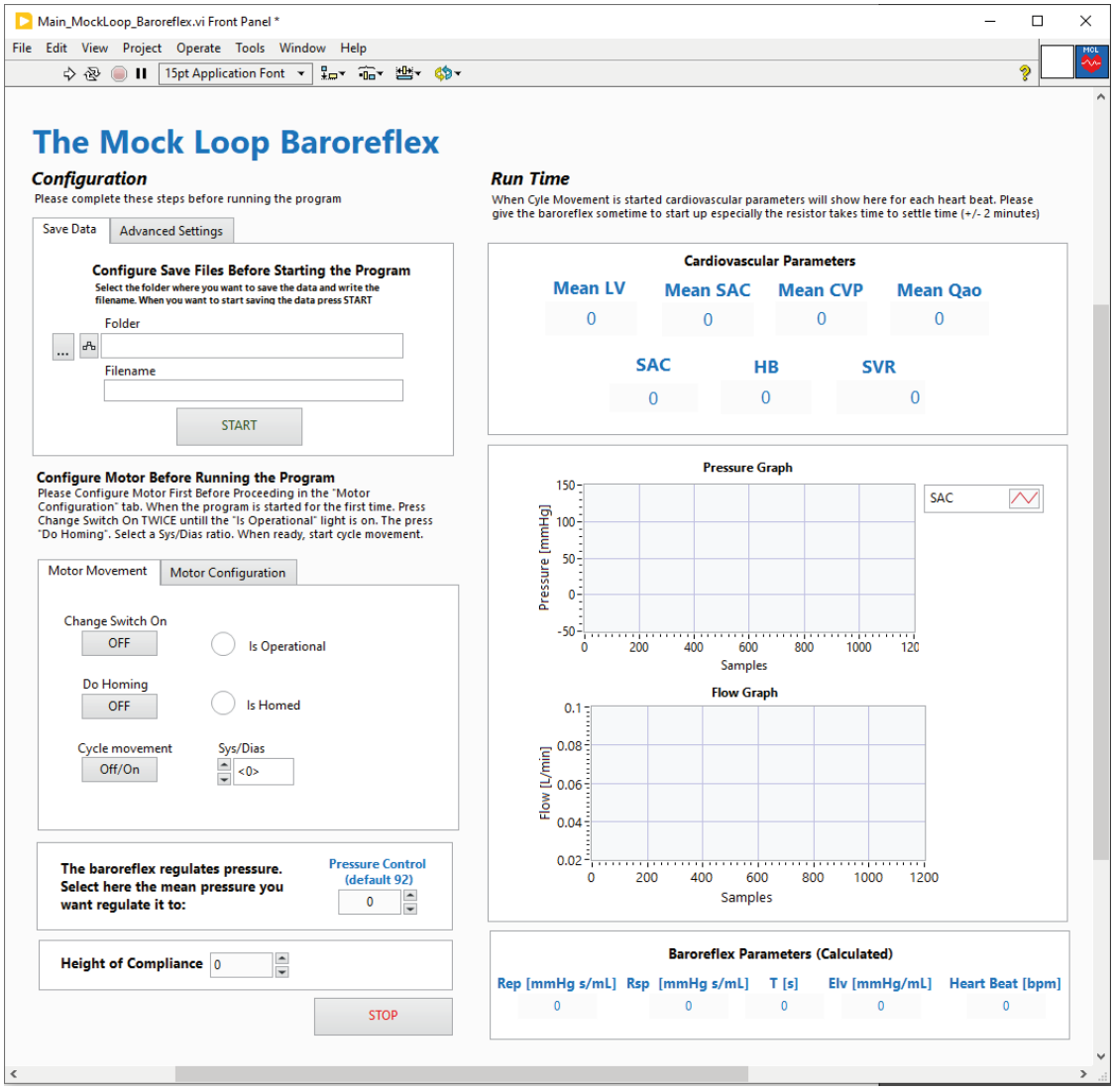

Configuration Settings: Save Data

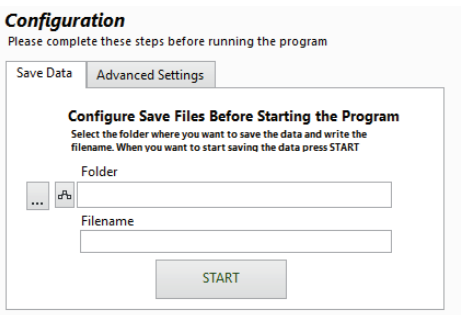

Configuration Settings: Advanced Settings

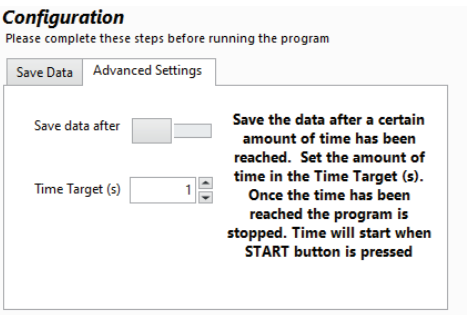

Figure 2.20: The user interface of the mock loop

Configuration Settings: Left Ventricle Motor Movement

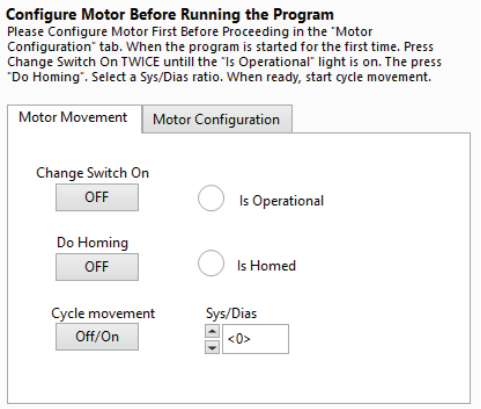

Configuration Settings: Motor Configuration

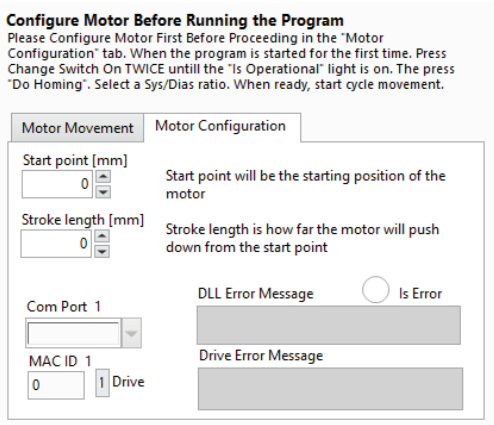

Configuration Settings: Baroreflex Control Settings

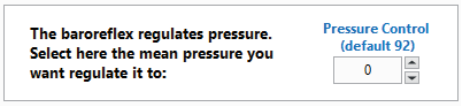

Configuration Settings: Compliance

Run Time: Cardiovascular Parameters

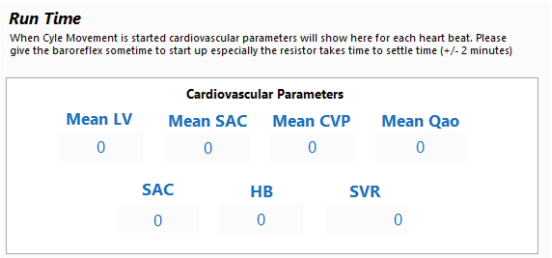

Run Time: Numerical Baroreflex Parameters

Figure 2.21: The user interface of the mock loop

Automated Vascular Resistor

Left Ventricle Simulator

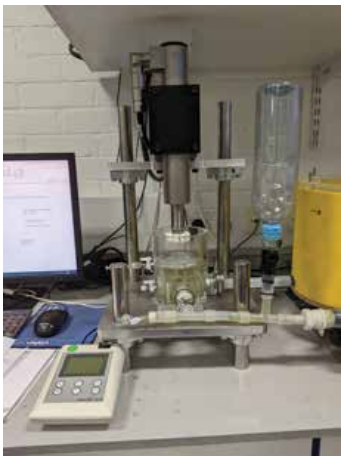

Reservoir

Full Lab Set-Up

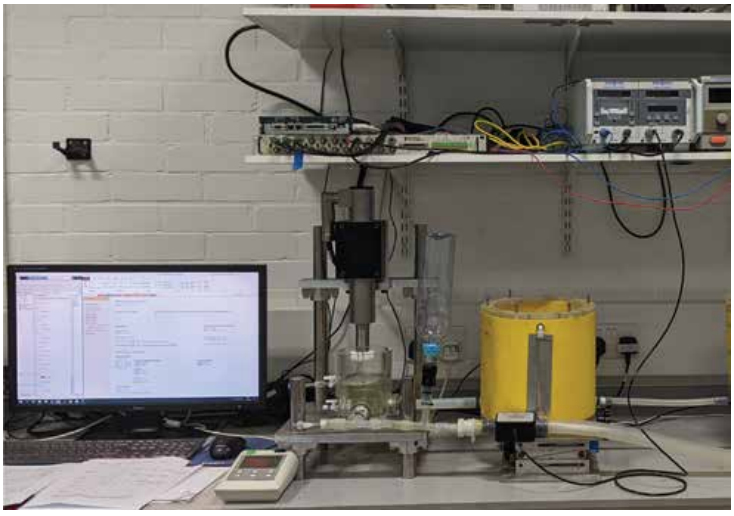

Figure 2.22: The full lab set-up

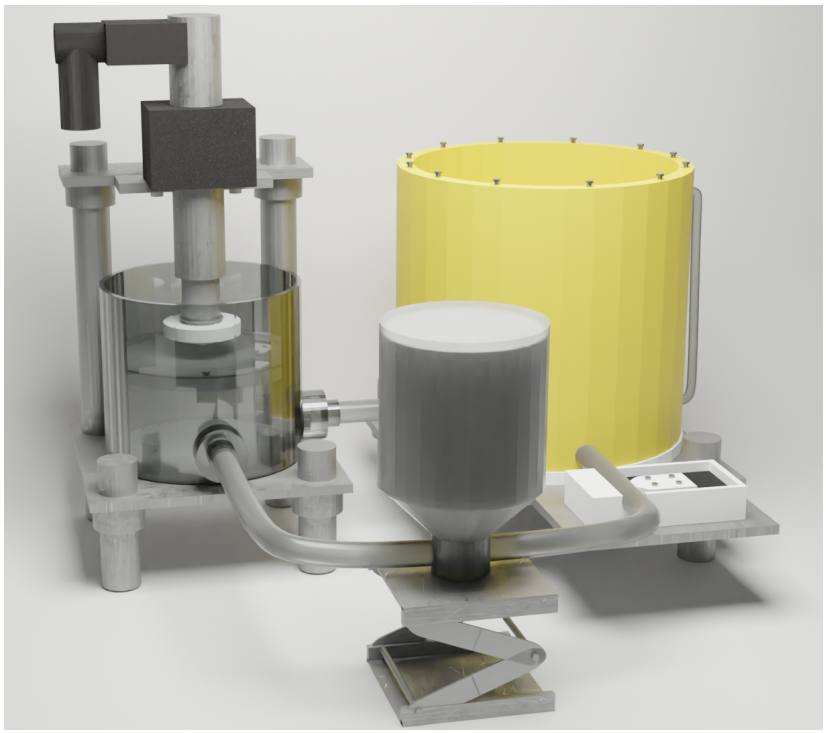

Figure 2.23: A 3D view of the mock loop

Chapter 3

Control of the Cardiac Output: The Left Ventricle Simulator

3.1 Introduction

Cardiac output is one the parameters regulated by the baroreflex, therefore this chapter presents the regulation of the cardiac output in the MCL. [1] The cardiac output is regulated by controlling the HR and contractility of the left ventricle. The control strategy for HR depended on the design of the left ventricle simulator. Notably, Mushi et al. achieved HR control of the baroreflex response by changing the pump speed of a continuous pump, which could be varied between 500 to 2750 rpm [120]. Schampaert et al. used a piston pump in which the velocity of the piston is used to control the HR [137], similarly to Jansen-Park et al. [121]. However, often the strategy for HR control remains unspecified [127], or HR control is disregarded in the simulation of the baroreflex response. [73], [106], [118]. In this context, the study aims to regulate HR using the displacement and velocity of the linear motor.

Next to HR ventricle contractility is also a control parameter of the baroreflex response. In MCLs ventricle contractility is simulated by adopting the elastance model of Baleo et al. [63], Sagawa et al. [68] or the model of Colacion et al.[73]. For example, Fresiello used the elastance model of Sagawa et al. to control the elastance of their numerical left ventricle [129]. Nonetheless, in the context of baroreflex, the capability to

[1] Part of this chapter is presented at the European society of artificial organs in F. Cappon, A.W. Khir, P.-L. Hsu, X. Du. "O20 - A novel machine learning model for predicting ventricular SV in a mock circulatory loop," The International Journal of Artificial Organs, vol. 45, no. 9, pp. 755–745,2022 [151]

regulate mechanical left ventricle contractility has been realised solely by Jansen-Park [121]. This has been accomplished through the use of a 3D lookup table, derived from experimental data encompassing all system states. This pioneering approach highlighted the potential of the control of contractility within MCL, however, the use of lookup tables has its limitations such as a limited resolution, challenges generalization and lack of adaptability. Therefore, the second objective of this study is the development of a ventricle contractility control system for the left ventricle simulator.

Assessing ventricular contractility requires measuring ventricular volume and pressure. The method for measuring ventricular volume in a MCL depends on its particular design and available instrumentation. For piston pumps, volume is often measured by multiplying the piston displacement by the constant piston area [43], [63], [133]. Other studies have used volume catheters [72], [90], sonomicrometry crystals to determine volume based on the distance between sensors [50], or magnetic level sensors when feasible [76], [98]. If direct measurement of ventricular volume is not an option, it can be calculated from aortic flow and arterial flow returning to the ventricle based on known initial volume [135], or it can be calculated using a mathematical model [41], [48]. In a ventricle with a complex and time-varying shape, real-time measurement and mathematical modelling of ventricular volume is challenging and computationally expensive. Here, the possible usefulness of machine learning models becomes an encouraging approach to overcome these challenges. As a result, the last objective of this study is to find out the ventricle volume using a machine learning model.

3.2 Methodology

The methodology section is divided into the HR and ventricle contractility.

3.2.1 Heart Rate

The HR of the left ventricle simulator is controlled via the velocity and acceleration of the linear motor. The motion profile of the linear motor is based on the following equations [152]:

$$p(t) = p_0 + v_0 \cdot t + \frac{1}{2} \cdot a \cdot t^2 \tag{3.1}$$

$$v(t) = v_0 + a \cdot t \tag{3.2}$$

In which p_0 and v_0 are the initial position in m and velocity in m/s respectively. p_t and v_t the position and velocity at time t and a the acceleration in m/s^2. These equations are rewritten in terms of stroke length and HR. First the HR in beats per minute is converted to heart period (T):

$$T = \frac{60}{HR} \tag{3.3}$$

The linear motor needs to travel the stroke length twice in one heart beat. As the initial velocity is $0m/s$, the acceleration can be expressed as:

$$a = \frac{2 \cdot StrokeLength}{4 \cdot t^2} \tag{3.4}$$

And thus the velocity, following from equation 3.2 is:

$$v = T \cdot a \tag{3.5}$$

3.2.2 Ventricle Contractility

This section outlines the methodology used for predicting ventricle volume and determining ventricle contractility. The description starts by detailing the machine learning techniques and then proceeds to explain the data collection process for training the machine learning model to predict ventricular SV. Followed, the trained model's use to estimate ventricular volume is demonstrated.

3.2.2.1 Build Machine Learning Model

Three machine learning algorithms, including linear regression, GPR, and support vector regression (described in section 2.1.4), were trained using the Regression Toolbox in MATLAB R2021a. The performance of each algorithm was assessed using cross-validation, where the collected experimental data was divided into a training set and a testing set. The training set was used to train the algorithms, and the testing set was used to evaluate their performance. This process was repeated, and the average cross-validation

error was used as the performance indicator. The algorithms were compared based on their Root Mean Square Error (RMSE), R-squared, Mean Squared Error (MSE), and Mean Absolute Error (MAE) values.

3.2.2.2 Data collection and processing

The data used in this study was collected from an experimental setup comprising the left ventricle simulator, a tube, and a vertically positioned reservoir, which was a long, narrow tube. One outlet of the left ventricle simulator was blocked, and at the other outlet, a valve was positioned, followed by a flow meter (PXN-25, Transonic,USA). A pressure sensor (6F, Gaeltec Devices Ltd, UK) was positioned inside the left ventricle, and one pressure sensor was placed at the bottom of the reservoir. The experimental set-up is displayed in figure 3.1.

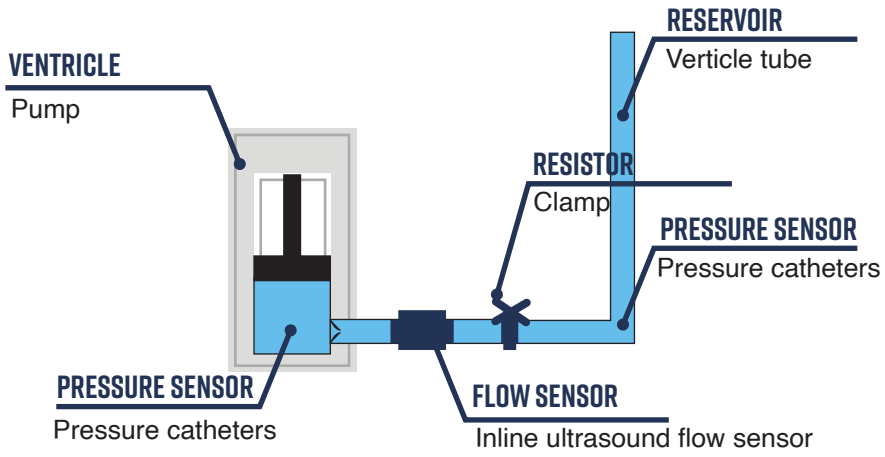

Figure 3.1: Experimental set-up to collect SV data

In the experiment, stroke length of the motor, initial pressure in the reservoir, acceleration of the motor, and resistance at the outlet of the left ventricle were varied. The stroke length, a measure of the distance the motor travels in mm and acceleration, in m/s^2, of the motor are controlled in LabVIEW, the initial pressure is dependent on the amount of water in the reservoir in $mmHg$, and the resistance is considered as a binary variable, either the outlet tube is clamped or not using a hoffman clamp.

The SV was determined via two methods. One method involved integrating the flow curve, and the second method involved measuring the pressure difference in the reservoir before and after the pulse. The SV was then determined by rearranging equation

2.22, the hydrostatic pressure equation. The water inside the system is assumed to be incompressible. A total of 800 data points on SV were gathered, and after post-processing and removing anomalies, 789 were used as training data for the machine learning model.

3.2.2.3 Determination Ventricle Volume and contractility

The machine learning model was trained and a the best performing model was chosen based on their root mean squared error (RMSE), R-squared, mean squared error (MSE) and mean absolute error (MAE). The machine learning model was then used to estimate the ventricle volume by making the assumption that the filling and emptying behaviour of the ventricle followed a second-order polynomial. The resulting approximation of the ventricle volume was then compared to the volume obtained through measurement from the volumetric inflow and outflow of the left ventricle in a MCL. The MCL configuration comprised of the left ventricle simulator, an aortic compliance chamber and a venous reservoir. To modulate ventricle preload, the water quantity within the system was changed, consequently regulating the mean systemic pressure. The mean systemic pressure was regulated from $5mmHg$ to $15mmHg$ in steps of $1mmHg$, keeping stroke length at a value of $21mm$ Moreover, the preload of the ventricle was modified by changing the stroke length of the linear motor. The stroke length was changed from $21mm$ to $30mm$ in steps of $1mm$. This resulted in 21 different experimental settings, each of which was repeated three times. By assessing the impacts of these alterations on the left ventricle simulator using PV-loop analysis, the contractility can be determined via the slope of E_{es}, as explained in section 2.1.1.

3.3 Results

First the results of the HR control of the left ventricle are shown followed by the results of the ventricle contractility.

3.3.1 Heart Rate

After implementation of the motion equation in LabVIEW the following motion profile was observed for one heart beat at 60 beats per minute, as seen in figure 3.2. In this motion

profile the linear motor has a stroke length of $20mm$. The acceleration is constant and the time period of the heart beat equals $1s$ which is equal to a HR of 60 beats per minute.

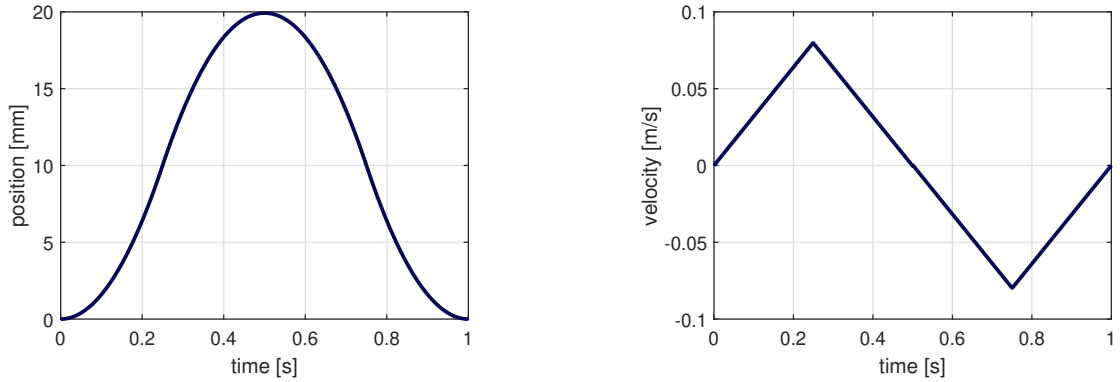

(a) Position time profile

(b) Velocity time profile

Figure 3.2: Motion profile of the linear motor for one heart beat at 60 beats per minute. (a) graph depicts the position time profile and the (b) graph the velocity time profile.

3.3.2 Ventricle Contractility

This section describes the results of the machine learning model, ventricle volume determination and ventricle contractility.

3.3.2.1 Feature selection

The feature selection process for training the machine learning model involved a combination of correlation and forward feature selection techniques. Initially, a correlation heatmap was generated (Figure 3.3) to examine the correlation between the features. Strong correlations were observed between SV and stroke length (0.89), maximum pressure and maximum flow (0.88), maximum pressure and acceleration (0.86), and maximum flow and acceleration (0.78). Weak correlations were observed between SV and initial pressure (0.37) and SV and maximum pressure (0.29), and no correlation was found between SV and acceleration or resistance.

Further visual inspection (figure 3.4) revealed that stroke length had a significant impact on SV, but acceleration did not. Moreover, resistance had little effect on SV where a maximum difference of $4mL$ was observed between resistance and no resistance, which was beyond the measurement's accuracy. As a result, this feature was omitted.

Figure 3.3: Correlation heatmap of the features.

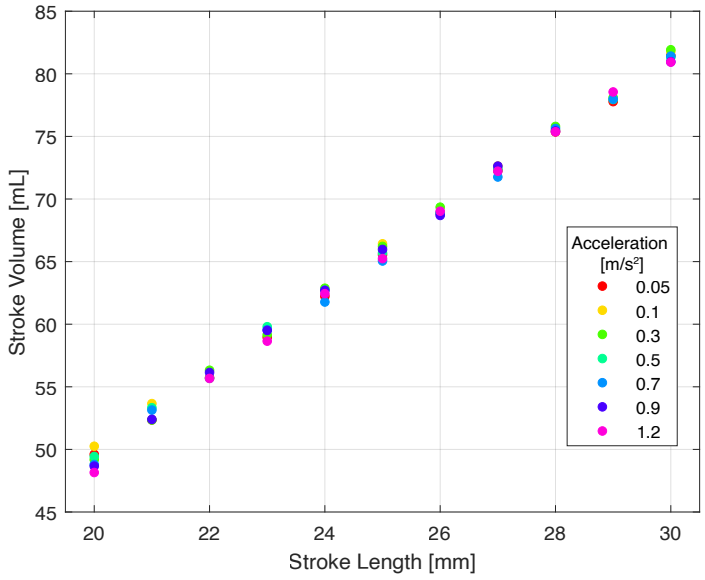

Figure 3.4: Scatter plot of the experimental data showing stroke length on the x-axis, SV on the y-axis and acceleration indiacted with colours.

After observing a strong correlation between maximum pressure, maximum flow, and acceleration and visually examining the effect of acceleration and resistance on SV, it was decided to consider only maximum pressure for forward feature selection. The

linear regression, linear support vector regression, and rational quadratic GPR models were then compared, and the first two features selected were initial pressure and stroke length, as they had the two highest correlation values with SV. The RMSE values for these models and features were 3.5, 3.5, and 3.4, respectively. After adding maximum pressure as a feature, the RMSE was reduced to 3.4, 3.4, and 2.1, respectively. Therefore, the models were trained using the features: initial pressure, stroke length, and maximum pressure.

3.3.2.2 Machine Learning Model Performance

The obtained results from the linear regression model are presented in figure 3.5, which includes both the prediction plot and the residuals plot. The prediction plot displays the true SV on the x-axis and the corresponding predicted SV from the linear regression model on the y-axis. The linear model has a RMSE of 3.44, a R^2 of 0.93, a MSE of 11.83 and MAE of 2.82.

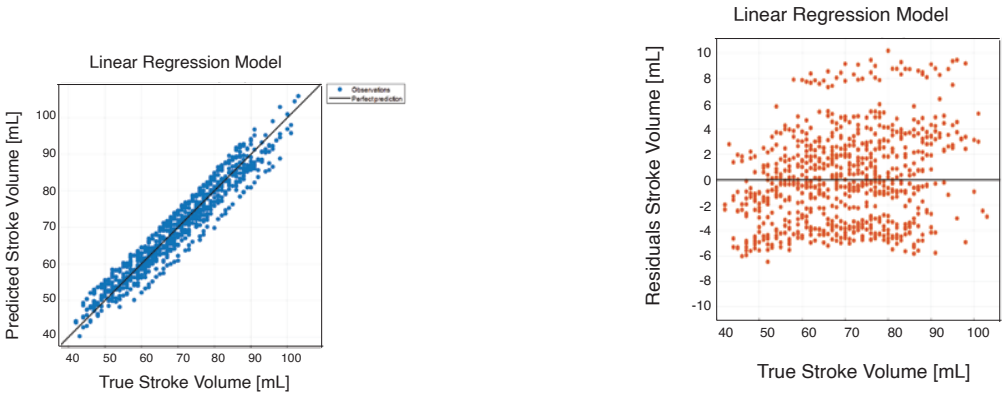

(a) Prediction plot

(b) Residuals plot

Figure 3.5: The results of the linear regression model of the prediction plot (a) and residuals plot (b)

The results from the linear support vector regression model are presented in figure 3.6, which includes both the prediction plot and the residuals plot. The linear support vector regression model has a RMSE of 3.46, a R^2 of 0.93, a MSE of 11.98 and MAE of 2.84.

The results from the rational quadratic GPR model are presented in figure 3.7, which includes both the prediction plot and the residuals plot. The GPR model has a RMSE of

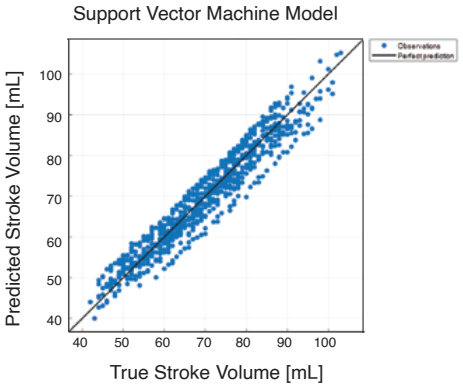

(a) Prediction plot

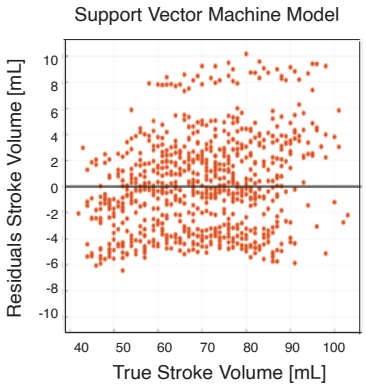

(b) Residuals plot

Figure 3.6: The results of the support vector regression model of the prediction plot (a) and residuals plot (b)

2.06, a R^2 of 0.98, a MSE of 4.23 and MAE of 1.28.

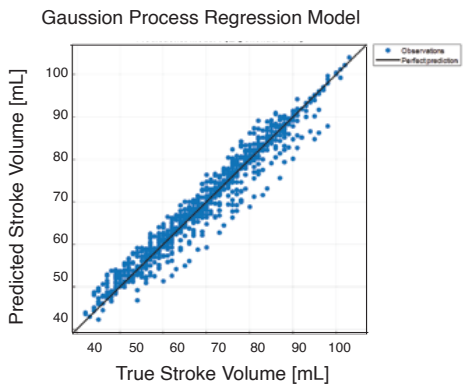

(a) Prediction plot

(b) Residuals plot

Figure 3.7: The results of the GPR model of the prediction plot (a) and residuals plot (b)

All results are combined in a table and shown in table 3.1. Following from the results it can be concluded that the rational quadratic GPR model is the best performing model, as it has the lowest value of RMSE, MSE and MAE.

3.3.2.3 Ventricle Volume Approximation Performance

From geometry analysis it was found that the ventricle volume when full is $200mL$. The end systolic and diastolic time is determined from the position of the linear motor. Then,

Table 3.1: RMSE, R-squared, MSE and MAE of the linear regression, linear support vector regression and Rational Quadratic GPR model.

	Linear Regression	Linear Support Vector Regression	Rational Quadratic GPR
RMSE	3.44	3.46	2.06
R-Squared	0.93	0.93	0.98
MSE	11.83	11.98	4.23
MAE	2.82	2.84	1.28

using the trained GPR model, the ventricle volume was approximated based on the predicted SV in combination with a second order polynomial. The resulting ventricle volume approximation was then compared to the experimental ventricle volume obtained through direct measurement of the in and outflow of the ventricle.

Figure 3.8 visualises the experimental ventricle volume vs a predicted ventricle volume. Displayed is one heart beat with on the x-axis the time and on the y-axis the ventricle volume in mL. At onset of diastole the difference between the predicted and experimental volume was $3mL$.

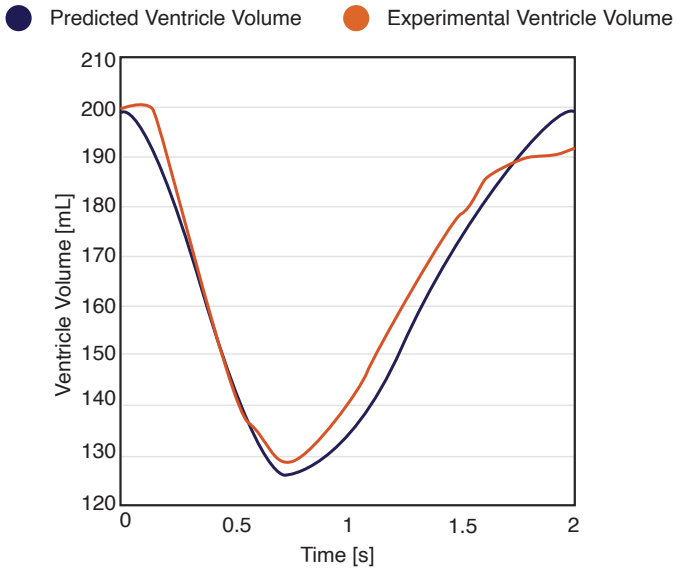

Figure 3.8: Results of ventricle volume prediction compared to the experimental ventricle volume.

The experiment was repeated for different values of initial pressure and stroke length.

The result of each experiment and the difference between the predicted and experimental stroke volume is shown in table 3.2.

Table 3.2: Table results of ventricle volume prediction in which stroke length, reservoir pressure, maximum absolute volume error and percentage volume error are listed. The experiment was conducted in random order to reduce bias.

Stroke Length [mm]	Reservoir Pressure [$mmHg$]	$\Delta Volume_{max}$ [mL]	% V_{max} [%]
20	5	12.4	11.6
20	6	8.6	9.1
20	7	10.3	9.5
20	8	7.3	7.9
20	9	2.4	2.9
20	10	6.2	6.5
20	11	4.4	7.2
20	12	9.0	8.9
20	13	7.0	9.5
20	14	5.8	8.4
20	15	6.9	8.3
21	5	6.8	7.1
22	5	7.7	9.4
23	5	8.7	8.4
24	5	6.4	7.0
25	5	11.9	13.8
26	5	8.1	9.9
27	5	5.8	7.8
28	5	6.2	7.6
29	5	9.7	10.2
30	5	9.4	12.0

3.3.2.4 Ventricle Contractility

Figure 3.9 shows the effect of preload, by changing the total volume in the mock loop (a) and the stroke length (b), the PV-loop of the left ventricle simulator. In both graphs the isovolumetric contraction and relaxation of the ventricle are not present.

In the graph (a) of figure 3.9 the increase of overall volume in the MCL leads to an increase in P_{es} and SV. For the experiment of a mean systemic pressure of $5mmHg$ the P_{es} and SV equalled $130mmHg$ and $52mL$, respectively. When the mean systemic pressure was raised to $15mmHg$ the P_{es} and SV increased to $200mmHg$ and $62mL$, respectively. ESV decreased from $148mL$ to $138mL$, there was no change in EDV. The overall shape of the PV-loop shifted towards the left, distinct from the native heart, leading to the inability

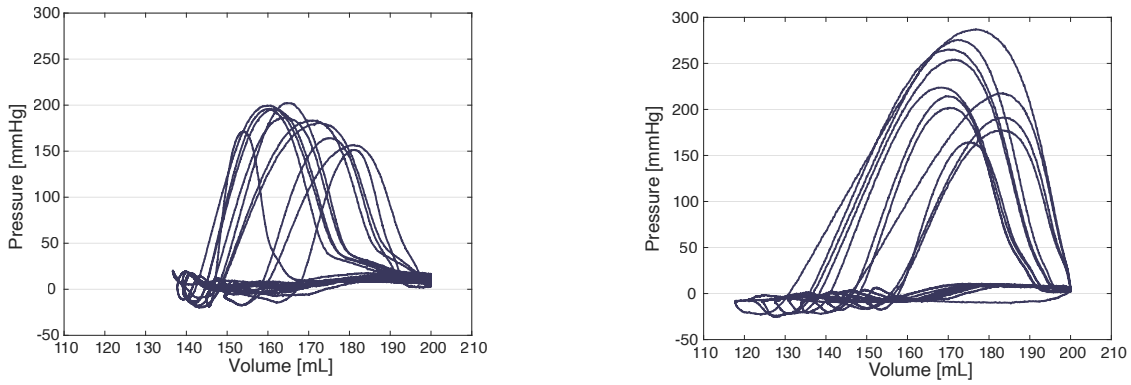

(a) Change in volume

(b) Change in stroke length

Figure 3.9: PV-loops as a result of changing the total volume in the mock loop (a) and the stroke length (b) on the PV-loop.

to ascertain contractility from this experiment.

Similarly, for graph (b) of figure 3.9, the increase of stroke length leads to an increase in P_{es} and SV. For a stroke length of $30mm$ the P_{es} and SV increased to $290mmHg$ and $81mL$ respectively. The ESV decreased to $119mL$, there was no change in EDV. The overall shape of the PV-loop increased size, both in height and width, distinct from the native heart, leading to the inability to ascertain contractility from this experiment.

3.4 Discussion

The primary objectives of this study were the control of HR and ventricular contractility. Additionally, as the assessment of ventricular contractility necessitates the measurement of ventricle volume, the evaluation of ventricle volume also stood as an aim within this study. HR was successfully controlled by using the linear motor's displacement and velocity, similar to the control strategies of prior MCL that used piston pumps as a driving force [121], [137].

To asses ventricle volume, a machine learning model was made to predict SV from which ventricle volume was derived. The results obtained from this study indicate that machine learning techniques can effectively predict SV. Among the models tested, the GPR model demonstrated the highest performance in SV prediction, and the subsequent approximation of ventricle volume showed good agreement with the experimental measurements. The largest difference between the experimental and predicted ventricle volume was observed in the case of a stroke length of $25mm$, and reservoir pressure of

$5mmHg$, with a maximum difference of $11.9mL$ or 13.8%. It should be noted that the experimental volume measurement used two flow probes, each of which carried a relative error of 10%. Taking into account this experimental error, the experimental and predicted ventricle volume can be considered nearly equal.

This approach of measuring ventricle volume holds potential even in situations where flow sensors are not available, as the data collection for the machine learning model does not necessarily require the use of a flow probe. Instead, SV can be determined from the hydrostatic pressure change. This aspect becomes particularly beneficial when constructing a mock loop with limited funding. However, a disadvantage can be that the machine learning model needs to be retrained when anything about the left ventricle changes.

Another advantage of the machine learning model is speed. Compared to mathematical modelling, which demands higher computational resources, and imaging techniques, which involve specialised equipment and additional computational power, the machine learning model offers an efficient alternative. Previous studies on ventricle volume prediction [153] have also highlighted the ability of machine learning models to rapidly predict left ventricle mechanics compared to finite element simulations. However, no prior research has explored this approach within the context of an MCL setting.

To further enhance the accuracy of predictions, this approach can be refined by incorporating additional features, such as ventricle shape. Moreover, the method holds promise for predicting ventricle volume, potentially leading to a quicker and less invasive approach for assessing ventricular function in patients. This would eliminate the reliance on imaging techniques for ventricle volume assessment [154].

Using the ventricle volume prediction the effect of preload on the ventricle was investigated to quantify the contractility. However, during this experimentation, differences between the behaviour of the left ventricle simulator and the native heart in terms of contractility was found. Observing the two ventricle volume loops in figure 3.9, it is evident that the isovolumic contraction and relaxation phases are absent. This observation suggests that the aortic and mitral valves of the left ventricle simulator are not effectively maintaining pressure. This can also be deduced from the ventricle volume curves. At the onset of systole, water immediately exits the ventricle into the aorta; conversely, in the CVS, the aortic valve holds the blood to increase the ventricular pressure. A similar sce-

nario applies to the mitral valve, which should prevent blood from entering the ventricle during the isovolumic relaxation phase. This phase is not detected in the left ventricle simulator. Furthermore, in the native heart the P_{es} is depended on the EDV. However, due to the rigid nature of the chamber in this left ventricle simulator, EDV remains constant. Nevertheless, for both the increase in stroke length and systemic pressure resulted in an increase in P_{es} and SV. Yet, the rigid ventricle walls cause a shift of the PV-loop upwards and to the left, making it impossible to quantify contractility for this ventricle.

Other researchers used pressure regulated left ventricle simulators to overcome this issue. Such as Baloa et al. who's camber pressure of the piston pump was continuously regulated to provide the correct value of elastance [63]. Similarly, HR and contractility parameters were used as input to a mathematical model to determine the systemic resistance and mean systemic pressure in the hydraulic system [73]. Left ventricle simulators that made use of air pressure regulators to contract the ventricle were able to regulate contractility by changing the level of pneumatic air pressure to vary end-diastolic volume [69], [76], [155]. However, none of these methods are feasible with the use of the left ventricle simulator used in this study as the control of this linear motor relies on the position, velocity and acceleration and no real-time control system of the linear motor is in place to control the motion using ventricular pressure as input.

3.5 Conclusion

In conclusion, this study primarily focused on regulating HR, ventricular contractility, and evaluating ventricle volume. The HR control was successfully implemented via the linear motor, as evidenced by the motion profile of the linear motor for a HR at 60 beats per minute, using LabVIEW, demonstrates a stroke length of 20mm, constant acceleration, and a time period of 1s.

To asses ventricle volume, a machine learning model was developed to predict SV, which in turn was used to determine ventricle volume. Among the models tested, the rational quadratic GPR model emerged as the most accurate, showing an RMSE of 2.06, a R^2 value of 0.98, and producing ventricle volume predictions with a maximum difference of $3mL$ from experimental measurements.

However, when analyzing ventricular contractility, distinct differences between the

left ventricle simulator and the native heart were evident. Adjustments in the total volume and stroke length in the MCL influence the P_{es} and SV. Notably, an increase in mean systemic pressure from $5mmHg$ to $15mmHg$ results a rise in P_{es} and SV to $200mmHg$ and $62mL$, respectively. Furthermore, increasing stroke length to $30mm$ increases the P_{es} and SV to $290mmHg$ and $81mL$, respectively. Moreover, the PV-loop results indicated an absence of isovolumic contraction and relaxation phases, which suggests inadequate pressure buildup by the aortic and mitral valves. Coupled with the chamber's rigidity, these observations complicate the quantification of contractility for this simulator. While other researchers have utilised pressure-regulated ventricle simulators to circumvent similar challenges, the specialised control mechanism of our study's linear motor precluded such adaptations.

Future endeavors should develop a real-time control system that integrates ventricular pressure input, which would facilitate a more precise regulation of the ventricle's contractility.

Chapter 4

Control of the Resistance: the Automated Vascular Resistor

4.1 Introduction

The vessel's radius is one of the factors opposing resistance to blood flow in the CVS. Arteries and veins, to a degree, can regulate inner radius by contraction or dilation of the smooth muscle varying SVR between 11 and 18 $mmHg \cdot min \cdot mL^{-1}$ [156]. [1]

The SVR is one the control targets of the baroreflex response. The SVR in the CVS is developed by the vascular bed in the smaller diameter arterioles and capillaries. These vessels can circumstantially constrict (leading to an increase in resistance) or dilate (vice versa) the smooth muscle wall to mediate a change in resistance, figure 4.1. The vessel's radius (r) is the main contributor of SVR (equation 4.1), other factors include blood viscosity (η), vessel length (L), branches, tapering, vasomotion and series-parallel arrangement of the vessels.

$$R \propto \frac{\eta L}{r^4} \tag{4.1}$$

There are several methods employed to impose resistance in MCLs. The use of screw clamps or pinch valves to occlude flexible tubes is a common and cost-effective approach to altering arterial resistance [35], [40], [45], [61], [88], [93], [96], [158]. The screw clamps

[1] Part of this chapter is presented at the European society of artificial organs in F. Cappon, A.W. Khir, P.-L. Hsu, X.Du. "H40- Development and experimental characterisation of an automated clamp-on resistor for mock circulatory loops.," The International Journal of Artificial Organs, vol. 44, no. 9, pp. 604,2021 [157]

Figure 4.1: Illustration of vasoconstriction and dilation of arterioles.

can be placed anywhere in the mock circulatory system, however, do not uniformly occlude the tube, and thus make it difficult to determine the resistance values with analytical methods. Moreover, manual adjustments are required with screw clamps, making them unsuitable for MCLs requiring automated adjustments of resistance. Pinch valves, on the other hand, can be operated electronically, making them a more viable option.

Another method to impose resistance in MCLs is by implementing porous blocks [13], [30], [36]. The resistance value is determined by the length and diameter of the conduits. The resistance of these apparatuses is variable with a slide assembly that partially obstructs some of the conduits. The porous blocks need to be installed in-line with the tubing of the MCL.

Throttle valves, or a variation of them, are also widely used as in-line flow resistors in MCL [28], [33], [38], [63], [98], [121]. In these designs the resistance value can be calculated from the orifice size. Taylor et al. developed an automated design in which the orifice size could be controlled via the position of the piston [141]. However, a downside of this in-line resistor is that it has a fixed position in the MCL.

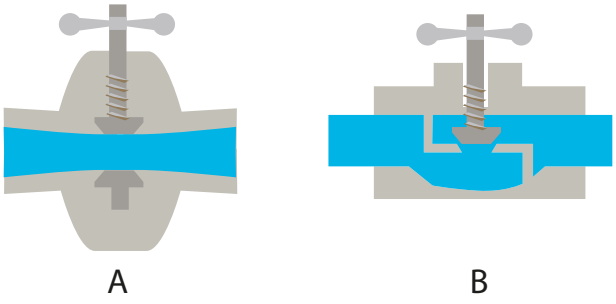

Figure 4.2: 2D images of a (A) pinch valve and (B) throttle valve.

Regardless of the design choice, an important step before using a resistor in any experimental set-up is the characterization to ensure reliable and consistent results. Knowing the resistance values and pressure drop for certain rate of occlusion, is crucial for

ensuring that the results obtained from experiments are reliable. Moreover, it essential to identify the step response of the control system of the resistor before it can be implemented in the hybrid MCL. Therefore, this chapter presents characterization of a clamp-on resistor of which the design was presented in section 2.2.2. The methodology, results, discussion, and conclusion of the characterization are described in detail.

4.2 Methodology

The resistor is characterised in both pulsatile and continuous flow conditions. A rotary positive-displacement pump (DC50G, ZKSJ, China) was used to generate flow for the continuous flow set-up, this pump was replaced by the left ventricle simulator for the pulsatile experiment. Furthermore, the set-up includes a water reservoir ($V = 3142mL$), a flow sensor (PXN25, Transonic, The Netherlands) and two pressure sensors (Gaeltech, UK) positioned directly up and downstream the resistor, figure 4.3. Measurements were taken for flexible tubes, connecting the pump to the water reservoir.

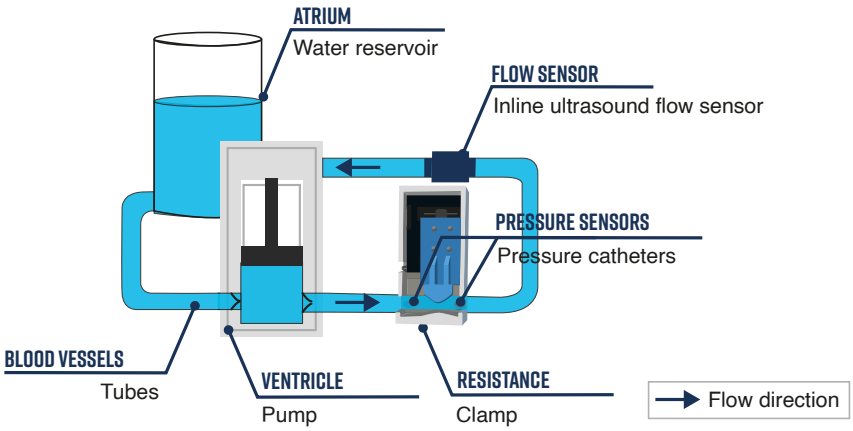

Figure 4.3: Experimental set-up for the characterization of the resistor.

Two experiments were conducted the characterisation experiment and the step response experiment.

4.2.1 Characterisation experiment

The objective of the characterisation experiment is to study the behaviour of the resistor in both continuous and pulsatile flow conditions. Specifically, the experiment measured

pressure and flow under different flow conditions and to use this data to calculate the resistance.

The continuous flow experiment, involved the manipulation of the flow rate through variations in the input voltage of the rotary pump. To establish a understanding of the behaviour of the resistor of a range of flow conditions, five distinct levels were evaluated. Five different flow conditions provide enough variation to capture the range of scenarios within the physiological flow range. For the pulsatile flow condition, a frequency of 60 beats per minute and a stroke length of $10mm$ were used, which produces a heart beat within the physiological pressure range.

For each flow rate, a series of steps were taken to modify the internal diameter of the tubes. Specifically, the resistor was occluded through successive decreases in the diameter of the tubes in increments of $0.5mm$, followed by a corresponding reopening of the tubes in equivalent increments. Throughout the occlusion and reopening procedures, the supply voltage and input pressure of the rotary pumps were held constant.

More specifically,

$$D_i = D_{max} + d_i \tag{4.2}$$

In which

$$d_i = \begin{cases} -0.5mm, & \text{if occlusion} \\ +0.5mm, & \text{if reopening} \end{cases} \tag{4.3}$$

and D_i is the diameter of the tube at the ith step, D_{max} is the maximum diameter of the tube, d is the step size, and i ranges from 1 to the total number of steps needed to reach D_{min}. D_{min} is the minimum diameter at which a reduction in flow is detected.

By occluding and reopening the tubes in successive increments, the impact of different levels of occlusion on the resistance is studied.

The experimental design is outlined in table 4.1. The experiment was conducted with three different tube sizes, with an internal diameter of 8 mm, 5 mm, and 4 mm, and the occlusion and reopening procedures were repeated for each tube. Tube one (internal diameter = $8mm$) and tube three (internal diameter = $4mm$) were more elastic than tube two (internal diameter = $5mm$).

The calculation of the resistance in the continuous flow study made use of equation 2.2, whereby the mean values of pressure and flow were determined through the aver-

Table 4.1: Experimental design conditions for each experiment for the characterisation of the automated vascular resistor experiment.

Experiment Number	Flow Condition	Flow Magnitude
1	Continous	Low
2	Continous	Low
3	Continous	Medium
4	Continous	Medium
5	Continou	Medium
6	Pulsatile	Physiological

aging of signals acquired over a duration of 10 seconds. In the context of pulsatile flow, the resistance was calculated with equation 2.5 obtained from one individual beat.

4.2.2 Step response experiment

The objective of this experiment is to determine the step response of the control system of the resistor. Specifically, to determine the rise time. The rise response is determined for both pulsatile and continuous flow experiments. The rise response will provide an indication of how quickly the system can adjust the resistance, which is an output parameter of the baroreflex response. Only one tube is used for this experiment, and pressure and flow are continuously monitored as previously mentioned. The control systems for continuous and pulsatile flow, as described in section 2.2.2.2, are used.

Specifically, the time-response in resistance was evaluated for steps from 10 to 15, 10 to 20, 10 to 25, 15 to 20, 10 to 25, and 15 to 25 $mmHgmin/L$, for one continuous flow condition. In addition, a step-response from 10 to 20 $mmHgmin/L$ was evaluated for the pulsatile flow condition. The resistance was allowed to have an error of 12% due to uncertainty in the resistance calculation. The rise time was determined as the time required for the resistor to rise from the baseline value to 100% of its final value.

4.2.3 Data analysis

The collected data, acquired from the LabVIEW software (National Instruments, version 2021), was saved in a text file for further analysis. A custom MATLAB script (MathWorks, version R2021a) was developed to extract the pressure and flow waveforms from the recorded data. The continuous flow values were calculated by taking the mean of the data recorded during a single experiment lasting 60 seconds. To filter the waveforms in

Table 4.2: Experimental design for the time response of the automated vascular resistor experiment.

Experiment	Step response [$mmHgL/min$]	Time response
Continous	10 to 15	in seconds
Continous	10 to 20	in seconds
Continous	10 to 25	in seconds
Continous	15 to 20	in seconds
Continou	10 to 25	in seconds
Continous	15 to 25	in seconds
Pulsatile	10 to 20	in number of heartbeats

the pulsatile experiment, a second-order polynomial Savitzky-Golay filter with a frame length of 31 was applied. This filter was specifically chosen due to its ability to preserve the area, position, and width of peaks in the pressure waveforms.

4.3 Results

This section provides a details of the outcomes obtained from both the characterisation and time response experiments, which aimed to investigate the behaviour of the automated vascular resistor under both continuous and pulsatile flow conditions.

4.3.1 Characterisation experiment

The flow, pressure and resistance results of tube one (internal diameter = $8.0mm$, wall thickness = $1.5mm$) are shown in figure 4.4. The findings reveal a inversely proportional relationship ($y = a \cdot x^b$) between the resistance and internal diameter. The statistical analysis indicated that this relationship is substantial with an R^2 value of 0.99, 0.99, 0.99, 0.97, 0.88 and 0.70 for a flow rate of $4.7L/min$, $3.4L/min$, $2.8L/min$, $2.1L/min$, $1.2L/min$ and pulsatile flow. With an RMSE value of 0.57, 0.45, 0.45, 0.64, 0.90 and 4.8.

Fitting an extra term in the relationship ($y = a \cdot x^b + c$) improves the fit between the resistance and internal diameter with an R^2 value of 0.99, 0.99, 0.99, 0.99, 0.99 and 0.99 for a flow rate of $4.7L/min$, $3.4L/min$, $2.8L/min$, $2.1L/min$, $1.2L/min$ and pulsatile flow. With an RMSE value of 0.47, 0.35, 0.35, 0.30, 0.30 and 0.76.

The resistance values for each flow condition were rescaled (min-max normalization), and it was observed that although the flow rate varied, the resistance curve followed the

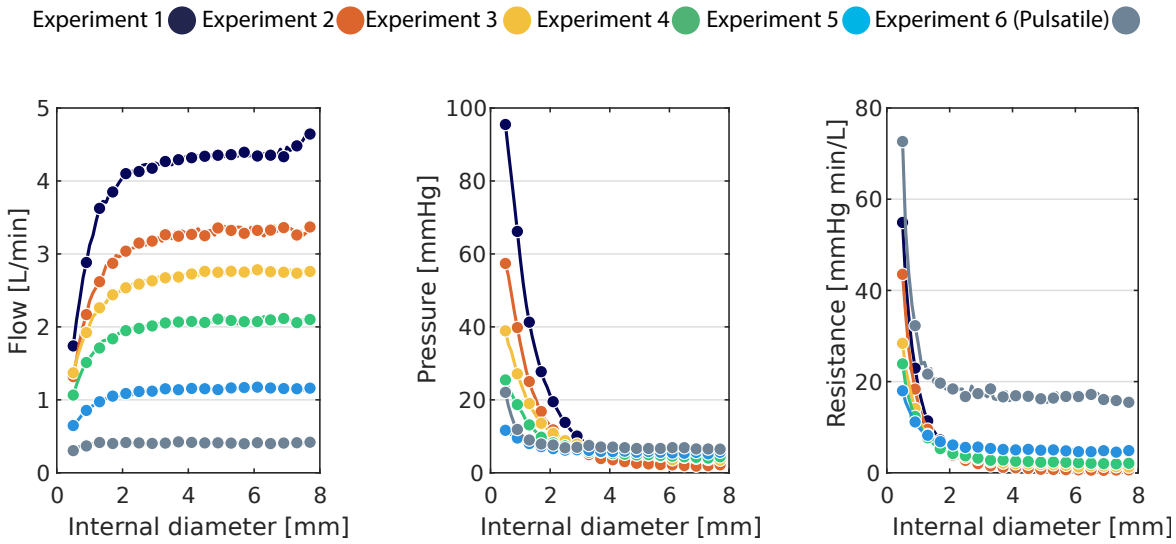

(a) Flow (b) Pressure (c) Resistance

Figure 4.4: Results resistance tube one, internal diameter = 8.0 mm, wall thickness = 1.5 mm.

same inversely proportional trend when plotted over internal diameter, figure 4.5.

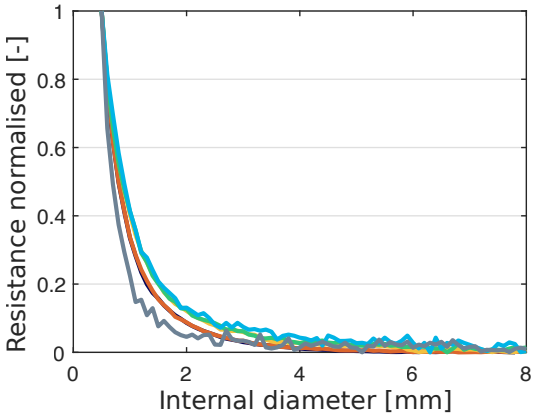

Figure 4.5: Normalised diameter tube one, internal diameter = 8.0 mm, wall thickness = 1.5 mm.

The flow, pressure and resistance results of tube two (internal diameter = $5.0mm$, wall thickness = $1.0mm$) are shown in figure 4.6. The findings reveal a inversely proportional relationship ($y = a \cdot x^b$) between the resistance and internal diameter. The statistical analysis indicated that this relationship is substantial with an R^2 value of 0.98, 0.97, 0.95, 0.92, 0.88 and 0.83 for a flow rate of $2.0L/min$, $1.4L/min$, $1.2L/min$, $0.9L/min$, $0.6L/min$ and pulsatile flow. With an RMSE value of 1.8, 1.7, 2.0, 2.2, 3.2 and 4.0.

Fitting an extra term in the relationship ($y = a \cdot x^b + c$) improves the fit between the

resistance and internal diameter with an R^2 value of 0.99, 0.99, 0.99, 0.99, 0.99 and 0.98 for a flow rate of $2.0L/min$, $1.4L/min$, $1.2L/min$, $0.9L/min$, $0.6L/min$ and pulsatile flow. With an RMSE value of 0.46, 0.77, 0.39, 0.52, 0.63 and 1.2, respectively.

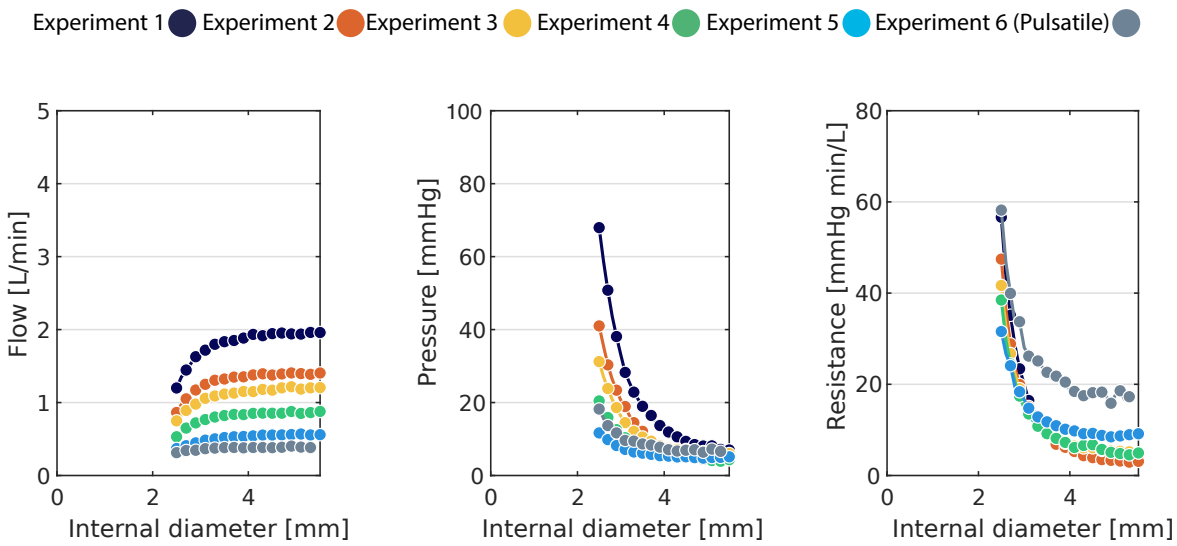

(a) Flow (b) Pressure (c) Resistance

Figure 4.6: Results resistance tube two, internal diameter = 5.0 mm, wall thickness = 1.0 mm.

Similarly to tube one, the resistance values for each flow condition for tube two were rescaled (min-max normalization), and it was observed that although the flow rate varied, the resistance curve followed the same inversely proportional trend when plotted over internal diameter, figure 4.7.

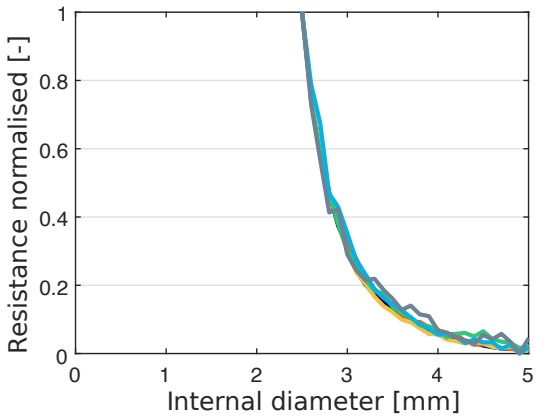

Figure 4.7: Normalised diameter tube one, internal diameter = 5.0 mm, wall thickness = 1.0 mm.

The flow, pressure and resistance results of tube three (internal diameter = $4.0mm$,

wall thickness = $0.5mm$) are shown in figure 4.8.The findings reveal a inversely proportional relationship ($y = a{\cdot}x^b$) between the resistance and internal diameter. The statistical analysis indicated that this relationship is substantial with an R^2 value of 0.98, 0.94, 0.99, 0.92, 0.81 and 0.86 for a flow rate of $1.9L/min$, $1.4L/min$, $1.2L/min$, $0.9L/min$, $0.5L/min$ and pulsatile flow. With an RMSE value of 2.0, 2.3, 0.45, 2.1, 2.2 and 3.3.

Fitting an extra term in the relationship ($y = a \cdot x^b + c$) improves the fit between the resistance and internal diameter with an R^2 value of 0.99, 0.99, 0.99, 0.99, 0.99 and 0.98 for a flow rate of $4.7L/min$, $3.4L/min$, $2.8L/min$, $2.1L/min$, $1.2L/min$ and pulsatile flow. With an RMSE value of 0.56, 0.60, 0.35, 0.32, 0.54 and 1.2, respectively.

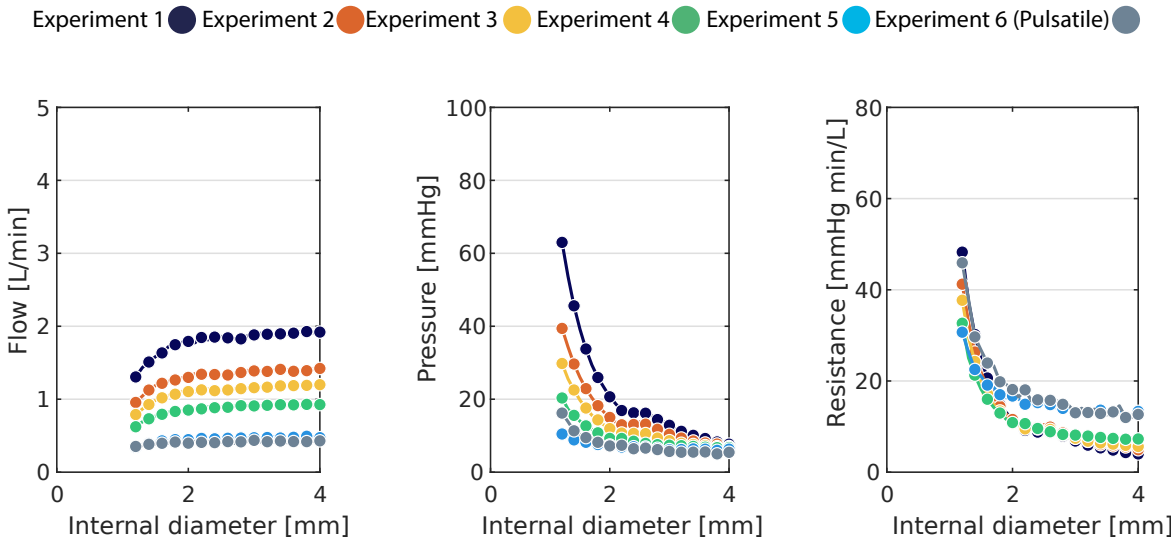

(a) Flow (b) Pressure (c) Resistance

Figure 4.8: Results resistance tube two, internal diameter = 4.0 mm, wall thickness = 0.5 mm.

Similarly to the previous two tubes, the resistance values for each flow condition for tube three were rescaled (min-max normalization), and it was observed that although the flow rate varied, the resistance curve followed the same inversely proportional trend when plotted over internal diameter, figure 4.9.

4.3.2 Step response experiment

The results are shown in in figure 4.10 illustrating five different step responses of the hydraulic resistor for continuous flow. The rise time of each step response was determined by visual inspection. The step response from 15 to $25mmHgL/min$ had a rise time of 0.6

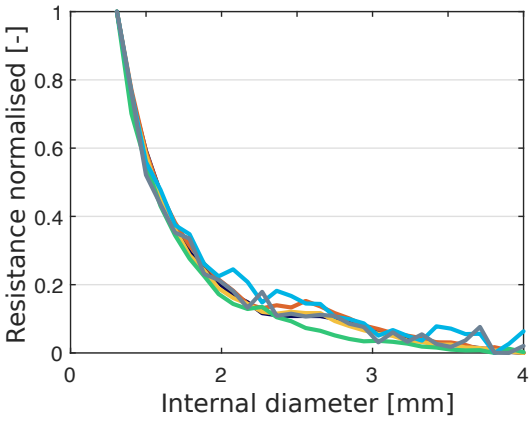

Figure 4.9: Normalised diameter tube one, internal diameter = 4.0 mm, wall thickness = 0.5 mm.

seconds, while the step response from 15 to $20mmHgL/min$ had a slightly shorter rise time of 0.5 seconds. The step response from 10 to $25mmHgL/min$ had a longer rise time of 1.4 seconds, and the step response from 10 to $20mmHgL/min$ had a further extended rise time of 2.1 seconds. The step response from 10 to $15mmHgL/min$ had the longest rise time of 2.9 seconds.

The process of controlling resistance under continuous flow conditions is relatively straightforward, as the resistance can be continuously calculated based on the pressure difference over flow. However, for pulsatile conditions, the mean pressure and flow for each heartbeat must be determined. Figure 4.11 displays the pressure and flow signals for the pulsatile flow conditions during the step response. As shown in the figure, the upstream pressure varies between $120mmHg$ and $-25mmHg$, while the downstream pressure varies between $10mmHg$ and $0mmHg$, and the flow between $-3L/min$ and $8L/min$.

In order to analyse pulsatile flow conditions, mean values of the upstream and downstream pressure and flow must be calculated for each heartbeat. These mean values are shown in figure 4.12. Specifically, the mean values of upstream pressure fall within the range of $18 - 35mmHg$, while the mean values of downstream pressure range between $10 - 13mmHg$. Additionally, the mean flow values varies between $0.4 - 1.6L/min$.

The calculated mean values of pressure and flow are used to determine the resistance for each heartbeat. LabVIEW uses these values to adjust the position of the resistor, in this case as step response from $10mmHgmin/L$ to $20mmHgmin/L$. The positional changes of the linear motor, as well as the resulting step response, are illustrated in figure 4.13. From the graph we can see that under pulsatile flow conditions, the step

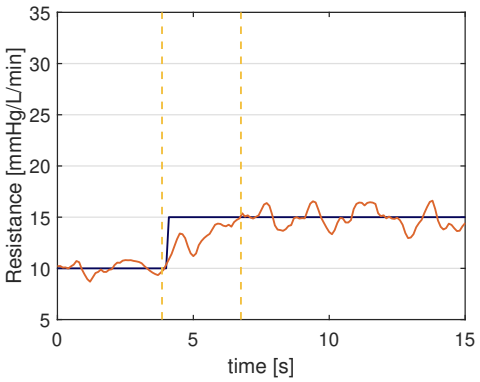

(a) From 10 to 15 $mmHgmin/L$

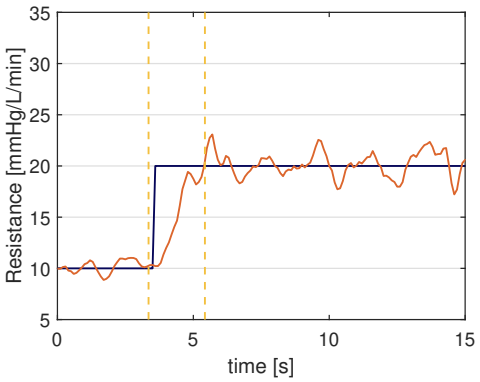

(b) From 10 to 20 $mmHgmin/L$

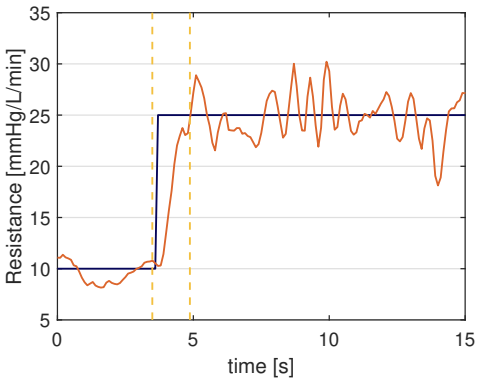

(c) From 10 to 25 $mmHgmin/L$

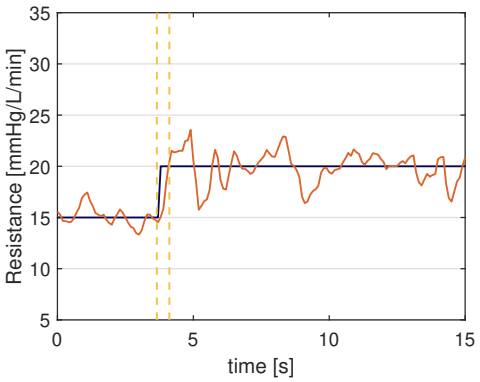

(d) From 15 to 20 $mmHgmin/L$

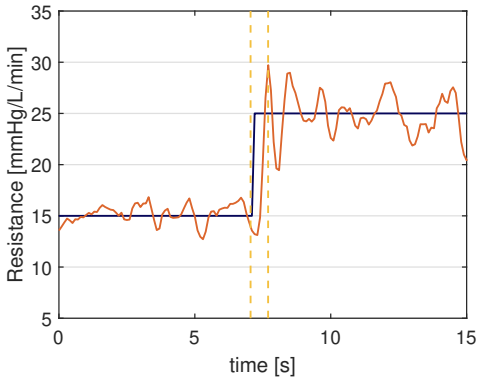

(e) From 15 to 25 $mmHgmin/L$

Figure 4.10: Results of the continuous flow step response experiment. Rise time for the experiments are (a) 2.9 seconds, (b) 2.1 seconds, (c) 1.4 seconds, (d) 0.5 seconds and (e) 0.6 seconds.

response from 10 to $20 mmHgL/min$ was equivalent to three heartbeats.

	Linear Regression	Linear Support Vector Regression	Rational Quadratic GPR
RMSE	3.44	3.46	2.06
R-Squared	0.93	0.93	0.98
MSE	11.83	11.98	4.23
MAE	2.82	2.84	1.28

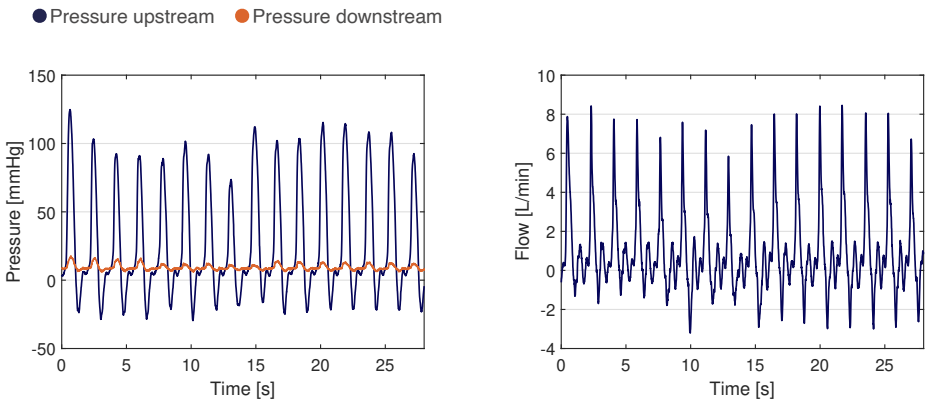

(a) Pressure (b) Flow

Figure 4.11: The pressure curve (a) and the flow curve (b), obtained during the pulsatile flow step response experiment.

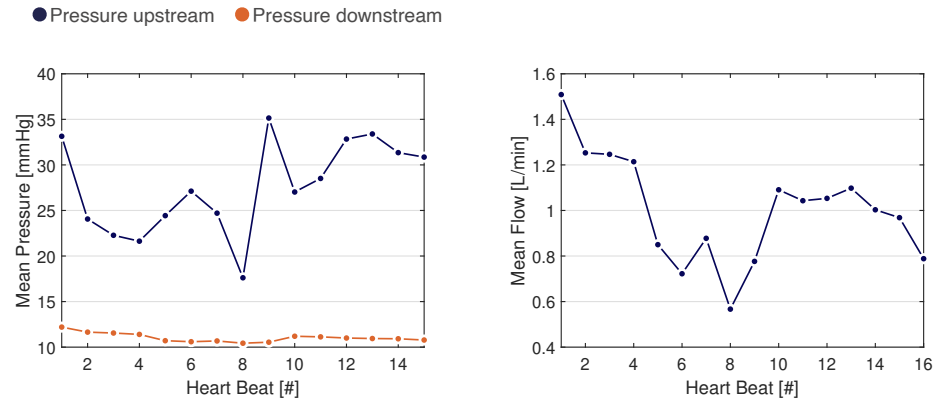

(a) Mean Pressure (b) Mean Flow

Figure 4.12: The variation in mean pressure (a) and mean flow (b), plotted as a function of the number of heartbeats during the pulsatile flow step response experiment.

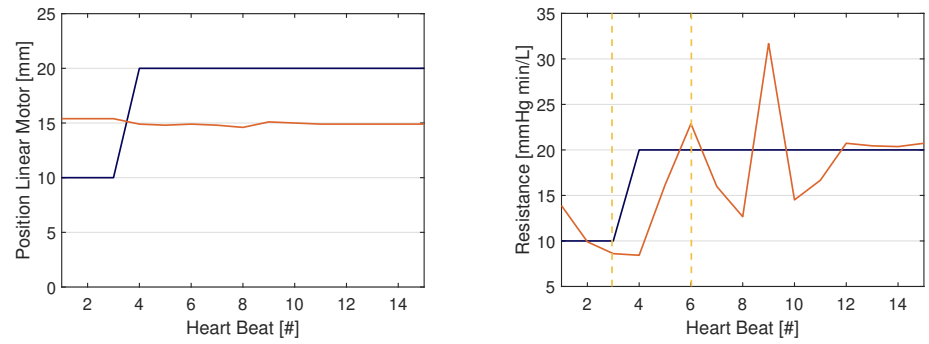

(a) Position Linear Motor (b) Resistance

Figure 4.13: The pulsatile step response, where the left panel depicts the position of the resistor, and the right panel demonstrates the resistance. It is noteworthy that the resistor would be entirely closed when placed in position 0.

4.4 Discussion

This study characterised a clamp-on resistor that has been developed for the use in a hybrid MCL setup. The resistance value of the resistor depends on the radius of the vessel. The resistance can be either increased or reduced by obstructing the tube. The resistor is designed to modify the resistance in the MCL by occluding the flexible tubes through a clamp-on mechanism. The aim of the study was to evaluate the capability of the resistor to change the resistance to flow and to evaluate the step response of the control system.

4.4.1 Characterisation experiment

Analysis of the normalisation graphs obtained from the characterisation experiment indicates that the resistance value remains relatively stable, with less than a 5% variation in the internal diameter range of $8-4mm$, $5-5.5mm$, and $4-3mm$ for tube 1, 2, and 3, respectively. This slight deviation could be attributed to the non-uniform deformation of the tube when subjected to external force by the pusher, with radial deformation assumed in the analysis. Despite the changing shape of the tube in this range, the orifice area remains constant, leading to negligible changes in resistance.

Moreover, the graphs showing the relationship between resistance and internal diameter show a notable rise in resistance beyond $2mm$, $4mm$, and $3mm$ internal diameters for tube 1, 2, and 3, respectively. The observed dissimilarity in the resistance and internal diameter among the three tubes can be attributed to variations in tube flexibility and flow characteristics.

Nevertheless, the characterisation experiment shows that the resistor is able to change the arterial resistance in the physiological range of $9-20.0mmHgmin/L$ [156] and thus feasible for using in a MCL to simulate the physiological arterial resistance.

Due to the observed variation in the resistance compared to internal diameter among the tubes, it is necessary to continuously measure pressure and flow when using the automated clamp-on resistor in an MCL. Unlike other resistors described in literature, whose resistance can be characterised using orifice area and do not deform over time [141], the proposed clamp-on design suffers from this disadvantage. Although, the characterisation experiment demonstrated that the automated resistor and control system

presented in this study can be used for tubes of varying sizes and flexibility without the need for parameter optimisation prior to any experiment, this has not been tested and confirmed. As the controller is designed to be working in this set-up only, it is unclear how well it would transfer to other experimental set-ups. Moreover, the physical design of the controller limits the dimensions of the tube up to $2.5cm$.

Anatomical models of the arterial system are often used to study wave propagation and pressure distribution [77]. In this context, the flexibility and versatility of the proposed resistor could be considered advantageous. The ability to accommodate tubes of different flexibility and sizes without requiring parameter optimisation may facilitate the study of nervous system responses in models of the arterial system.

4.4.2 Step response experiment

From the step response experiment it can be concluded that the rise time of the hydraulic resistor depends on the magnitude of the step change in input. The larger the step change in input, the longer the rise time of the system output.

Specifically, the step response from 15 to $25mmHgL/min$ had a rise time of 0.6 seconds, which is relatively short. The step response from 15 to $20mmHgL/min$ had a slightly shorter rise time of 0.5 seconds. The longer rise times were observed for the step responses with larger step changes in input, such as the step response from 10 to $25mmHgL/min$ with a rise time of 1.4 seconds and the step response from 10 to $20mmHgL/min$ with a rise time of 2.1 seconds.

The step response graphs shows an observable degree of noise in the resistance signal. The origin of this noise can primarily be attributed to the continuous flow pump, which generates an imperfect continuous flow. This imperfect flow is visible in the noise in the resistance signal.

In the context of pulsatile flow conditions, the automated resistor is able to respond to an increase in resistance from $11 - 18mmHgL/min$ within three cardiac cycles. While the response time of the control system could potentially be improved, it is currently deemed sufficient within the context of this thesis and the implementation of the baroreflex responses. The refinement of the time response of the automated resistor can be addressed in future research.

4.5 Conclusion

In conclusion, this study evaluated the feasibility of using the designed automated clamp-on resistor in a MCL setup for modifying the resistance. The experimental investigation presented insights into the behaviour of the automated vascular resistor under both continuous and pulsatile flow conditions. The characterisation experiment demonstrated that the resistor could change the resistance in the physiological range and accommodate tubes of different sizes and flexibility. Upon normalisation, it was clear that irrespective of the flow rate, the resistance trend remains inversely proportional to the internal diameter. However, the experiment also revealed the necessity of continuously measuring pressure and flow, when specific values of arterial resistance are required, due to the non-uniform deformation of the tube when subjected to external force by the pusher.

The step response experiment revealed that the rise time of the hydraulic resistor depends on the magnitude of the step change in input, with larger step changes resulting in longer rise times. Under continuous flow conditions, the rise time of the hydraulic resistor step response displayed variability based on initial and final conditions. In contrast, pulsatile conditions introduced more intricate dynamics. The automated resistor demonstrated sufficient response time for implementing baroreflex responses in the context of pulsatile continuous and flow conditions.

Chapter 5

A Hybrid Mock Circulatory Loop: The Baroreflex Response

5.1 Introduction

The maintenance of homeostasis in the body is an important function of the CVS.[1] One of the key mechanisms involved in this process is the baroreflex, a regulatory mechanism that modulates blood pressure through changes in HR, peripheral resistance, and cardiac contractility (described in detail in section 1.1.0.3). Stretch receptors, located in the walls of the carotid sinus and aortic arch, serve as the primary detectors of changes in blood pressure, which are then transmitted as signals to the central nervous system. The autonomic nervous system integrates these signals and adjusts regulatory mechanisms accordingly to restore blood pressure to its set point. The baroreflex is thus an essential component of cardiovascular function. Understanding the interaction between the baroreflex and CADs is critical for developing effective CADs to support patients with heart failure.

The aim of this study is investigate the response of the implemented baroreflex in a hybrid MCL to different stimuli. The methodology, results, discussion, and conclusion of the evaluation are described in detail.

[1] Part of this chapter is presented at the European society of artificial organs in F. Cappon, X.Du, P.-L. Hsu, A.W. Khir. "P23 - Development and Validation of a Mock Circulatory Loop with Baroreflex Response," The International Journal of Artificial Organs, vol. 46, no. 9, pp. 440-441,2023 [159]

5.2 Methodology

In this section, the methodology used to investigate the modulation of parameters by the baroreflex response to a specific pressure stimulus is described. Specifically, the initial experiment studies the baroreflex behaviour in the numerical environment, prior to the hybrid environment.

5.2.1 Evaluation of the baroreflex response in a numerical model

This experiment is designed to assess the behaviour of the baroreflex in the numerical environment. Ursino's model [119], a well-established lumped-parameter model of the cardiovascular system, was used to simulate the baroreflex response. A Simulink model was developed based on the model equations and parameters provided in the literature [119]. Further details regarding the model can be found in section 2.1.2 and the Simulink model is provided in appendix A. To evaluate the baroreflex's response to a specific pressure stimulus, an open loop Simulink model was used. This model controls the input pressure of the numerical baroreflex, recording the activity of the vagal and sympathetic pathways, and monitoring changes in the controlled parameters, including resistance, cardiac elasticity, and heart period changes (vagal and sympathetic).

Four different pressure responses are evaluated: constant input, step input, ramp input and simulated heart beat.

5.2.1.1 Experiment 1: Constant pressure inputs

Firstly, the implementation of a constant pressure input to assess the behaviour of the baroreflex response. Four different input pressures were evaluated, specifically 60, 80, 100, and $120 mmHg$. Each pressure was maintained for 100 seconds to allow the system to reach steady-state.

5.2.1.2 Experiment 2: Step pressure inputs

Similarly to the constant pressure experiment, the behaviour of the baroreflex response was evaluated under three distinct step responses. As shown in figure 5.1, the step response was for pressure changes of 60 to $80 mmHg$, 80 to $100 mmHg$, and 100 to $120 mmHg$ were evaluated. Each step was initiated 30 seconds after the onset of the experimental.

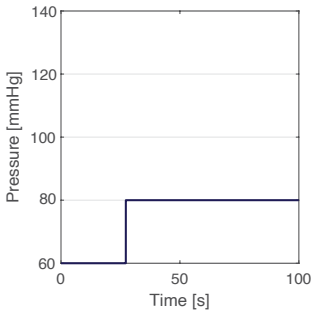

(a) From 60 to 80 $mmHg$

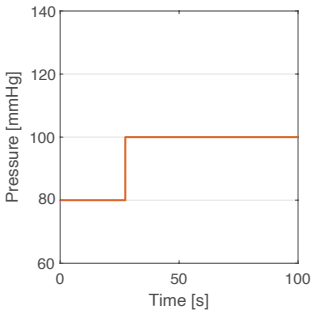

(b) From 80 to 100 $mmHg$

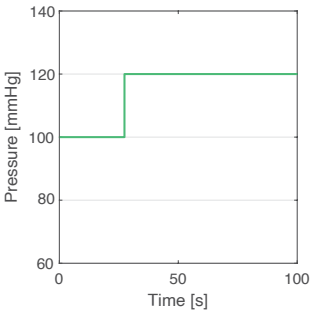

(c) From 100 to 120 $mmHg$

Figure 5.1: Step input for the numerical experiment

5.2.1.3 Experiment 3: Ramp pressure input

In addition to the constant and step inputs, the behaviour of the baroreflex response was also evaluated under a ramp input. As shown in figure 5.2, the ramp input starts at 60 mmHg and increases linearly to approximatly $125mmHg$ over a period of 60 seconds. The ramp input was chosen to mimic a gradual increase in blood pressure, which can occur in various clinical scenarios, such as during exercise.

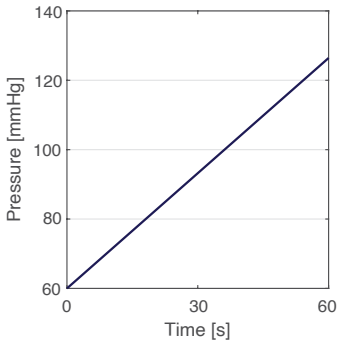

Figure 5.2: Ramp input for the numerical experiment

5.2.1.4 Experiment 4: Simulated heartbeat input

To further investigate the baroreflex response, a simulated heart beat was also used in the numerical experiment. The simulated heart beat input was generated using the summation of two sine waves, as illustrated in Figure 5.3 [160]

The blood pressure waveform was simulated using Simulink, and the resulting pressure waveform is shown in Figure 5.4.

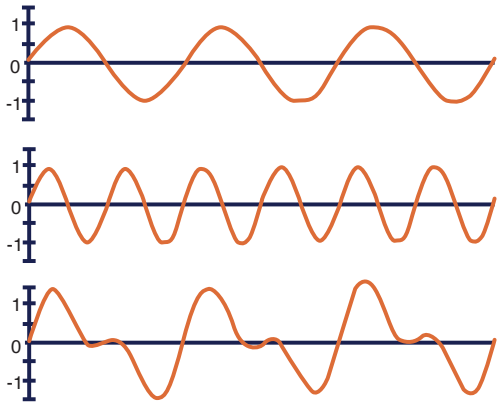

Figure 5.3: Simulated heart beat using two sine waves.

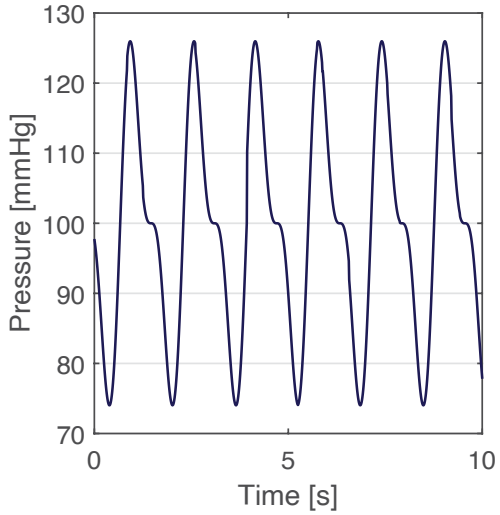

Figure 5.4: Simulated heart beat for the numerical experiment

5.2.2 Evaluation of the baroreflex response in a hybrid model

The MCL is set-up as described in chapter 2, in which the pressure sensor measures the fluctuations in pressure in the aorta. To investigate the dynamic response of a hybrid MCL, three closed-loop experiments were conducted, each involving a different stimulus. Specifically, the first experiment involved clamping the resistance of a tube using a Hoffman clamp, the second experiment involved reducing the volume of the system by draining water through a valve, and the third experiment involved suddenly increasing the overall volume of the system by adding water to the reservoir. These experiments were chosen to assess the baroreflex response under different conditions. The increase in resistance reflects the physiological scenario of a hypertensive patient or a stenosis.

The volume reduction experiments represents blood loss and the volume increase experiment represents the physiological scenario of increase in preload.

The parameters of the baroreflex response, including changes in heart period (vagal and sympathetic activity) and resistance, were active and monitored during each experiment together with the pressure and flow waveforms. For all experiment the hybrid mock loop set-up from section 2.3 was used.

5.2.2.1 Experiment 1: Resistance increase

During the experiment, the baroreflex control system was used to actively regulate the pressure. At the start of the experiment the baroreflex control system needs to stabilise the pressure by determining the appropriate HR and resistance value. Once the system is stabilised, which occurred approximately 60 seconds after initiation, the resistance was gradually increased. This experimental sequence was repeated five times to ensure repeatability.

To increase the resistance, a Hoffman clamp was positioned between the flow meter and the automated resistor.

5.2.2.2 Experiment 2: Volume reduction over time

Similar to the aforementioned experiment, the baroreflex control system was employed in this experiment to regulate the pressure and establish a stable system. However, in contrast to the previous protocol, the experimental manipulation involved the outflow of water from the MCL. To facilitate this process, a valve was placed between the flow meter and the automated resistor, allowing for control of the water outflow. The water was collected from the system and stored in a reservoir for a period of 60 seconds, after which the average reduction of water over time was calculated. This experiment was also repeated for five times.

5.2.2.3 Experiment 3: Sudden volume addition at specified time

This experiment shares similarities with the water reduction study. However, in this particular protocol, the experiment involved the addition of $2L$ water to the reservoir after a 60-second period, as opposed to the outflow of water. this experiment was also repeated five times to ensure repeatability.

In summary, the baroreflex response will be assessed purely in a numerical context, followed by its evaluation in a hybrid test setup involving three dynamic scenarios. An overview is given in table 5.1.

Test Number	Numerical Test Scenarios	Experimental Test Scenarios
1	Constant Pressure	Resistance Increase
2	Step Input	Volume Reduction
3	Ramp Input	Volume Increase
4	Heart Beat	-

Table 5.1: Different test scenarios for the numerical and experimental baroreflex experiments.

5.2.3 Data analysis

The collected data, acquired from the LabVIEW software (National Instruments, version 2021), was saved in a text file for further analysis. A custom MATLAB script (MathWorks, version R2021a) was developed to extract the pressure and flow waveforms from the recorded data. To filter the waveforms a second-order polynomial Savitzky-Golay filter with a frame length of 31 was applied.

5.3 Results

This section presents the results obtained from the evaluation of the baroreflex response in a numerical model and a hybrid model, respectively.

5.3.1 Evaluation of the baroreflex response in a numerical model

This section shows the results of four numerical experiments, which aimed to investigate the behaviour of the baroreflex under various conditions. Experiment 1 involved the application of constant pressure inputs to the numerical model to analyse the steady-state behaviour of the baroreflex response. Experiment 2 involved the application of step pressure inputs to investigate the transient behaviour of the baroreflex in response to sudden changes in blood pressure. Experiment 3 involved the application of ramp pressure inputs to investigate the dynamic behaviour of the baroreflex response to gradual changes

in blood pressure. Finally, Experiment 4 simulated a heartbeat input to investigate the interaction between the baroreflex and the physiological pressure curve.

5.3.1.1 Experiment 1: Constant pressure inputs

Figure 5.5 on the left side shows the activity in the neurological pathways, right shows the change in the effectors. The graphs show the effectors that operate in the systemic circulation, difference in cardiac contractility of the left ventricle [$mmHg/mL$] (E_{lv}), difference in resistanceextrasplanich pheriperal [$mmHgmin/L$] (R_{ep}), difference in resistance splanich peripheral [$mmHgmin/L$] (R_{sp}), difference in heart period vagal neurological pathway [s] (T_v) and difference in heart period sympathetic neurological pathway [s] (T_s). For a constant pressure of $60mmHg$ it can be seen that it takes around 10 seconds for the neurological activity and effectors to settle. the frequency of spikes in the afferent pathway [$spikes/s$] (f_{cs}) settles on $7spikes/s$, the frequency of spikes in the efferent sympathetic nerves [$spikes/s$] (f_{es}) on $13spikes/s$ and the frequency of spikes in the efferent vagal fibers [$spikes/s$] (f_{ev}) on $4spikes/s$. dE_{lv}, dR_{ep}, dR_{sp}, dT_v and dT_s settled on $1.1mmHg/mL$, $1.2mmHg \cdot s/mL$, $1.6mmHg \cdot s/mL$, $0.3s$ and $-0.3s$, respectively.

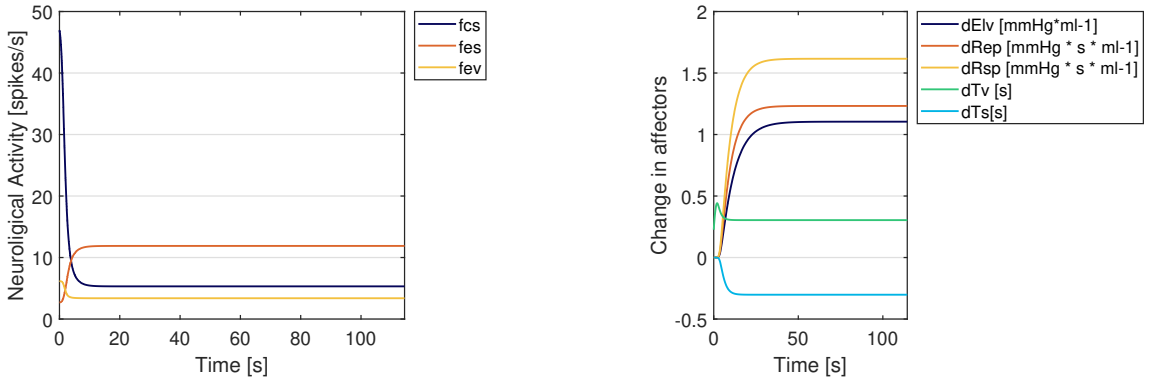

(a) Neurological activity (b) Change in effectors

Figure 5.5: Input constant pressure of $60mmHg$

For the results for a constant pressure input of $80mmHg$ is shown in figure 5.6. Similarly to the input of $60mmHg$ it takes around 10 seconds for the values to settle down. f_{cs} settles on $15spikes/s$, f_{es} on $7spikes/s$ and f_{ev} on $4spikes/s$. dE_{lv}, dR_{ep}, dR_{sp}, dT_v and dT_s settled on $0.8mmHg/mL$, $0.9mmHg \cdot s/mL$, $1.2mmHg \cdot s/mL$, $0.3s$ and $-0.2s$, respectively. Notably there is an overshoot in dT_v at a time of 5 seconds of $3.4s$

For the results for a constant pressure input of $100mmHg$ is shown in figure 5.7. Sim-

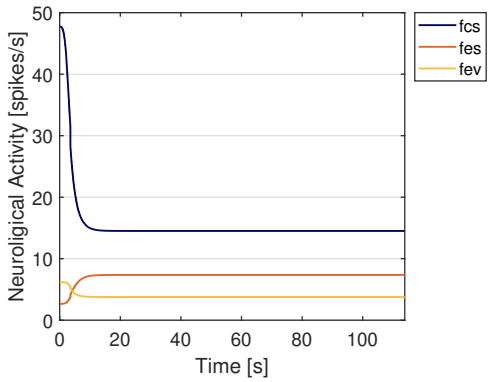

(a) Neurological activity

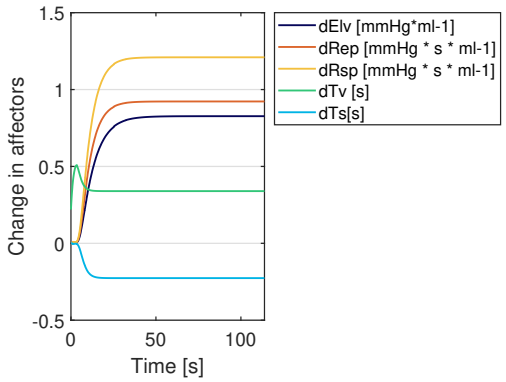

(b) Change in effectors

Figure 5.6: Input constant pressure of $80mmHg$

ilarly to the input of $60mmHg$ and $80mmHg$ it takes around 10 seconds for the values to settle down. f_{cs} settles on $33spikes/s$, f_{es} on $4spikes/s$ and f_{ev} on $6spikes/s$. dE_{lv}, dR_{ep}, dR_{sp}, dT_v and dT_s settled on $0.3mmHg/mL$, $0.4mmHg \cdot s/mL$, $0.5mmHg \cdot s/mL$, $0.5s$ and $-0.1s$, respectively. Notably there is an overshoot in dT_v at a time of 5 seconds of $5.2s$

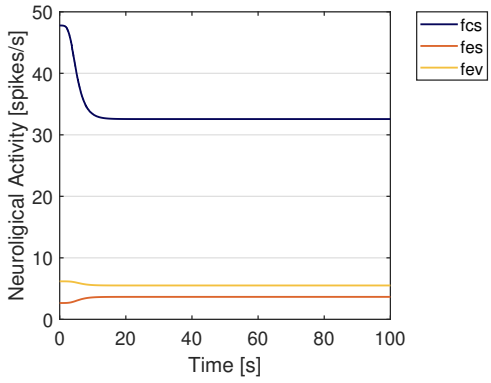

(a) Neurological activity

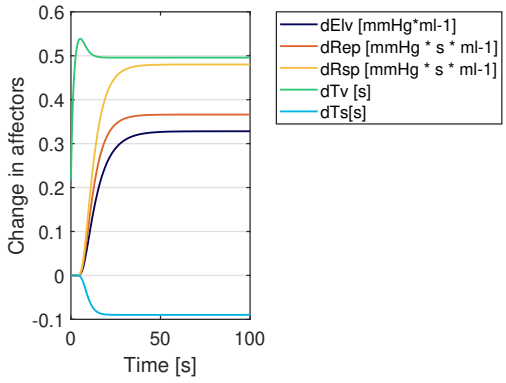

(b) Change in effectors

Figure 5.7: Input constant pressure of $100mmHg$

For the results for a constant pressure input of $120mmHg$ is shown in figure 5.8. Similarly to the input of $60mmHg$, $80mmHg$ and $100mmHg$ it takes around 10 seconds for the values to settle down. f_{cs} settles on $44spikes/s$, f_{es} on $3spikes/s$ and f_{ev} on $6spikes/s$. dE_{lv}, dR_{ep}, dR_{sp}, dT_v and dT_s settled on $0.07mmHg/mL$, $0.08mmHg \cdot s/mL$, $0.1mmHg \cdot s/mL$, $0.5s$ and $-0.02s$, respectively. Notably there is an overshoot in dT_v at a time of 5 seconds of $5.2s$

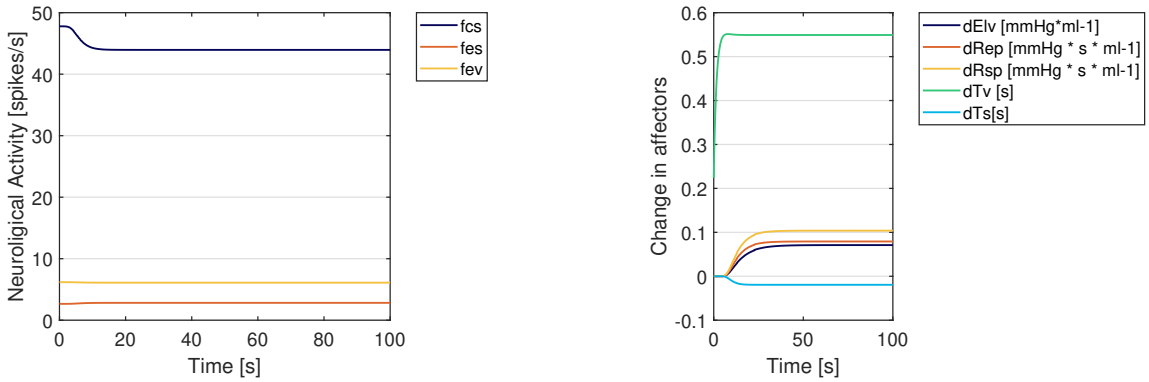

(a) Neurological activity (b) Change in effectors

Figure 5.8: Input constant pressure of $120mmHg$

5.3.1.2 Experiment 2: Step pressure inputs

Figure 5.9 shows the step response from $60mmHg$ to $80mmHg$. After stabilisation of the system ($t = 10seconds$) the same values as in figure 5.5 are observed. At the 30-second mark, the step response begins. The system then stabilises within the subsequent 10 seconds. The resulting stable values are consistent with those depicted in figure 5.6.

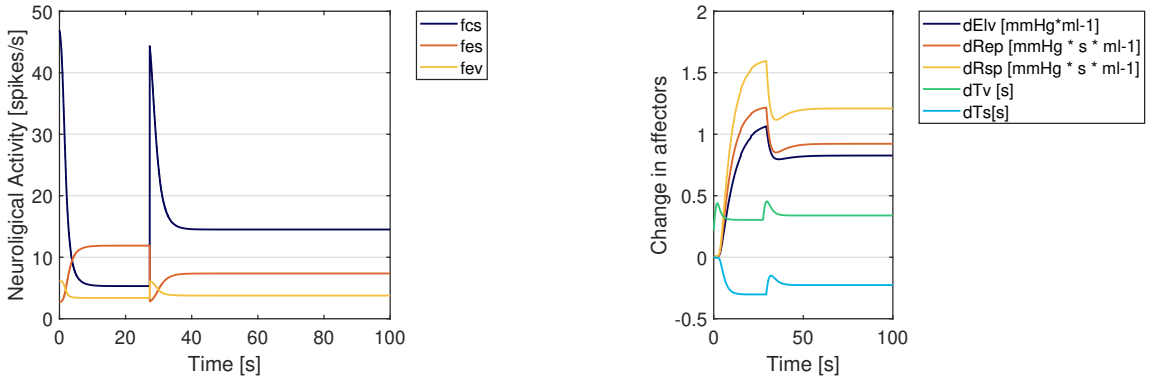

(a) Neurological activity (b) Change in effectors

Figure 5.9: Step from 60 to $80mmHg$ initiated at 30 seconds.

Figure 5.10 shows the step response from $80mmHg$ to $100mmHg$. After stabilisation of the system ($t = 10seconds$) the same values as in figure 5.6 are observed. At 30 seconds the step response is initiated, again we see that the system stabilises after 10 seconds. And the variables stabilise to the same values as in figure 5.7.

In figure 5.11, the step response transitions from $100mmHg$ to $120mmHg$. Once the system stabilises at $t = 10$ seconds, the observed values align with those in figure 5.7. The step response begins at 30 seconds, and, similar to the previous observation, the

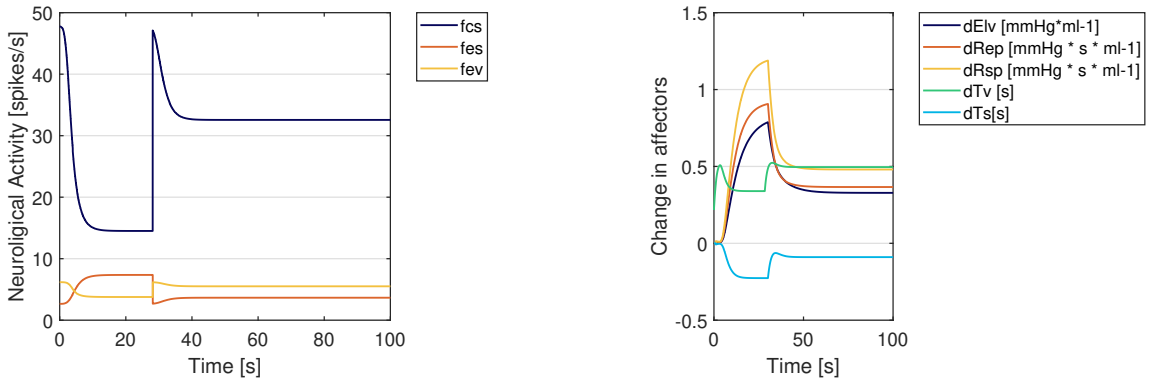

(a) Neurological activity (b) Change in effectors

Figure 5.10: Step from 80 to $100mmHg$ initiated at 30 seconds.

system reaches stability after an additional 10 seconds. The resulting stable values are consistent with those presented in figure 5.8.

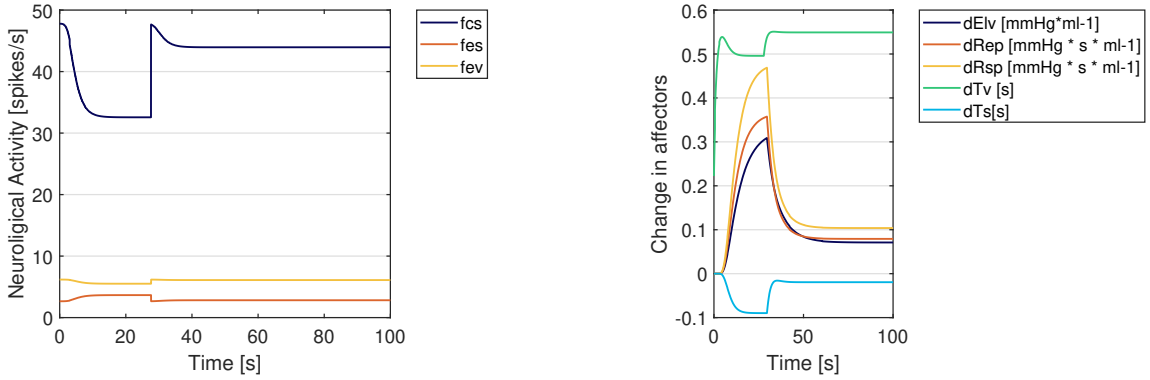

(a) Neurological activity (b) Change in effectors

Figure 5.11: Step from 100 to $120mmHg$ initiated at 30 seconds.

5.3.1.3 Experiment 3: Ramp pressure input

Figure 5.12 shows the effect of the ramp input on the reflex response. Additionally, the neurological activity and the effectors show a positively skewed parabola. The peak of this parabola for f_{cs}, f_{es} and f_{ev} is observed at 7 seconds, this is where the pressure is around $70mmHg$. For dT_v and dT_s the peak is observed around 9 and 10 seconds respectively. The pressure at these points in time are $70mmHg$ and $71mmHg$ respecivley. For dE_{lv}, dR_{ep} and dR_{sp} the peak is observed around 16 seconds where the pressure is $80mmHg$.

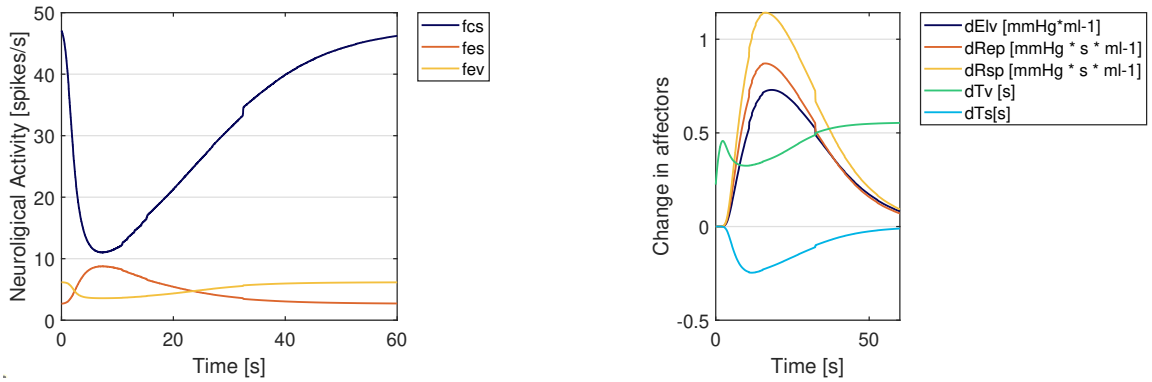

(a) Neurological activity (b) Change in effectors

Figure 5.12: Results of ramp input.

5.3.1.4 Experiment 4: Simulated heartbeat input

In figure 5.13 the results of the simulated heart beat are shown. After 10 seconds f_{cs} fluctuates between $48 spikes/s$ and $3 spikes/s$. f_{es} fluctuates between $14 spikes/s$ and $3 spikes/s$ and f_{ev} fluctuates between $6 spikes/s$ and $3 spikes/s$. Similarly, dE_{lv} varries between 0.83 and $0.80 mmHg/mL$, dR_{ep} between 1.05 and $1.00 mmHg \cdot s/mL$, dR_{sp} between 1.38 and $1.34 mmHg \cdot s/mL$, dT_v between 0.46 and $0.41 s$ and dT_s between -0.25 and $-0.27 s$.

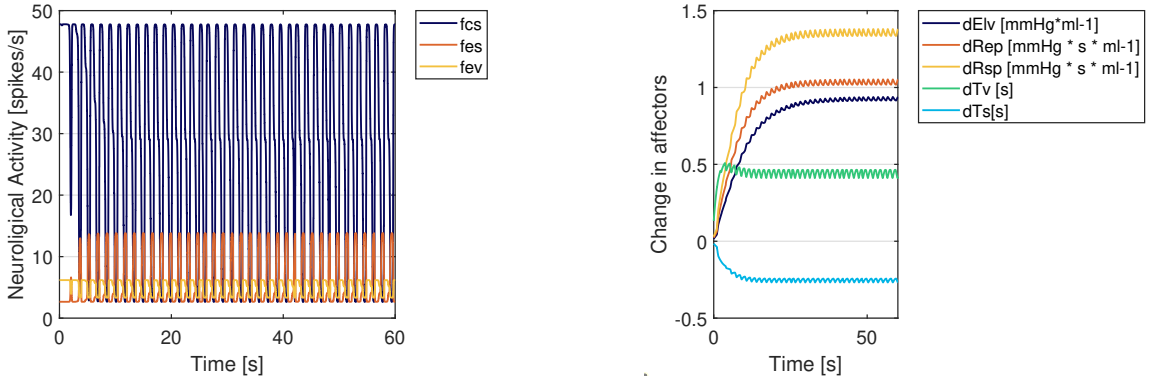

(a) Neurological activity (b) Change in effectors

Figure 5.13: Results of simulated blood pressure input. The figure displays the pressure curves (a) and the change in effectors of the baroreflex response (b)

These simulation results illustrate the response of the baroreflex to changes in pressure. The results are generated purely numerically using the Simulink model. Prior to conducting experiments in the hybrid test setup, the numerical pressure input values were also used for testing the LabVIEW baroreflex model. The results demonstrated consistency, enabling me to proceed with the dynamic tests.

5.3.2 Evaluation of the baroreflex response in a hybrid model

This section presents the outcomes of the closed-loop experiments on the H-MCL.

5.3.2.1 Experiment 1: Resistance increase

In the first experiment a step-wise increase in resistance was induced using a Hoffman clamp. Initial conditions were set to replicate a stable physiological state, with the MCL operating at a baseline heart rate and pressure. Figure 5.14 illustrates the time-course changes in the MCL pressure (a), flow (b) resistance (c) and heart rate (d). At 60 seconds the Hoffman clamp gradually started to close. Specifically, Figure 5.14a shows the rise in mean aortic pressure from 38 mmHg to 98 mmHg between 60 and 100 seconds, followed by stabilisation. Concurrently, mean downstream pressure decreased slightly from 13 mmHg to 11 mmHg. In Figure 5.14b, the flow rate, initially stable at around 3 L/min, exhibited a steep decrease to 0 L/min starting at 95 seconds, indicating full occlusion by the clamp.

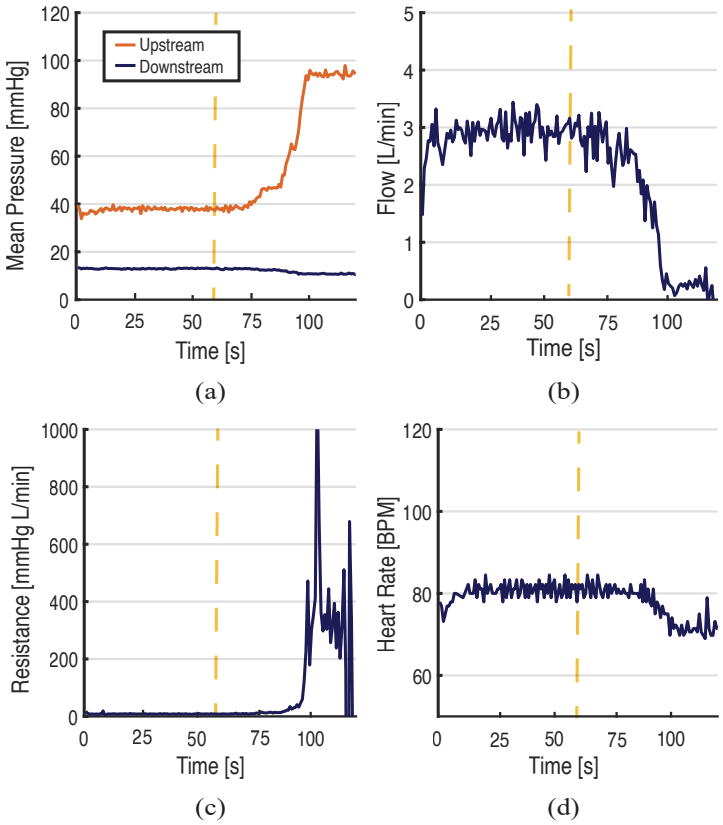

Figure 5.14: Experiment 1: Clamping - Time-course changes in the MCL aortic pressure (orange) downstream pressure (blue) (a), flow (b) resistance (c) and heart rate (d).

Adaptive changes were observed in the baroreflex effectors. As depicted in Figure 5.15, the numerical model initiated a reduction in resistance and heart rate approximately 80 seconds into the experiment. This indicates that the baroreflex detected an increase in pressure and adjusted its parameters to maintain a stable pressure. This adjustment is reflected in Figure 5.14d, where the heart rate in the MCL decreased from 80 BPM to 70 BPM. The resistance, initially around 8 mmHg·min/L, showed a steep increase after 100 seconds, coinciding with the full occlusion of the tube by the Hoffman clamp. Near 110 seconds the resistance value becomes negative as the backward flow occurs due to the fully occluded tube.

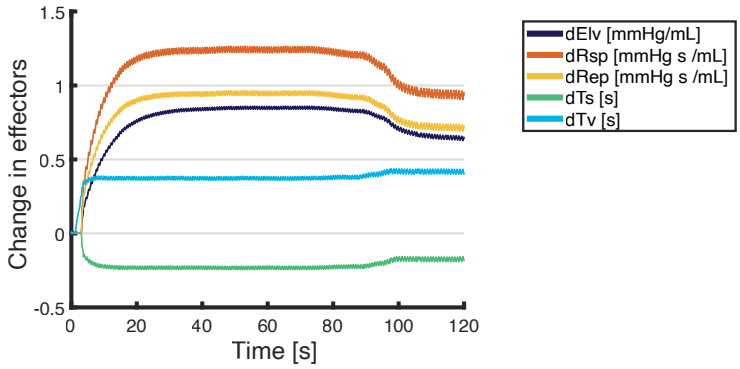

Figure 5.15: Dynamic changes in the baroreflex effectors in response to the induced resistance increase, illustrating the system's adaptive mechanisms.

5.3.2.2 Experiment 2: Volume reduction over time

The second experiment aimed to assess the response of the baroreflex model and the MCL to a gradual reduction in volume, simulating conditions like slow blood loss. Commencing from 60 seconds, the valve was progressively opened to reduce the volume within the MCL. A total of 2L water was taken out of the MCL. Figure 5.16 illustrates the time-course changes in MCL pressure (a), flow (b), resistance (c), and heart rate (d). Notably, Figure 5.16a shows a reduction in mean aortic pressure from 35 mmHg to 28 mmHg between 60 and 120 seconds, with downstream pressure decreasing from 13 mmHg to 8 mmHg. Despite the volume reduction, the flow rate remained stable at around 3 L/min throughout the experiment, as depicted in Figure 5.16b.

The baroreflex effectors responded adaptively to the volume and pressure reduction. Both resistance and heart rate exhibited slight changes, as shown in Figure 5.17. Specifi-

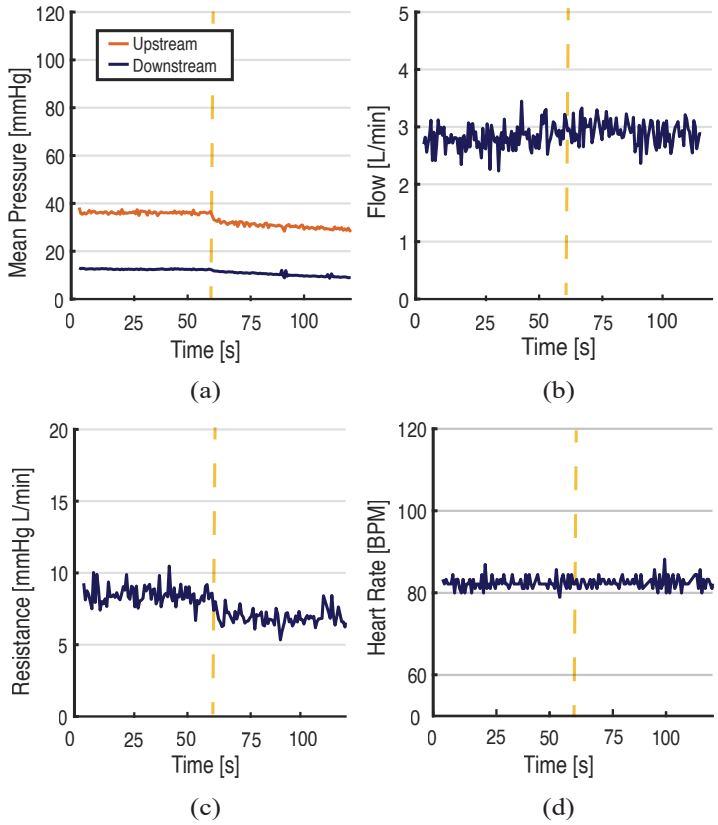

Figure 5.16: Experiment 2: Volume Reduction - Time-course changes in the MCL aortic pressure (orange), downstream pressure (blue) (a), flow (b), resistance (c), and heart rate (d).

cally, resistance decreased slightly from 9 mmHg·min/L, stabilising at 7 mmHg·min/L from 70 seconds onwards (Figure 5.16c). The heart rate increased marginally from 81 to 83 BPM (Figure 5.16d), indicating a compensatory response to maintain hemodynamic stability.

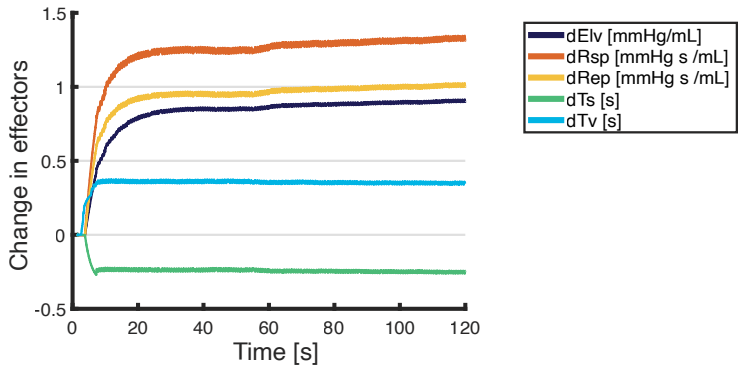

Figure 5.17: Adaptive changes in the baroreflex effectors in response to volume reduction, demonstrating the system's compensatory mechanisms to maintain hemodynamic stability.

5.3.2.3 Experiment 3: Sudden volume addition at specified time

The third experiment aimed to evaluate the response of the baroreflex model and the MCL to a sudden increase in volume. After 60 seconds of stable operation, 2 litres of water were rapidly added to the reservoir, significantly increasing the system's volume. Figure 5.18 illustrates the time-course changes in MCL pressure (a), flow (b), resistance (c), and heart rate (d). Notably, Figure 5.18a shows an increase in both aortic and downstream pressures from 37 mmHg to 42 mmHg, and 13 mmHg to 17 mmHg, respectively, while the flow rate remained stable at around 3 L/min.

The baroreflex effectors demonstrated an adaptive response to the increased volume and pressure. The baroreflex model responded to the pressure increase by decreasing resistance and heart rate. In the MCL, no notable change in resistance was observed, likely due to the minimal extent of the change, maintaining an average resistance of 8 mmHg·min/L. However, the heart rate showed a decrease from 82 to 79 BPM following the volume increase, indicating the system's compensatory mechanism in action.

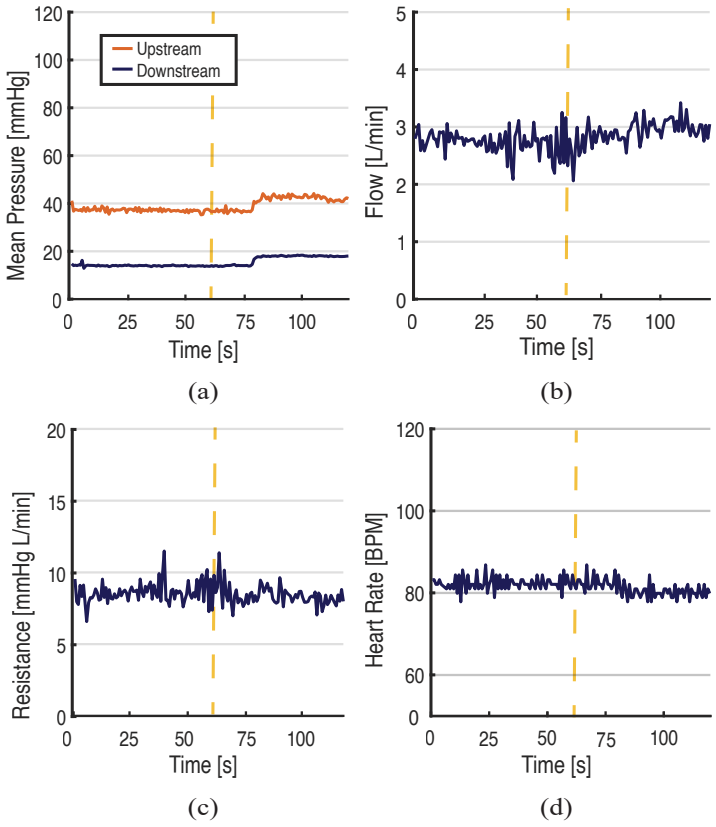

Figure 5.18: Experiment 3: Sudden Volume Addition - Time-course changes in the MCL aortic pressure (orange), downstream pressure (blue) (a), flow (b), resistance (c), and heart rate (d).

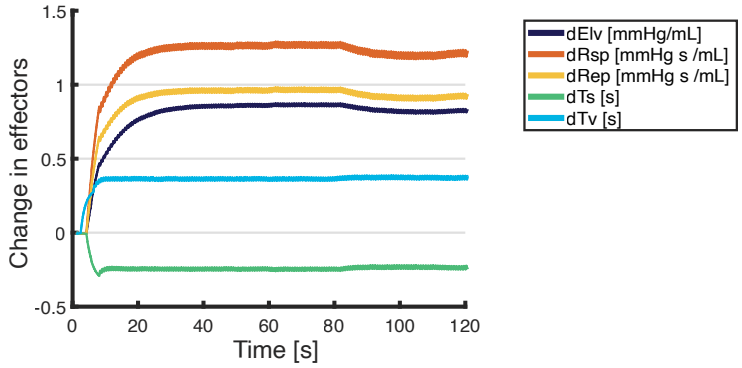

Figure 5.19: Dynamic changes in the baroreflex effectors in response to sudden volume addition, demonstrating the system's adaptability to acute hemodynamic changes.

5.4 Discussion

The results of the 'resistance increase' experiment demonstrated that the onset of clamping did not immediately affect the pressure curves in the MCL in the first 15 seconds. Moreover, the baroreflex effectors, including E_{lv}, R_{ep}, R_{sp}, T_v, and T_s, changed throughout the clamping to maintain the pressure. Specifically, the mean values of E_{lv}, R_{ep}, R_{sp} effectors decreased as the pressure increased and the mean values of T_v, and T_s increased, indicating the activation of the baroreflex response. These findings suggest that the baroreflex response can effectively regulate the blood pressure in the MCL under conditions of resistance increase. This is consistent with previous in-vivo studies, for example, a study done by Rascher et al. found that cardiac output reduced when total peripheral resistance was increased in hypertensive rats [161] and by Burratini et al. who noted a reduction in cardiac output in cats during venous constriction [162].

However, in the later stages of the experiment, the baroreflex was unable to maintain the pressure. After a duration of 78 seconds, the maximum upstream pressure increased to $131 mmHg$, which was $11 mmHg$ greater compared to the stable conditions. Although the baroreflex was observed to be active and responding by decreasing the E_{lv}, R_{ep} and R_{sp} and increasing T_v and T_s, it was unable to maintain homeostasis. Further analysis of the results showed an additional increase in pressure at the end of the clamping process, whereby the maximum upstream pressure reached a peak value of $173 mmHg$. Furthermore, no pulse was detected in the downstream pressure curve, which indicated that the tube was fully clamped. It is important to note that the set-up was an in-series connec-

tion, and not a complex arterial tree in vivo. Although the baroreflex in the MCL was still actively attempting to decrease pressure, as indicated by the changes in the effectors, it was unable to maintain homeostasis. These findings show the limitations of the in-series arterial model of the MCL, which does not fully replicate the physiological arterial system. Using an anatomical arterial tree might increase the resemblance with the native CVS, however, will increase the complexity of the set-up. Additionally, the MCL does not regulate E_{lv}. Had E_{lv} been incorporated into the regulation mechanism, the MCL could have potentially maintained pressure for an extended duration.

The results of the volume reduction experiment showed that although $2L$ was taken from the MCL, there was only reduction of $6mmHg$ upstream peak pressure. This indicates that the baroreflex was able to successfully maintain pressure by increasing E_{lv}, R_{ep}, and R_{sp}, and reducing T_v and T_s. Similar results were reported by Cuenca-Navalon et al. who studied the effect of a $500mL$ volume reduction [118]. Their results also showed a small reduction in mean arterial pressure from $90mmHg$ to $88mmHg$, a reduction in venous pressure from $6mmHg$ to $3mmHg$, and an increase in systemic resistance from $1mmHg \cdot /mL$ to $1.05mmHg \cdot s/mL$. Jansen et al. also reported similar results when studying the effect of a $450mL$ volume reduction [121]. They observed a variation of resistance from 3.25 to $4.50mmHg \cdot s/mL$. During our volume reduction experiment, there was a change in resistance of $0.22mmHg \cdot s/mL$, and the venous peak pressure reduced from $23mmHg$ to $17mmHg$.

Similar to the 'resistance increase' experiment the mechanical part of the MCL did not regulate the E_{lv} during the volume reduction experiment. Nonetheless, this lack of regulation did not appear to affect the pressure regulation in this experiment. This finding is consistent with the results reported by Jansen et al. [121], who conducted a study comparing the effectiveness of different baroreflex parameters in regulating pressures during a volume reduction experiment. Specifically, their study found no substantial difference in pressure regulation when all baroreflex parameters were active versus when the E_{lv} was not active after 60 seconds.

Comparable results were found for the 'volume increase' experiment. With the baroreflex active only a slight variation of upstream peak pressure was observed from $118mmHg$ to $121mmHg$. Similar results were observed by Cuenca-Navalon et al. who observed a similar reduction of systemic resistance when volume was added to the system when

the baroreflex was activated [118]. In their study mean arterial pressure increased from $90mmHg$ briefly to $95mmHg$ however after 40 seconds this was reduced to $92mmHg$. The central venous pressure increased from $3mmHg$ to $6mmHg$ and the sysemtic arterial resistance reduced from $1.02mmHg \cdot /mL$ to $1.0mmHg \cdot s/mL$.

5.5 Conclusion

This study aimed to investigate the ability of the baroreflex system to regulate blood pressure in the MCL under different stimuli. The experiments conducted provided valuable insights into the behaviour of the baroreflex response within the MCL under various conditions.

The findings from the resistance increase experiment revealed that while the onset of clamping had a negligible impact on the pressure curves within the initial 15 seconds. The baroreflex effectors, including E_{lv}, R_{ep}, R_{sp}, T_v, and T_s, dynamically adjusted in response to the changing pressures. Specifically, there was a decrease in E_{lv}, R_{ep}, and R_{sp} effectors and an increase in T_v and T_s as the pressure increased. Despite the baroreflex's active response, it couldn't maintain homeostasis beyond 78 seconds, with the maximum upstream pressure reaching $173mmHg$. This experiment highlighted the limitations of the in-series arterial model of the MCL and the potential benefits of incorporating E_{lv} into the regulation mechanism. In the volume reduction experiment, the removal of $2L$ from the MCL led to a modest $6mmHg$ dip in the upstream peak pressure. The baroreflex successfully maintained pressure by modulating the effectors. Specifically, there was an increase in E_{lv}, R_{ep}, and R_{sp}, and a decrease in T_v and T_s. Lastly, the addition of volume to the MCL resulted in a minor increase in the upstream peak pressure from $118mmHg$ to $121mmHg$.

The limitations of the in-series arterial model of the MCL were also highlighted, particularly the lack of regulation of E_{lv}. Incorporating E_{lv} into the mechanical regulation mechanism could potentially improve the ability of the MCL to maintain pressure. It is important to note that the MCL does not fully replicate the physiological arterial system. Whilst using an anatomical arterial tree may increase the resemblance with the native cardiovascular system it would also increase the complexity of the setup.

Overall, this study demonstrated the effectiveness of the employed baroreflex mech-

anism in regulating pressure within the MCL. Future studies could focus on further exploring the limitations and potential improvements of the MCL model and investigating the effect of CADs on the baroreflex response.

Chapter 6

General Discussion and Conclusions

MCLs play an important role in cardiovascular research, device development, and testing. It's essential to continuously refine and develop MCLs to increase the accuracy and adaptability of the testing environment. The more precisely an MCL can simulate the human CVS, the more its results align with real-world clinical scenarios. This accuracy becomes especially important when evaluating CADs. Given that the CVS can present a wide array of conditions and pathophysiologies, a versatile MCL is invaluable for simulating various patient conditions and CADs. This thesis has contributed to improving the flexibility and accuracy of MCLs by developing a flexible automated vascular resistor and implementing the baroreflex response. To conclude this work, this chapter offers a summation of the findings, a discussion and a conclusion. The section begins with a presentation of the main findings. This is followed by a discussion on the feasibility and efficiency of the automated resistor and left ventricle simulator when integrated with the baroreflex response. An assessment of the strengths and weaknesses of the MCL is then provided, considering the system as a whole and its broader implications in the field. The section concludes with remarks on potential directions for future research.

6.1 Summary of the main findings

The overarching aim of this thesis is the development of the next-generation MCL with baroreflex response. This work is driven by three main objectives of which the first was the control of the cardiac output, described in chapter 3. The HR was regulated through the linear motor's velocity and displacement. A machine learning model pre-

dicted the stroke volume, from which the ventricle volume was derived. Analysis showed that the linear motor effectively controlled HR. For the machine learning model the Rational Quadratic GPR model had the highest accuracy. Upon analyzing the PV-loop of the left ventricle simulator, it became evident that it did not accurately represent the native heart, making it not possible to determine ventricle contractility.

Secondly, an automated vascular resistor was designed and studied in chapter 4. This involved examining the variation in resistance across three tubes of differing dimensions. Furthermore, the step response of the resistor was analysed. The results showed that the resistor could effectively adjust the resistance for three tubes within the physiological range. Moreover, for pulsatile flow the resistor was able to stabilise from a step response within three cardiac cycles.

Lastly, the baroreceptor response was ultimately integrated into the MCL in chapter 5. The mathematical model of the baroreflex was implemented into LabVIEW and communicated in real-time with the MCL. The performance of the baroreflex was assessed by observing its response to changes in resistance and volume fluctuations. When resistance increased the baroreflex consistently maintained pressure during the experiment's initial phase. In the volume reduction test, pressures consistently remained stable. Meanwhile, in the volume addition experiment only minor pressure increases were observed.

6.2 Discussion

Chapter 4 of this thesis described the characterization and control mechanisms of the automated vascular resistor. This resistor was used in Chapter 5, where its capacity to control the vascular resistance of the baroreflex response was tested. During the resistor's characterisation, an inversely proportional relationship between resistance and internal diameter was observed across three different tubes. Analysis of their normalised values offered evidence that the resistor behaves consistently across varying tube sizes, a requirement that was needed for its eventual combination with the MCL. Although the tube size and stiffness differed in the final setup, the system still accurately controlled the resistance with the active baroreflex for this tube. This supports that the resistor can be used in various positions and experimental setups.

Throughout the mock loop's stabilisation, the resistor responded effectively to values

calculated by the baroreflex model. During the step-response experiments, the resistor's performance was assessed using step sizes ranging from 5 to $15 mmHgL/min$, with time responses varying between 0.5 and $2.1 s$. Under pulsatile conditions, a step size of $10 mmHgL/min$ required three cardiac cycles for stabilisation. In the baroreflex model, resistance step sizes varied between 0 and $2 mmHgL/min$, suggesting that the resistor can aptly respond to resistance changes in line with the baroreflex model's response. This adaptability was evident in the sudden volume addition experiment. The results demonstrated that even with abrupt volume changes, the resistor and baroreflex model effectively regulate pressure, a similar response to that observed during the volume reduction experiment.

Other frequently used resistors are proportional valves [118], [120], [121], whose resistance is determined by the valve's orifice size. While these valves have proven effective in regulating resistance in combination with the baroreflex response, they come with predefined resistance values. This means they don't adapt to changes within the MCL, such as the introduction of arterial trees. Furthermore, their rigidity often confines them to a specific position and tube size.

In contrast, the resistor introduced in this thesis can be clamped onto tubes of varying sizes and wall thicknesses, showcasing its versatility. This automated resistor can improve MCL setups, especially compared to those using mechanical screws [73] or solely simulating resistance in the numerical section of the H-MCL [106]. The control algorithm proposed in this thesis has also been demonstrated to be efficient in controlling baroreflex resistance, eliminating the need for a proportional integrator.

The cardiac output in the baroreflex is controlled by changing HR and ventricle contractility. In chapter 3, the strategy of controlling the linear motor's velocity to regulate HR was explored and found to be effective, especially when combined with the baroreflex model discussed in chapter 5. During the MCL stabilisation phase the HR increased, suggesting that the linear motor effectively responds to the changes calculated by the baroreflex model.

In subsequent experiments, including the increase in resistance and volume addition, shifts in the effector were followed by corresponding changes in HR. Throughout these tests, the linear motor consistently aligned its response of HR with the calculated value of the baroreflex model.

Furthermore, chapter 3 focused on controlling the contractility of the left ventricle simulator. However, from the analysis of preload effects on the left ventricle simulator, as depicted in figure 3.9, it became evident that the ventricle simulator could not replicate the native heart's responses. This limitation persisted whether changes were made to the mock loop's total volume or the linear motor's stroke length. The PV-loop's shape reacted differently to preload variations compared to a native heart, making it not possible to determine contractility from the E_{es} slope.

The HR control was successful, but the model could not control contractility. While the contractility control was factored into the baroreflex calculations, it wasn't directly altered in the hydraulic part of the model. Despite this, the system sustained the desired pressure levels without needing to adjust the left ventricle simulator's contractility. This outcome implies that the baroreflex mechanism can function adequately without active contractility control, which alligns with the findings of Jansen-Park et al. [121].

Nevertheless, for a more accurate physiological simulation, integrating all relevant controls, including contractility, would potentially offer enhanced precision and a more genuine portrayal of the CVS. Though ventricle contractility can be adjusted in the current literature [73], it has yet to be implemented into a pulsatile MCL along side a numerical model of the baroreflex response. Efforts have been made by defining contractility through rotational pump speed in continuous flow MCL models [120] or via use of look-up tables [121]. Incorporating it would provide a more authentic representation of the native CVS. A different ventricle driving system is proposed in section 6.5.

6.2.1 Disciplinary Impacts

Presently, according to BSI [163], there aren't any specific standards tailored for MCL requirements. The criteria mentioned for MCLs only requires the researcher to document the simulated heart, vascular compliance, and resistance. Given the vast diversity and differences among MCLs, there's a clear case for an international standard addressing MCL testing requirements for CAD. Enhancements to the standard test bed, like incorporating the baroreflex, can optimise in-vitro testing platforms, thereby minimising the reliance on in-vivo trials.

The research presented in this thesis extends beyond merely using the MCL as a testing platform for CADs. It provides students the opportunity to explore the effects of

resistance changes on the CVS by adjusting the resistor, and to observe the impact of HR variations on pressure and flow waves. In addition, students can examine the baroreflex response to perturbations and grasp the challenges and constraints of in-vivo experiments.

6.3 Limitations

As with all scientific research, while the methods and results have shown promise, it's essential to acknowledge and reflect on certain constraints and areas for improvement.

6.3.1 Experimental limitations

A significant limitation lies in the design of the compliance chamber. Currently, the chamber is rigid, with fixed air and water volumes that remain static throughout experiments. The ventricle chamber utilised, with a capacity of $200mL$, is notably larger than the average human ventricles, which range from 62 - $120mL$ for males and 58 - $103mL$ for females [164]. This discrepancy underscores a potential area for refinement.

Furthermore, the current ventricle design falls short in emulating the native contractility of the heart. The alterations in speed and stroke length don't mirror the nuanced changes in force and shortening observed in native ventricular contractility. The left ventricle's replication of the Frank-Starling response is also presently inadequate. While this mechanism's incorporation extends beyond the scope of this thesis, its inclusion would undoubtedly enhance the MCL's resemblance to the CVS.

The choice of fluid for experiments also presents a limitation. Tests were conducted using water, which doesn't capture the viscosity of blood. More accurate simulations might be achieved using water-glycerin mixtures or other suitable alternatives [165].

Another limitation lies in simulating the left ventricle's atria. Employing a smaller reservoir to account for atrium compliance could enhance the accuracy of the model. This adjustment might also optimise the functionality of the ventricle valves. Currently, these valves struggle to maintain pressure and fail to accurately replicate the isovolumic contraction and relaxation phases of the cardiac cycle.

Another notable limitation is the absence of real-time volume visualisation in the machine learning model for the ventricle program. Incorporating this feature would offer

deeper insights into the mock loop's behaviour, allowing for on-the-fly adjustments to system compliance and water volume. Such real-time adjustments could ensure a more faithful representation of the CVS. Without this capability, assessing the system's repeatability becomes challenging.

Regarding HR regulation, the current system only achieves a maximum of 140 beats per minute. This imposes a constraint on the baroreflex response, as the HR cannot exceed this threshold. In certain physiological conditions, the HR can surge to as high as 200 beats per minute. The inability of the current system to simulate such scenarios is a clear limitation.

Furthermore, the baroreflex has only been evaluated under three distinct dynamic scenarios. To truly gauge its efficacy in maintaining system pressure, it would be beneficial to juxtapose these dynamic responses against a scenario where the baroreflex is deactivated. Such a comparison would provide a clearer picture of the baroreflex's role in pressure regulation.

6.3.2 Computational limitations

Regarding the numerical component of the MCL, data acquisition and real-time simulation of the baroreflex were conducted using LabVIEW. A notable limitation of the current LabVIEW-based baroreflex model is its sampling rate, which is capped at $100Hz$ due to computer hardware constraints. For a more accurate representation, especially to capture the intricacies of the full cardiac cycle, a sampling rate of $1000Hz$ would be ideal.

The baroreflex model employed in this study is based on the work of Ursino et al. [117]. While this model is among the most comprehensive available, it's important to highlight certain discrepancies and simplifications. Firstly, Ursino's model primarily uses aortic pressure as its sole input. In reality, the baroreflex system also incorporates pressure readings from sensors located in the carotid arteries. Additionally, Ursino's model differentiates between resistances in the splanchnic and extrasplanchnic arteries. In contrast, the current MCL simplifies this by representing them with a single resistor. Furthermore, while Ursino's model accounts for variations in venous volume as part of the baroreflex mechanism, such dynamics are not currently simulated in the MCL of this study.

In summary, while the MCL presents a promising approach to simulating the CVS, it is imperative to recognise its current limitations, both experimental and computational.

These constraints, ranging from hardware design to fluid choice and from sampling rates to model simplifications, underscore the importance of continuous refinement in future iterations. By addressing these identified areas of improvement, subsequent studies can aspire to achieve a more accurate and comprehensive representation of the CVS.

6.4 Conclusion

The aim of this thesis was to develop the next-generation MCLs by addressing the pressure regulations of the CVS and striving to develop a flexible and accurate MCL.

The accomplishments of this work include:

- The precise regulation of HR through the control of the linear motor's velocity and displacement.
- The introduction of a versatile automated vascular resistor capable of adapting to tubes of diverse dimensions and promptly responding to fluctuations in physiological parameters.
- The successful integration and dynamic evaluation of the baroreceptor response into the MCL.

Beyond the technological and academic contributions, this research provides students and researchers a platform to study the CVS. From resistance changes and HR variations to the baroreflex responses and the challenges of in-vivo experiments.

In summation, while this work has achieved substantial advancements in MCLs, the journey towards a perfectly representative model of the human CVS continues. The findings and innovations presented herein not only increases our existing understanding but also provide a robust foundation for future research work.

6.5 Future Work

Future research should emphasise adapting the left ventricle simulator. One approach involves transitioning the left ventricle pump to a volume-controlled pump, akin to the methodology described by Colacino et al. [73]. In their model, pressure measured within the left ventricle is relayed to its mathematical counterpart. The computed reference

volume then dictates the piston's position via a PI controller. Inputs to this mathematical model include the HR and contractility, whereas the SVR and pressure in the mean systemic circuit arise from modifications made to the hydraulic circuit.

Alternatively, the model presented by Vaes et al. can be adopted. This model integrates muscle fiber stress and left ventricle volume to regulate ventricular pressure [122]. Given that these models require real-time, precise volume determinations, redesigning the linear motors to operate as piston pumps might be advantageous. This design would allow for volume determinations based solely on piston position. The current design does not permit this due to the inclusion of a flexible membrane.

For optimal elastance, ventricular flow, and simulations of the Frank-Starling law, the employment of pressurised chambers seems most suitable for heart representation. Both pneumatic and hydraulic pressurised chambers have received successful mentions in academic literature. For instance, the left ventricle can be fabricated from an elastic latex bag situated within a water chamber. Here, the water chamber's pressure prompts water to evacuate the ventricle. An alternative setup places the elastic bag within a pneumatic chamber where air pressure expels the water from the left ventricle [29]. If shape recreation is not a priority, vertical pipes can be used. Compressed air introduced to the ventricle during systole or released during diastole can emulate the arterial pulse [98].

Secondly, it would be interesting to integrate more machine learning techniques into the MCL to enhance its intelligence. For instance, the baroreflex model could be transitioned into a machine learning model to better capture patient-specific data. This would elevate the accuracy of the MCL, enabling more personalised testing for CADs.

Lastly, the MCL might also benefit from incorporating an automated or variable compliance chamber. Consider, for instance, the design proposed by Taylor et al. They introduced an automated compliance chamber comprising a cylindrical space where water and air are separated by a membrane [140]. The change in compliance is governed by the pressure in the air compartment, exerting increased force on the membrane. Both a pressure sensor situated in the fluid chamber and a displacement sensor tracking membrane deflection serve as real-time inputs for a control algorithm. Employing a variable compliance chamber provides users with enhanced control over pressure and flow curves. Consequently, users can fine-tune the compliance during the MCL operation.

References

[1] F. Cappon, T. Wu, T. Papaioannou, X. Du, P.-L. Hsu, and A. W. Khir, "Mock circulatory loops used for testing cardiac assist devices: A review of computational and experimental models," *The International Journal of Artificial Organs*, vol. 44, no. 11, pp. 793–806, 2021.

[2] B. H. Foundation, "Tipping point: Why heart care must be prioritised now," Tech. Rep., 2022.

[3] B. Collins, P. Bandosz, M. Guzman-Castillo, *et al.*, "What will the cardiovascular disease slowdown cost? modelling the impact of cvd trends on dementia, disability, and economic costs in england and wales from 2020–2029," *PloS one*, vol. 17, no. 6, e0268766, 2022.

[4] "Organ donation and transplantation - activity figures for the uk as at 9 april 2021," NHS, Tech. Rep., 2021.

[5] S. Susen, A. Rauch, E. Van Belle, A. Vincentelli, and P. Lenting, "Circulatory support devices: Fundamental aspects and clinical management of bleeding and thrombosis," *Journal of Thrombosis and Haemostasis*, vol. 13, no. 10, pp. 1757–1767, 2015.

[6] K. Werdan, S. Gielen, H. Ebelt, and J. S. Hochman, "Mechanical circulatory support in cardiogenic shock," *European heart journal*, vol. 35, no. 3, pp. 156–167, 2014.

[7] G. Makdisi and I.-w. Wang, "Extra corporeal membrane oxygenation (ecmo) review of a lifesaving technology," *Journal of thoracic disease*, vol. 7, no. 7, E166, 2015.

[8] S. Unverzagt, M. Buerke, A. de Waha, *et al.*, "Intra-aortic balloon pump counterpulsation (iabp) for myocardial infarction complicated by cardiogenic shock," *Cochrane Database of Systematic Reviews*, no. 3, 2015.

[9] S. Christiansen, A. Klocke, and R. Autschbach, "Past, present, and future of long-term mechanical cardiac support in adults," *Journal of cardiac surgery*, vol. 23, no. 6, pp. 664–676, 2008.

[10] R. John, F. Kamdar, K. Liao, M. Colvin-Adams, A. Boyle, and L. Joyce, "Improved survival and decreasing incidence of adverse events with the heartmate ii left ventricular assist device as bridge-to-transplant therapy," *The Annals of thoracic surgery*, vol. 86, no. 4, pp. 1227–1235, 2008.

[11] U. P. Jorde, S. S. Kushwaha, A. J. Tatooles, *et al.*, "Results of the destination therapy post-food and drug administration approval study with a continuous flow left ventricular assist device: A prospective study using the intermacs registry (interagency registry for mechanically assisted circulatory support)," *Journal of the American College of Cardiology*, vol. 63, no. 17, pp. 1751–1757, 2014.

[12] E. J. Molina, P. Shah, M. S. Kiernan, *et al.*, "The society of thoracic surgeons intermacs 2020 annual report," *The Annals of thoracic surgery*, vol. 111, no. 3, pp. 778–792, 2021.

[13] J. F. Cornhill, "An aortic-left ventricular pulse duplicator used in testing prosthetic aortic heart valves," *The Journal of thoracic and cardiovascular surgery*, vol. 73, no. 4, pp. 550–558, 1977.

[14] S. Magder, "Understanding central venous pressure: Not a preload index?" *Current opinion in critical care*, vol. 21, no. 5, pp. 369–375, 2015.

[15] A. R. Vest and F. A. Heupler, "Chapter 2 afterload," 2019. [Online]. Available: https://api.semanticscholar.org/CorpusID:4781257.

[16] M. Pillon, H. Duffour, and M. Jufer, "In vitro experiments: Circulatory assist device interaction with a virtual cardiovascular system," in *1992 14th Annual International Conference of the IEEE Engineering in Medicine and Biology Society*, IEEE, vol. 2, 1992, pp. 740–741.

[17] Y. Shi and H. Yang, "Mock circulatory test rigs for the in vitro testing of artificial cardiovascular organs," *Journal of Medical Engineering & Technology*, vol. 43, no. 4, pp. 223–234, 2019.

[18] Y. Shi, T. Korakianitis, Z. Li, and Y. Shi, "Structure and motion design of a mock circulatory test rig," *Journal of medical engineering & technology*, vol. 42, no. 6, pp. 443–452, 2018.

[19] G. Pontrelli and E. Rossoni, "Numerical modelling of the pressure wave propagation in the arterial flow," *International journal for numerical methods in fluids*, vol. 43, no. 6-7, pp. 651–671, 2003.

[20] A. M. Bavo, G. Rocatello, F. Iannaccone, J. Degroote, J. Vierendeels, and P. Segers, "Fluid-structure interaction simulation of prosthetic aortic valves: Comparison between immersed boundary and arbitrary lagrangian-eulerian techniques for the mesh representation," *PloS one*, vol. 11, no. 4, e0154517, 2016.

[21] K. H. Fraser, M. E. Taskin, B. P. Griffith, and Z. J. Wu, "The use of computational fluid dynamics in the development of ventricular assist devices," *Medical engineering & physics*, vol. 33, no. 3, pp. 263–280, 2011.

[22] S. Hales, *Statistical essays: Containing haemostaticks, or an account of some hydraulick and hydrostatical experiments on the blood and blood-vessels of animals, etc.* London: Innys & Manby, 1733, vol. 2.

[23] E. Weber, *Wellenlehre Experimente Gegruendet 1825*. [Online]. Available: https://books.google.co.uk/books?id=MUszzwEACAAJ.

[24] O. Frank, *Die grundform des arteriellen pulses: mathematische analyse. erste abhandlung*. 1899.

[25] N. Westerhof, J.-W. Lankhaar, and B. E. Westerhof, "The arterial windkessel," *Medical & biological engineering & computing*, vol. 47, no. 2, pp. 131–141, 2009.

[26] S. M. Toy, J. Melbin, and A. Noordergraaf, "Reduced models of arterial systems," *IEEE transactions on biomedical engineering*, no. 2, pp. 174–176, 1985.

[27] N. Westerhof, G. Elzinga, and P. Sipkema, "An artificial arterial system for pumping hearts.," *Journal of applied physiology*, vol. 31, no. 5, pp. 776–781, 1971.

[28] F. Donovan, "Design of a hydraulic analog of the circulatory system for evaluating artificial hearts," *Biomaterials, medical devices, and artificial organs*, vol. 3, no. 4, pp. 439–449, 1975.

[29] G. M. Pantalos, S. C. Koenig, K. J. Gillars, G. A. Giridharan, and D. L. Ewert, "Characterization of an adult mock circulation for testing cardiac support devices," *ASAIO journal*, vol. 50, no. 1, pp. 37–46, 2004.

[30] M. Arabia and T. Akutsu, "A new test circulatory system for research in cardiovascular engineering," *Annals of biomedical engineering*, vol. 12, no. 1, pp. 29–48, 1984.

[31] G. Ferrari, A. W. Khir, L. Fresiello, A. Di Molfetta, and M. Kozarski, "Hybrid model analysis of intra-aortic balloon pump performance as a function of ventricular and circulatory parameters," *Artificial organs*, vol. 35, no. 9, pp. 902–911, 2011.

[32] G. M. Pantalos, C. Ionan, S. C. Koenig, *et al.*, "Expanded pediatric cardiovascular simulator for research and training," *ASAIO Journal*, vol. 56, no. 1, pp. 67–72, 2010.

[33] H. Schima, H. Baumgartner, F. Spitaler, P. Kühn, and E. Wolner, "A modular mock circulation for hydromechanical studies on valves, stenoses, vascular grafts and cardiac assist devices," *The International journal of artificial organs*, vol. 15, no. 7, pp. 417–421, 1992.

[34] D. Kikugawa, "Evaluation of cardiac function during left ventricular assist by a centrifugal blood pump," *Artificial Organs*, vol. 24, no. 8, pp. 632–635, 2000.

[35] V. Björk, F. Intonti, and A. Meissl, "A mechanical pulse duplicator for testing prosthetic mitral and aortic valves," *Thorax*, vol. 17, no. 3, p. 280, 1962.

[36] L. Scotten, D. Walker, and R. Brownlee, "Construction and evaluation of a hydromechanical simulation facility for the assessment of mitral valve prostheses," *Journal of medical engineering & technology*, vol. 3, no. 1, pp. 11–18, 1979.

[37] W. J. Kolff, "Mock circulation to test pumps designed for permanent replacement of damaged hearts," *Cleveland Clinic Quarterly*, vol. 26, pp. 223–226, 1959.

[38] B. Knierbein, H. Reul, R. Eilers, M. Lange, R. Kaufmann, and G. Rau, "Compact mock loops of the systemic and pulmonary circulation for blood pump testing," *The International journal of artificial organs*, vol. 15, no. 1, pp. 40–48, 1992.

[39] Y. Orime, S. Takatani, K. Tasai, *et al.*, "In vitro and in vivo validation tests for total artificial heart," *Artificial organs*, vol. 18, no. 1, pp. 54–72, 1994.

[40] H. A. Khalil, D. T. Kerr, M. A. Franchek, *et al.*, "Continuous flow total artificial heart: Modeling and feedback control in a mock circulatory system," *Asaio Journal*, vol. 54, no. 3, pp. 249–255, 2008.

[41] J. R. Crosby, K. J. DeCook, P. L. Tran, *et al.*, "A physical heart failure simulation system utilizing the total artificial heart and modified donovan mock circulation," *Artificial organs*, vol. 41, no. 7, E52–E65, 2017.

[42] M. Nishida, R. Kosaka, O. Maruyama, *et al.*, "Long-term durability test of axial-flow ventricular assist device under pulsatile flow," *Journal of Artificial Organs*, vol. 20, no. 1, pp. 26–33, 2017.

[43] H. Reul, B. Tesch, J. Schoenmackers, and S. Effert, "Hydromechanical simulation of systemic circulation," *Medical and biological engineering*, vol. 12, no. 4, pp. 431–436, 1974.

[44] T. G. Papaioannou, D. S. Mathioulakis, J. N. Nanas, S. G. Tsangaris, S. F. Stamatelopoulos, and S. D. Moulopoulos, "Arterial compliance is a main variable determining the effectiveness of intra-aortic balloon counterpulsation: Quantitative data from an in vitro study," *Medical engineering & physics*, vol. 24, no. 4, pp. 279–284, 2002.

[45] Y. Liu, P. Allaire, Y. Wu, H. Wood, and D. Olsen, "Construction of an artificial heart pump performance test system," *Cardiovascular Engineering*, vol. 6, no. 4, pp. 151–158, 2006.

[46] T. Sénage, D. Février, M. Michel, *et al.*, "A mock circulatory system to assess the performance of continuous-flow left ventricular assist devices (lvads): Does axial flow unload better than centrifugal lvad?" *ASAIO journal*, vol. 60, no. 2, p. 140, 2014.

[47] H. C. Love, D. L. Timms, F. Nestler, O. H. Frazier, and W. E. Cohn, "A mock circulatory loop for designing and evaluating total artificial hearts," in *2014 36th Annual International Conference of the IEEE Engineering in Medicine and Biology Society*, IEEE, 2014, pp. 5667–5670.

[48] A. Karabegovic, M. Hinteregger, C. Janeczek, *et al.*, "A systemic mock circulation for in-vitro testing of a pneumatically operated left ventricular assist device," *IFAC Proceedings Volumes*, vol. 47, no. 3, pp. 8409–8414, 2014.

[49] Y. Wu, P. E. Allaire, G. Tao, and D. Olsen, "Modeling, estimation, and control of human circulatory system with a left ventricular assist device," *IEEE transactions on control systems technology*, vol. 15, no. 4, pp. 754–767, 2007.

[50] C.-S. Jhun, J. D. Reibson, and J. P. Cysyk, "Effective ventricular unloading by left ventricular assist device varies with stage of heart failure: Cardiac simulator study," *ASAIO Journal*, vol. 57, no. 5, pp. 407–413, 2011.

[51] T. Papaioannou, D. Mathioulakis, and S. Tsangaris, "Simulation of systolic and diastolic left ventricular dysfunction in a mock circulation: The effect of arterial compliance," *Journal of medical engineering & technology*, vol. 27, no. 2, pp. 85–89, 2003.

[52] P.-L. Hsu, N. Hatam, J. Unterkofler, *et al.*, "Selective reduction of afterload in right heart assist therapy: A mock loop study," *Interactive CardioVascular and Thoracic Surgery*, vol. 19, no. 1, pp. 76–81, 2014.

[53] T. Miyamoto, D. J. Horvath, D. W. Horvath, *et al.*, "Simulated performance of the cleveland clinic continuous-flow total artificial heart using the virtual mock loop," *ASAIO journal (American Society for Artificial Internal Organs: 1992)*, vol. 65, no. 6, p. 565, 2019.

[54] F. Mouret, V. Garitey, T. Gandelheid, J. Fuseri, and R. Rieu, "A new dual activation simulator of the left heart that reproduces physiological and pathological conditions," *Medical and Biological Engineering and Computing*, vol. 38, no. 5, pp. 558–561, 2000.

[55] D. Timms, M. Hayne, K. McNeil, and A. Galbraith, "A complete mock circulation loop for the evaluation of left, right, and biventricular assist devices," *Artificial organs*, vol. 29, no. 7, pp. 564–572, 2005.

[56] D. Timms, M. Hayne, A. Tan, and M. Pearcy, "Evaluation of left ventricular assist device performance and hydraulic force in a complete mock circulation loop," *Artificial organs*, vol. 29, no. 7, pp. 573–580, 2005.

[57] Y. Wang, P. A. Smith, D. L. Timms, P.-L. Hsu, and R. A. McMahon, "Hemodynamic effects of synchronizing an intra-aortic vad in reverse-rotation control with left ventricle: A mock loop study," in *2016 38th Annual International Conference of the IEEE Engineering in Medicine and Biology Society (EMBC)*, IEEE, 2016, pp. 4300–4304.

[58] Y. Tsuboko, Y. Shiraishi, S. Matsuo, *et al.*, "Effect of right atrial contraction on prosthetic valve function in a mechanical pulmonary circulatory system," *Journal of Biomechanical Science and Engineering*, vol. 11, no. 3, pp. 15–00 356, 2016.

[59] J. Zhou, G. P. Armstrong, A. L. Medvedev, W. A. Smith, L. Golding, and J. D. Thomas, "Numeric modeling of the cardiovascular system with a left ventricular assist device.," *ASAIO journal (American Society for Artificial Internal Organs: 1992)*, vol. 45, no. 1, pp. 83–89, 1999.

[60] G. Ferrari, C. D. Lazzari, R. Mimmo, and D. A. Tosti, "Mock circulatory system for in vitro reproduction of the left ventricle, the arterial tree and their interaction with a left ventricular assist device," *Journal of medical engineering & technology*, vol. 18, no. 3, pp. 87–95, 1994.

[61] R. Zannoli, I. Corazza, and A. Branzi, "Mechanical simulator of the cardiovascular system," *Physica Medica*, vol. 25, no. 2, pp. 94–100, 2009.

[62] K. Fukamachi, A. Shiose, A. Massiello, *et al.*, "Preload sensitivity in cardiac assist devices," *The Annals of thoracic surgery*, vol. 95, no. 1, pp. 373–380, 2013.

[63] L. Baloa, J. Boston, and J. Antaki, "Elastance-based control of a mock circulatory system," *Annals of biomedical engineering*, vol. 29, no. 3, pp. 244–251, 2001.

[64] Y. Shi, T. Korakianitis, and C. Bowles, "Numerical simulation of cardiovascular dynamics with different types of vad assistance," *Journal of biomechanics*, vol. 40, no. 13, pp. 2919–2933, 2007.

[65] M. Loh and Y.-C. Yu, "Feedback control design for an elastance-based mock circulatory system," in *Proceedings of the 2004 American Control Conference*, IEEE, vol. 2, 2004, pp. 1639–1644.

[66] Y. Shi, P. V. Lawford, and D. R. Hose, "Numerical modeling of hemodynamics with pulsatile impeller pump support," *Annals of biomedical engineering*, vol. 38, no. 8, pp. 2621–2634, 2010.

[67] T. Korakianitis and Y. Shi, "Numerical simulation of cardiovascular dynamics with healthy and diseased heart valves," *Journal of biomechanics*, vol. 39, no. 11, pp. 1964–1982, 2006.

[68] K. Sagawa, *Cardiac contraction and the pressure-volume relationship*. Oxford University Press, USA, 1988.

[69] Y. Yokoyama, O. Kawaguchi, T. Shinshi, U. Steinseifer, and S. Takatani, "A new pulse duplicator with a passive fill ventricle for analysis of cardiac dynamics," *Journal of Artificial Organs*, vol. 13, no. 4, pp. 189–196, 2010.

[70] D. Burkhoff, I. Mirsky, and H. Suga, "Assessment of systolic and diastolic ventricular properties via pressure-volume analysis: A guide for clinical, translational, and basic researchers," *American Journal of Physiology-Heart and Circulatory Physiology*, vol. 289, no. 2, H501–H512, 2005.

[71] S. Vandenberghe, P. Segers, P. Steendijk, *et al.*, "Modeling ventricular function during cardiac assist: Does time-varying elastance work?" *ASAIO journal*, vol. 52, no. 1, pp. 4–8, 2006.

[72] S. C. Koenig, G. M. Pantalos, K. J. Gillars, D. L. Ewert, K. N. Litwak, and S. W. Etoch, "Hemodynamic and pressure–volume responses to continuous and pulsatile ventricular assist in an adult mock circulation," *ASAIO journal*, vol. 50, no. 1, pp. 15–24, 2004.

[73] F. M. Colacino, F. Moscato, F. Piedimonte, G. Danieli, S. Nicosia, and M. Arabia, "A modified elastance model to control mock ventricles in real-time: Numerical and experimental validation," *ASAIO journal*, vol. 54, no. 6, pp. 563–573, 2008.

[74] S. D. Gregory, M. Stevens, D. Timms, and M. Pearcy, "Replication of the frank-starling response in a mock circulation loop," in *2011 Annual International Conference of the IEEE Engineering in Medicine and Biology Society*, IEEE, 2011, pp. 6825–6828.

[75] M. Vollkron, H. Schima, L. Huber, and G. Wieselthaler, "Interaction of the cardiovascular system with an implanted rotary assist device: Simulation study with a refined computer model," *Artificial organs*, vol. 26, no. 4, pp. 349–359, 2002.

[76] D. L. Timms, S. D. Gregory, N. A. Greatrex, M. J. Pearcy, J. F. Fraser, and U. Steinseifer, "A compact mock circulation loop for the in vitro testing of cardiovascular devices," *Artificial organs*, vol. 35, no. 4, pp. 384–391, 2011.

[77] C. Kolyva, G. Biglino, J. R. Pepper, and A. W. Khir, "A mock circulatory system with physiological distribution of terminal resistance and compliance: Application for testing the intra-aortic balloon pump," *Artificial organs*, vol. 36, no. 3, E62–E70, 2012.

[78] A. W. Khir, M. J. Swalen, P. Segers, P. Verdonck, and J. R. Pepper, "Hemodynamics of a pulsatile left ventricular assist device driven by a counterpulsation pump in a mock circulation," *Artificial organs*, vol. 30, no. 4, pp. 308–312, 2006.

[79] P. G. Knoops, G. Biglino, A. D. Hughes, *et al.*, "A mock circulatory system incorporating a compliant 3d-printed anatomical model to investigate pulmonary hemodynamics," *Artificial organs*, vol. 41, no. 7, pp. 637–646, 2017.

[80] A. C. Boone, S. D. Gregory, E. L. Wu, *et al.*, "Evaluation of an intraventricular balloon pump for short-term support of patients with heart failure," *Artificial Organs*, vol. 43, no. 9, pp. 860–869, 2019.

[81] M. Laumen, T. Kaufmann, D. Timms, *et al.*, "Flow analysis of ventricular assist device inflow and outflow cannula positioning using a naturally shaped ventricle and aortic branch," *Artificial Organs*, vol. 34, no. 10, pp. 798–806, 2010.

[82] S. Gregory, D. Timms, M. Pearcy, and G. Tansley, "A naturally shaped silicone ventricle evaluated in a mock circulation loop: A preliminary study," *Journal of medical engineering & technology*, vol. 33, no. 3, pp. 185–191, 2009.

[83] K. May-Newman, N. Marquez-Maya, R. Montes, and S. Salim, "The effect of inflow cannula angle on the intraventricular flow field of the left ventricular assist device–assisted heart: An in vitro flow visualization study," *ASAIO Journal*, vol. 65, no. 2, pp. 139–147, 2019.

[84] D. Tanné, E. Bertrand, L. Kadem, P. Pibarot, and R. Rieu, "Assessment of left heart and pulmonary circulation flow dynamics by a new pulsed mock circulatory system," *Experiments in fluids*, vol. 48, no. 5, pp. 837–850, 2010.

[85] K. N. Litwak, S. C. Koenig, R. C. Cheng, G. A. Giridharan, K. J. Gillars, and G. M. Pantalos, "Ascending aorta outflow graft location and pulsatile ventricular assist provide optimal hemodynamic support in an adult mock circulation," *Artificial organs*, vol. 29, no. 8, pp. 629–635, 2005.

[86] A. Geier, A. Kunert, G. Albrecht, A. Liebold, and M. Hoenicka, "Influence of cannulation site on carotid perfusion during extracorporeal membrane oxygenation in a compliant human aortic model," *Annals of biomedical engineering*, vol. 45, no. 10, pp. 2281–2297, 2017.

[87] L. Peter, N. Noury, and M. Cerny, "The new approach for the model of cardiovascular system," *IFAC-PapersOnLine*, vol. 51, no. 6, pp. 48–53, 2018.

[88] J. Gehron, J. Zirbes, M. Bongert, *et al.*, "Development and validation of a life-sized mock circulatory loop of the human circulation for fluid-mechanical studies," *ASAIO Journal*, vol. 65, no. 8, pp. 788–797, 2019.

[89] C. Kolyva, J. R. Pepper, and A. W. Khir, "Newly shaped intra-aortic balloons improve the performance of counterpulsation at the semirecumbent position: An in vitro study," *Artificial Organs*, vol. 40, no. 8, E146–E157, 2016.

[90] I. Mueller, S.-H. Jansen-Park, M. Neidlin, *et al.*, "Design of a right ventricular mock circulation loop as a test bench for right ventricular assist devices," *Biomedical Engineering/Biomedizinische Technik*, vol. 62, no. 2, pp. 131–137, 2017.

[91] G. A. D'Souza, M. D. Taylor, and R. K. Banerjee, "Methodology for hemodynamic assessment of a three-dimensional printed patient-specific vascular test device," *Journal of Medical Devices*, vol. 13, no. 3, 2019.

[92] J. M. King, C. A. Bergeron, and C. E. Taylor, "Development of an adaptive pulmonary simulator for in vitro analysis of patient populations and patient-specific data," *Computer Methods and Programs in Biomedicine*, vol. 161, pp. 93–102, 2018.

[93] M. C. Geven, V. N. Bohté, W. H. Aarnoudse, *et al.*, "A physiologically representative in vitro model of the coronary circulation," *Physiological Measurement*, vol. 25, no. 4, p. 891, 2004.

[94] C. De Lazzari, M. Darowski, G. Ferrari, D. M. Pisanelli, and G. Tosti, "Modelling in the study of interaction of hemopump device and artificial ventilation," *Computers in biology and medicine*, vol. 36, no. 11, pp. 1235–1251, 2006.

[95] G. A. Giridharan, D. L. Ewert, G. M. Pantalos, *et al.*, "Left ventricular and myocardial perfusion responses to volume unloading and afterload reduction in a computer simulation," *ASAIO journal*, vol. 50, no. 5, pp. 512–518, 2004.

[96] M. Rezaienia, G. Paul, E. Avital, S. Mozafari, M. Rothman, and T. Korakianitis, "In-vitro investigation of the hemodynamic responses of the cerebral, coronary and renal circulations with a rotary blood pump installed in the descending aorta," *Medical engineering & physics*, vol. 40, pp. 2–10, 2017.

[97] P.-L. Hsu, J. Bruch, and R. McMahon, "A controller for a miniature intra-aortic ventricular assist device," *Artificial Organs*, vol. 35, no. 3, pp. 282–287, 2011.

[98] S. D. Gregory, J. P. Pauls, E. L. Wu, *et al.*, "An advanced mock circulation loop for in vitro cardiovascular device evaluation," *Artificial Organs*, vol. 44, no. 6, E238–E250, 2020.

[99] W. D. Clark, B. A. Eslahpazir, I. R. Argueta-Morales, A. J. Kassab, E. A. Divo, and W. M. DeCampli, "Comparison between bench-top and computational modelling of cerebral thromboembolism in ventricular assist device circulation," *Cardiovascular engineering and technology*, vol. 6, no. 3, pp. 242–255, 2015.

[100] S. Bozkurt, "Effect of cerebral flow autoregulation function on cerebral flow rate under continuous flow left ventricular assist device support," *Artificial Organs*, vol. 42, no. 8, pp. 800–813, 2018.

[101] G. Ferrari, M. Kozarski, C. De Lazzari, *et al.*, "A hybrid (numerical-physical) model of the left ventricle," *The International journal of artificial organs*, vol. 24, no. 7, pp. 456–462, 2001.

[102] M. Kozarski, G. Ferrari, F. Clemente, *et al.*, "A hybrid mock circulatory system: Development and testing of an electro-hydraulic impedance simulator," *The International Journal of artificial organs*, vol. 26, no. 1, pp. 53–63, 2003.

[103] G. Ferrari, M. Kozarski, C. De Lazzari, *et al.*, "Modelling of cardiovascular system: Development of a hybrid (numerical-physical) model," *The International Journal of Artificial Organs*, vol. 26, no. 12, pp. 1104–1114, 2003.

[104] G. Ferrari, C. De Lazzari, M. Kozarski, *et al.*, "A hybrid mock circulatory system: Testing a prototype under physiologic and pathological conditions," *ASAIO journal*, vol. 48, no. 5, pp. 487–494, 2002.

[105] K.-W. Gwak, "Design and evaluation of cardiovascular impedance simulator considering mechanical limits," *Journal of the Korean Society for Precision Engineering*, vol. 25, no. 1, pp. 151–159, 2008.

[106] G. Ochsner, R. Amacher, A. Amstutz, *et al.*, "A novel interface for hybrid mock circulations to evaluate ventricular assist devices," *IEEE transactions on biomedical engineering*, vol. 60, no. 2, pp. 507–516, 2012.

[107] F. Nestler, A. P. Bradley, S. J. Wilson, D. L. Timms, O. H. Frazier, and W. E. Cohn, "A hybrid mock circulation loop for a total artificial heart," *Artificial organs*, vol. 38, no. 9, pp. 775–782, 2014.

[108] C. L. Felipini, A. J. P. De Andrade, J. C. Lucchi, J. W. G. Da Fonseca, and D. Nicolosi, "An electro-fluid-dynamic simulator for the cardiovascular system," *Artificial Organs*, vol. 32, no. 4, pp. 349–354, 2008.

[109] D. Telyshev, A. Pugovkin, S. Selishchev, D. Rüschen, and S. Leonhardt, "Hybrid mock circulatory loop for training and study purposes," in *2018 Ural Symposium on Biomedical Engineering, Radioelectronics and Information Technology (USBEREIT)*, IEEE, 2018, pp. 29–32.

[110] E. Mirzaei, M. Farahmand, and E. Kung, "An algorithm for coupling multibranch in vitro experiment to numerical physiology simulation for a hybrid cardiovascular model," *International Journal for Numerical Methods in Biomedical Engineering*, vol. 36, no. 3, e3289, 2020.

[111] B. Hanson, M. Levesley, K. Watterson, and P. Walker, "Hardware-in-the-loop-simulation of the cardiovascular system, with assist device testing application," *Medical engineering & physics*, vol. 29, no. 3, pp. 367–374, 2007.

[112] A. Alazmani, D. G. Keeling, P. G. Walker, *et al.*, "Introducing a hardware-in-the-loop simulation of the cardiovascular system," in *2012 4th IEEE RAS & EMBS International Conference on Biomedical Robotics and Biomechatronics (BioRob)*, IEEE, 2012, pp. 153–158.

[113] A. Urbaszek and M. Schaldach, *Bio-fluid mechanics*. Computational mechanics, 1995, vol. 3, pp. 129–160.

[114] M. Darowski, M. Kozarski, G. Ferrari, *et al.*, "A new hybrid (hydro-numerical) model of the circulatory system," *Bulletin of the Polish Academy of Sciences. Technical Sciences*, vol. 61, no. 4, 2013.

[115] G. Ferrari, M. Kozarski, C. De Lazzari, K. G. Ska, G. Tosti, and M. Darowski, "Development of a hybrid (numerical-hydraulic) circulatory model: Prototype testing and its response to iabp assistance," *The International journal of artificial organs*, vol. 28, no. 7, pp. 750–759, 2005.

[116] L. Fresiello, A. W. Khir, A. Di Molfetta, M. Kozarski, and G. Ferrari, "Effects of intra-aortic balloon pump timing on baroreflex activities in a closed-loop cardiovascular hybrid model," *Artificial organs*, vol. 37, no. 3, pp. 237–247, 2013.

[117] M. Ursino, M. Giulioni, and C. A. Lodi, "Relationships among cerebral perfusion pressure, autoregulation, and transcranial doppler waveform: A modeling study," *Journal of neurosurgery*, vol. 89, no. 2, pp. 255–266, 1998.

[118] E. Cuenca-Navalon, T. Finocchiaro, M. Laumen, A. Fritschi, T. Schmitz-Rode, and U. Steinseifer, "Design and evaluation of a hybrid mock circulatory loop for total artificial heart testing," *The International journal of artificial organs*, vol. 37, no. 1, pp. 71–80, 2014.

[119] M. Ursino, M. Antonucci, and E. Belardinelli, "Role of active changes in venous capacity by the carotid baroreflex: Analysis with a mathematical model," *American Journal of Physiology-Heart and Circulatory Physiology*, vol. 267, no. 6, H2531–H2546, 1994.

[120] S. Mushi and Y.-C. Yu, "Control of a mock circulatory system to simulate the short-term baroreflex," in *2008 American Control Conference*, IEEE, 2008, pp. 844–849.

[121] S.-H. Jansen-Park, M. N. Mahmood, I. Müller, *et al.*, "Effects of interaction between ventricular assist device assistance and autoregulated mock circulation including frank–starling mechanism and baroreflex," *Artificial Organs*, vol. 40, no. 10, pp. 981–991, 2016.

[122] M. Vaes, M. Rutten, R. van de Molengraft, and F. van de Vosse, "Left ventricular assist device evaluation with a model-controlled mock circulation," in *Summer Bioengineering Conference*, American Society of Mechanical Engineers, vol. 47985, 2007, pp. 723–724.

[123] A. M. Van Roon, L. J. Mulder, M. Althaus, and G. Mulder, "Introducing a baroreflex model for studying cardiovascular effects of mental workload," *Psychophysiology*, vol. 41, no. 6, pp. 961–981, 2004.

[124] S. Bozkurt and K. K. Safak, "Evaluating the hemodynamical response of a cardiovascular system under support of a continuous flow left ventricular assist device via numerical modeling and simulations," *Computational and Mathematical Methods in Medicine*, vol. 2013, 2013.

[125] J. Bonnemain, A. C. I. Malossi, M. Lesinigo, S. Deparis, A. Quarteroni, and L. K. von Segesser, "Numerical simulation of left ventricular assist device implantations: Comparing the ascending and the descending aorta cannulations," *Medical engineering & physics*, vol. 35, no. 10, pp. 1465–1475, 2013.

[126] Y. Wu, P. Allaire, G. Tao, H. Wood, D. Olsen, and C. Tribble, "An advanced physiological controller design for a left ventricular assist device to prevent left ventricular collapse," *Artificial organs*, vol. 27, no. 10, pp. 926–930, 2003.

[127] A. Petrou, M. Granegger, M. Meboldt, and M. S. Daners, "A versatile hybrid mock circulation for hydraulic investigations of active and passive cardiovascular implants," *Asaio Journal*, vol. 65, no. 5, p. 495, 2019.

[128] T. G. Papaioannou, D. S. Mathioulakis, K. S. Stamatelopoulos, *et al.*, "New aspects on the role of blood pressure and arterial stiffness in mechanical assistance by intra-aortic balloon pump: In-vitro data and their application in clinical practice," *Artificial organs*, vol. 28, no. 8, pp. 717–727, 2004.

[129] L. Fresiello, K. Zieliński, S. Jacobs, *et al.*, "Reproduction of continuous flow left ventricular assist device experimental data by means of a hybrid cardiovascular model with baroreflex control," *Artificial organs*, vol. 38, no. 6, pp. 456–468, 2014.

[130] N. Yuan, G. J. Arnaoutakis, T. J. George, *et al.*, "The spectrum of complications following left ventricular assist device placement," *Journal of cardiac surgery*, vol. 27, no. 5, pp. 630–638, 2012.

[131] F. Nestler, D. L. Timms, M. Stevens, *et al.*, "Investigation of the inherent left-right flow balancing of rotary total artificial hearts by means of a resistance box," *Artificial Organs*, vol. 44, no. 6, pp. 584–593, 2020.

[132] J. Tsay, D. Pinkhas, B. C. Lee, *et al.*, "Worsening renal function in cardiac mechanical support," *Heart, Lung and Circulation*, vol. 29, no. 8, pp. 1247–1255, 2020.

[133] Y. Wang, P. A. Smith, P. De-Sciscio, *et al.*, "Replication of pressure-volume loop with controllable espvr and edpvr curves on a personalized mock circulatory loop based on elastance function," in *2017 39th Annual International Conference of the IEEE Engineering in Medicine and Biology Society (EMBC)*, IEEE, 2017, pp. 1282–1286.

[134] J. R. Gohean, M. J. George, K.-W. Chang, *et al.*, "Preservation of native aortic valve flow and full hemodynamic support with the torvad™ using a computational model of the cardiovascular system," *ASAIO journal (American Society for Artificial Internal Organs: 1992)*, vol. 61, no. 3, p. 259, 2015.

[135] F. Huang, X. Ruan, J. Zou, W. Qian, and X. Fu, "A fast building and effective hydraulic pediatric mock circulatory system for the evaluation of a left ventricular assist device," *ASAIO journal*, vol. 59, no. 6, pp. 575–585, 2013.

[136] Y.-C. Yu and S. Gopalakrishnan, "Elastance control of a mock circulatory system for ventricular assist device test," in *2009 American Control Conference*, IEEE, 2009, pp. 1009–1014.

[137] S. Schampaert, K. Pennings, M. Van de Molengraft, N. Pijls, F. Van de Vosse, and M. Rutten, "A mock circulation model for cardiovascular device evaluation," *Physiological measurement*, vol. 35, no. 4, p. 687, 2014.

[138] G. Kissas, Y. Yang, E. Hwuang, W. R. Witschey, J. A. Detre, and P. Perdikaris, "Machine learning in cardiovascular flows modeling: Predicting arterial blood pressure from non-invasive 4d flow mri data using physics-informed neural networks," *Computer Methods in Applied Mechanics and Engineering*, vol. 358, p. 112 623, 2020.

[139] T. Li, H. Li, W. Cui, N. Xie, X. Li, and Y. Wang, "Design and intelligent control of mock circulation system to reproduce patient-specific physiological indexes," *Biomedical Signal Processing and Control*, vol. 78, p. 103 987, 2022.

[140] C. E. Taylor and G. E. Miller, "Mock circulatory loop compliance chamber employing a novel real-time control process," *Journal of medical devices*, vol. 6, no. 4, 2012.

[141] C. E. Taylor and G. E. Miller, "Implementation of an automated peripheral resistance device in a mock circulatory loop with characterization of performance values using simulink simscape and parameter estimation," *Journal of Medical Devices*, vol. 6, no. 4, 2012.

[142] H. Suga, K. Sagawa, and A. A. Shoukas, "Load independence of the instantaneous pressure-volume ratio of the canine left ventricle and effects of epinephrine and heart rate on the ratio," *Circulation research*, vol. 32, no. 3, pp. 314–322, 1973.

[143] N. Herring and D. J. Paterson, *Levick's introduction to cardiovascular physiology*. CRC Press, 2018.

[144] K. Sagawa, H. Suga, A. A. Shoukas, and K. M. Bakalar, "End-systolic pressure/volume ratio: A new index of ventricular contractility," *The American journal of cardiology*, vol. 40, no. 5, pp. 748–753, 1977.

[145] S. Frolov, S. Sindeev, V. Lischouk, D. S. Gazizova, D. Liepsch, and A. Balasso, "A lumped parameter model of cardiovascular system with pulsating heart for diagnostic studies," *Journal of Mechanics in Medicine and Biology*, vol. 17, no. 03, p. 1 750 056, 2017.

[146] M. W. Chapleau and F. M. Abboud, "Contrasting effects of static and pulsatile pressure on carotid baroreceptor activity in dogs.," *Circulation Research*, vol. 61, no. 5, pp. 648–658, 1987.

[147] W. Wang, M. Brandle, and I. H. Zucker, "Influence of vagotomy on the baroreflex sensitivity in anesthetized dogs with experimental heart failure," *American Journal of Physiology-Heart and Circulatory Physiology*, vol. 265, no. 4, H1310–H1317, 1993.

[148] P. Parker, B. Celler, E. K. Potter, and D. McCloskey, "Vagal stimulation and cardiac slowing," *Journal of the autonomic nervous system*, vol. 11, no. 2, pp. 226–231, 1984.

[149] E. Schulz, M. Speekenbrink, and A. Krause, "A tutorial on gaussian process regression: Modelling, exploring, and exploiting functions," *Journal of Mathematical Psychology*, vol. 85, pp. 1–16, 2018.

[150] W. Wagner and A. Pruß, "The iapws formulation 1995 for the thermodynamic properties of ordinary water substance for general and scientific use," *Journal of physical and chemical reference data*, vol. 31, no. 2, pp. 387–535, 2002.

[151] "Esao abstract book," *The International Journal of Artificial Organs*, vol. 45, no. 9, pp. 729–796, 2022.

[152] C. Lewin, *Mathematics of motion control profiles*, Accessed on August 9, 2023. [Online]. Available: https://www.pmdcorp.com/resources/type/articles/get/mathematics-of-motion-control-profiles-article.

[153] Y. Dabiri, A. Van der Velden, K. L. Sack, J. S. Choy, G. S. Kassab, and J. M. Guccione, "Prediction of left ventricular mechanics using machine learning," *Frontiers in physics*, vol. 7, p. 117, 2019.

[154] S. Darvishi, H. Behnam, M. Pouladian, and N. Samiei, "Measuring left ventricular volumes in two-dimensional echocardiography image sequence using level-set method for automatic detection of end-diastole and end-systole frames," *Research in Cardiovascular Medicine*, vol. 2, no. 1, p. 39, 2013.

[155] T. Shiga, T. Kuroda, Y. Tsuboko, H. Miura, Y. Shiraishi, and T. Yambe, "Hemodynamic effects of pressure-volume relation in the atrial contraction model on the total artificial heart using centrifugal blood pumps," in *2013 35th Annual International Conference of the IEEE Engineering in Medicine and Biology Society (EMBC)*, IEEE, 2013, pp. 1815–1818.

[156] M. Maleki, A. Alizadehasl, and M. Haghjoo, *Practical Cardiology: Principles and Approaches*. Elsevier, 2021, ISBN: 9780323809153.

[157] "Abstract esao 2021," *The International Journal of Artificial Organs*, vol. 44, no. 9, pp. 592–638, 2021.

[158] D. Legendre, J. Fonseca, A. Andrade, *et al.*, "Mock circulatory system for the evaluation of left ventricular assist devices, endoluminal prostheses, and vascular diseases," *Artificial organs*, vol. 32, no. 6, pp. 461–467, 2008.

[159] "Abstract esao 2023," *The International Journal of Artificial Organs*, vol. 46, no. 7, pp. 440–441, 2023.

[160] J. B. Mark, *Atlas of cardiovascular monitoring*. Churchill Livingstone, 1998.

[161] W. Rascher, R. Lang, M. Taubitz, *et al.*, "Vasopressin-induced increase in total peripheral resistance in deoxycorticosterone acetate hypertensive rats is buffered by the baroreceptor reflex.," *Clinical Science (London, England: 1979)*, vol. 61, 153s–156s, 1981.

[162] R. Burattini and P. Borgdorff, "Closed-loop baroreflex control of total peripheral resistance in the cat: Identification of gains by aid of a model," *Cardiovascular research*, vol. 18, no. 12, pp. 715–723, 1984.

[163] "Implants for surgery — active implantable medical devices, part 5: Circulatory support devices," BSI, UK, Standard, Jul. 2022.

[164] S. Clay, K. Alfakih, A. Radjenovic, T. Jones, and J. P. Ridgway, "Normal range of human left ventricular volumes and mass using steady state free precession mri in the radial long axis orientation," *Magnetic Resonance Materials in Physics, Biology and Medicine*, vol. 19, pp. 41–45, 2006.

[165] M. C. Brindise, M. M. Busse, and P. P. Vlachos, "Density-and viscosity-matched newtonian and non-newtonian blood-analog solutions with pdms refractive index," *Experiments in fluids*, vol. 59, pp. 1–8, 2018.

Appendix A

Simulink: Cardiovascular Model with Baroreflex Response

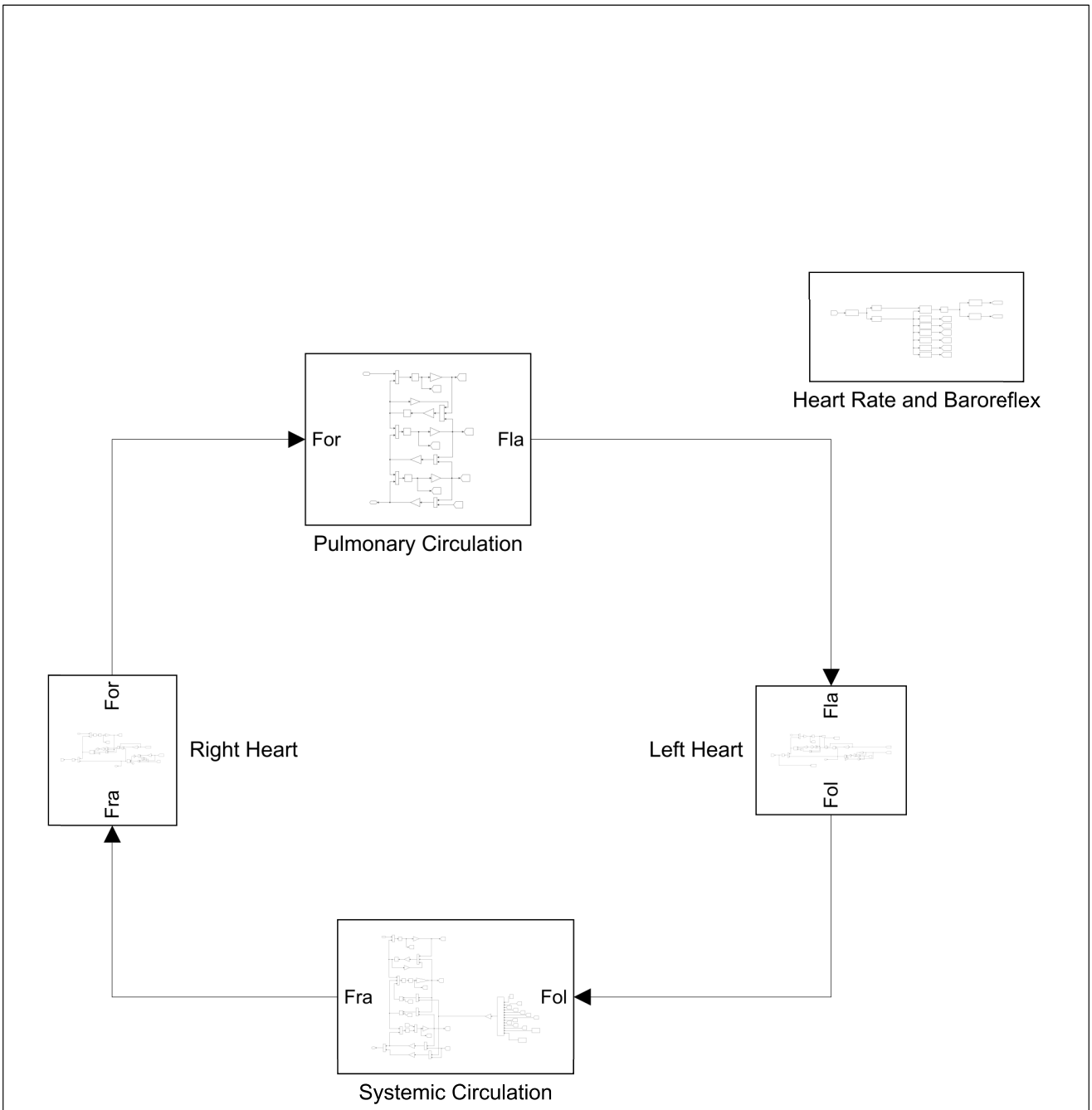

V2_Baroreflexmodel_2021a

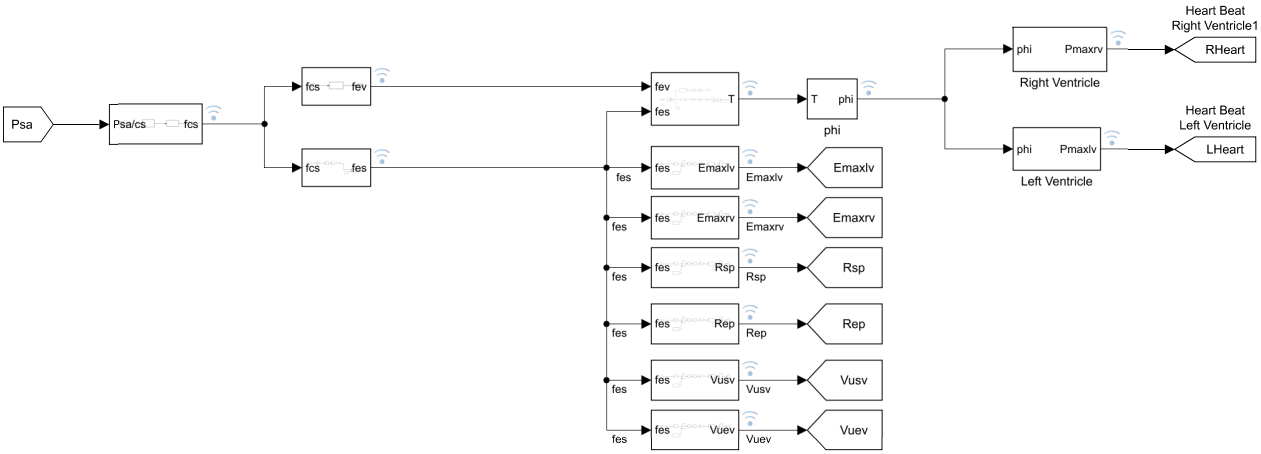

Heart Rate and Baroreflex

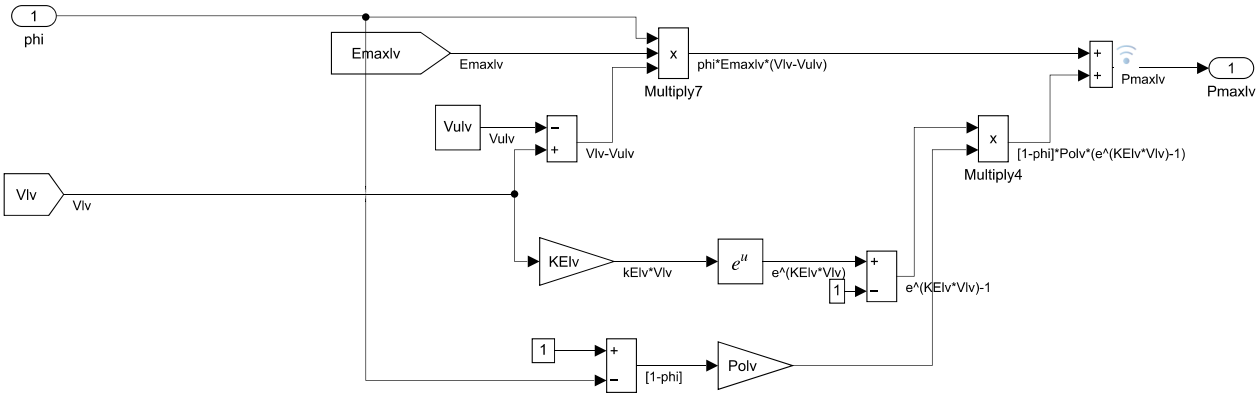

Left Ventricle

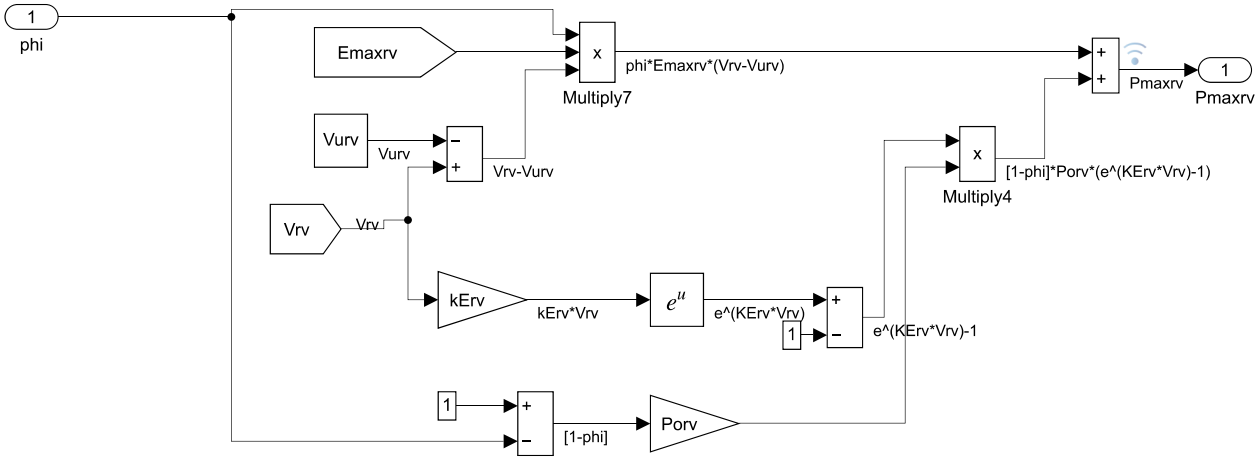

Right Ventricle

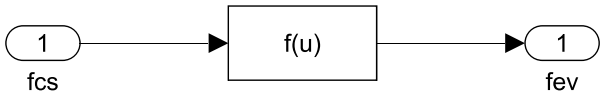

Subsystem1

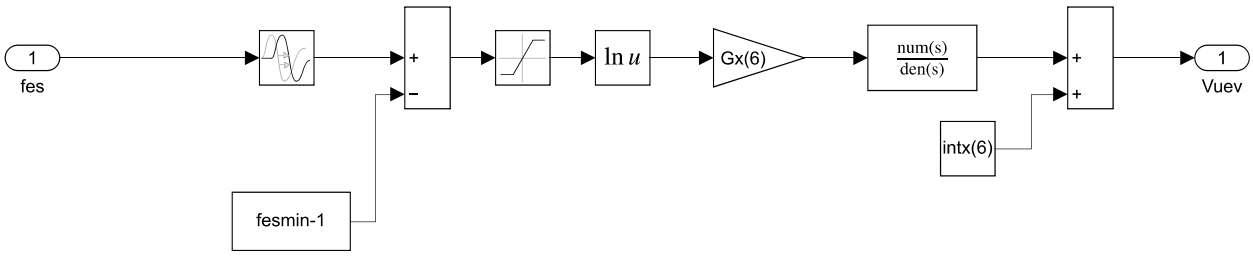

Subsystem10

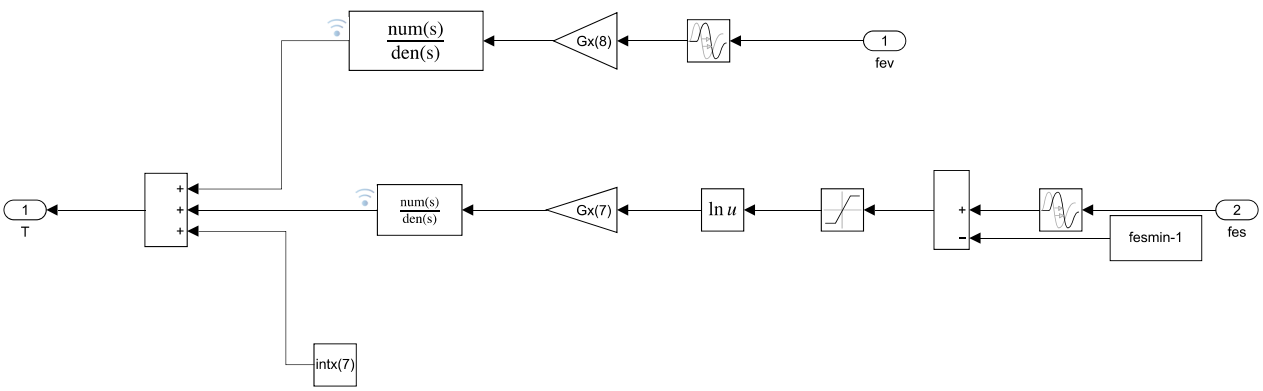

Subsystem13

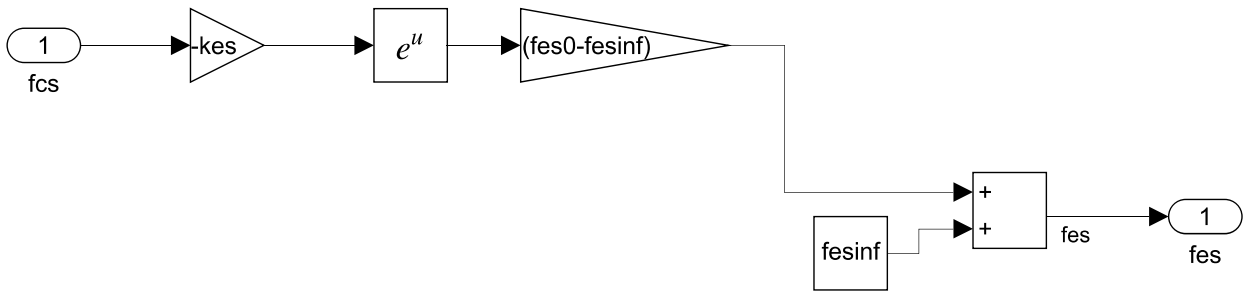

Subsystem2

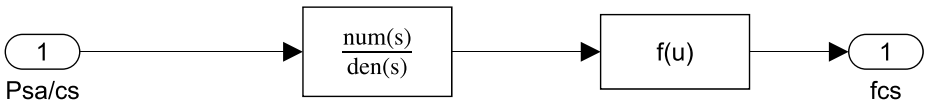

Subsystem4

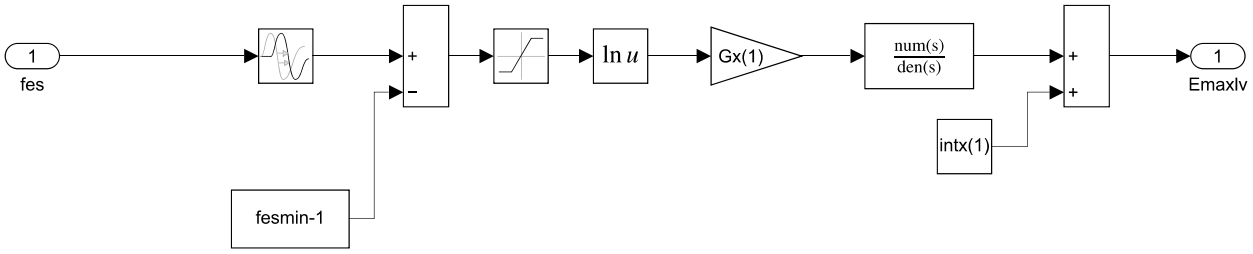

Subsystem5

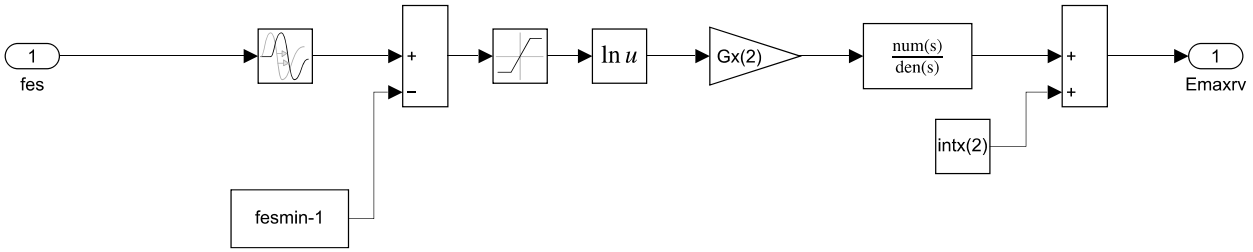

Subsystem6

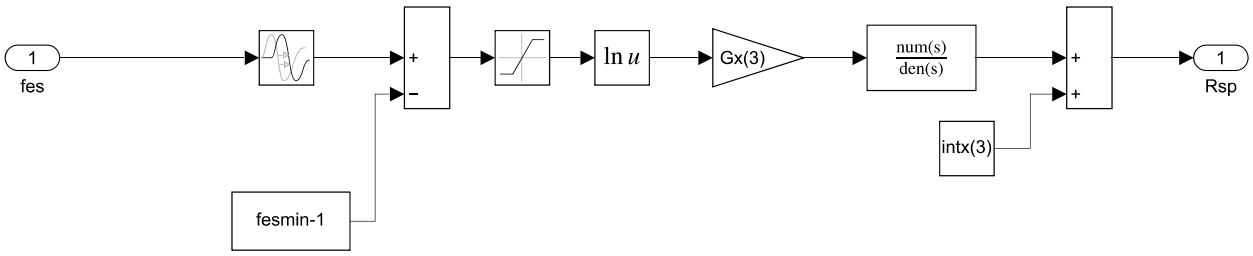

Subsystem7

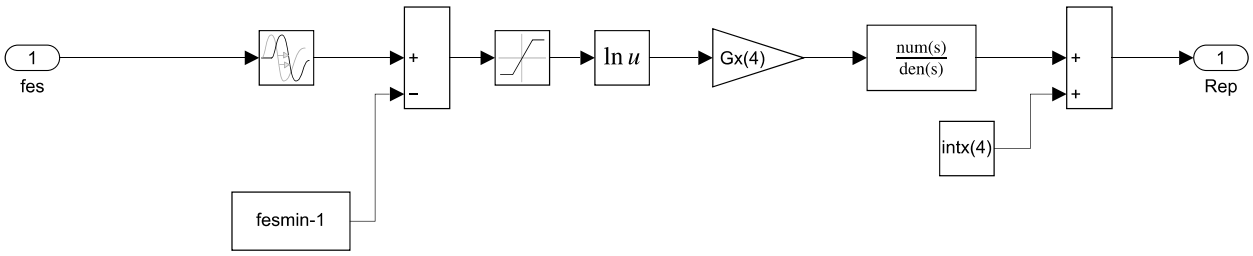

Subsystem8

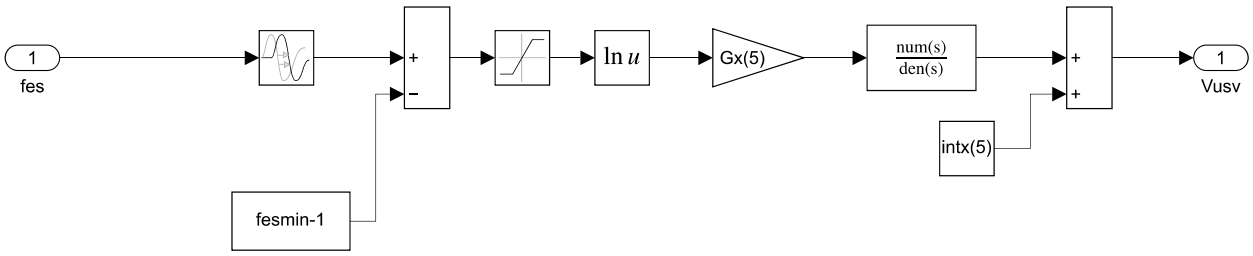

Subsystem9

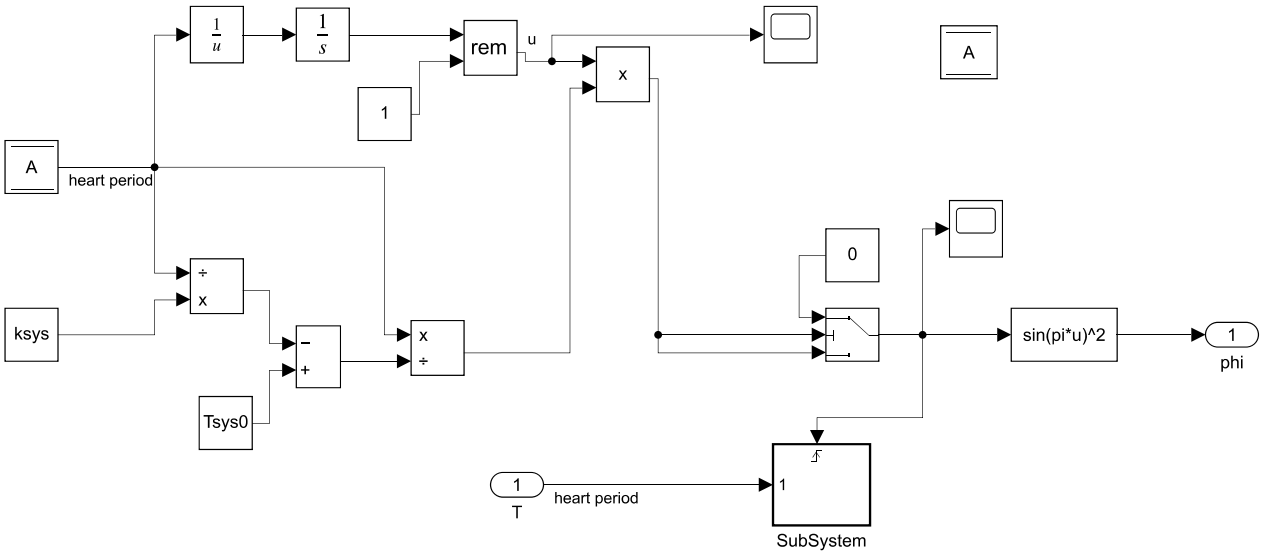
1/u
1/s
rem
u
1
x
A
heart period
÷
x
ksys
−
+
Tsys0
x
÷
0
sin(pi*u)^2
1
phi
1
T
heart period
1
SubSystem

phi

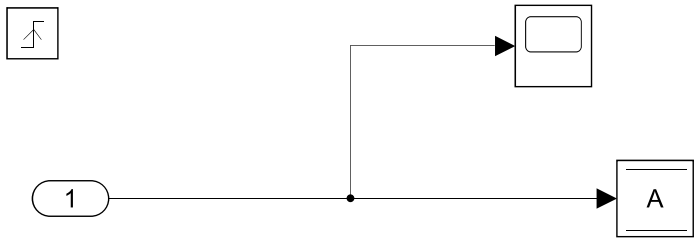

SubSystem

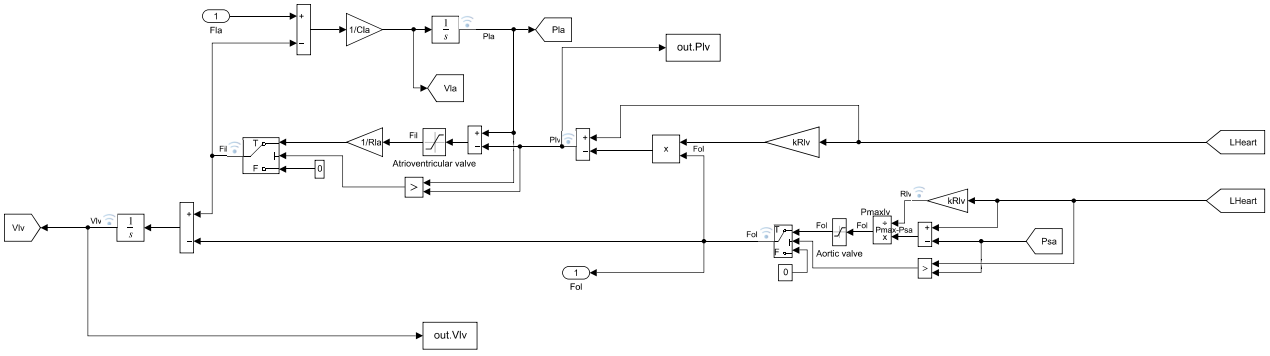
1
Fla
1/Cla
Pla
Vla
out.Plv
Fil
1/Rla
Fil
Atrioventricular valve
Plv
x
Fol
kRlv
LHeart
Vlv
Vlv
Rlv
kRlv
LHeart
Pmaxlv
Fol
Fol
Fol
Pmax
Psa
Psa
Aortic valve
1
Fol
out.Vlv

Left Heart

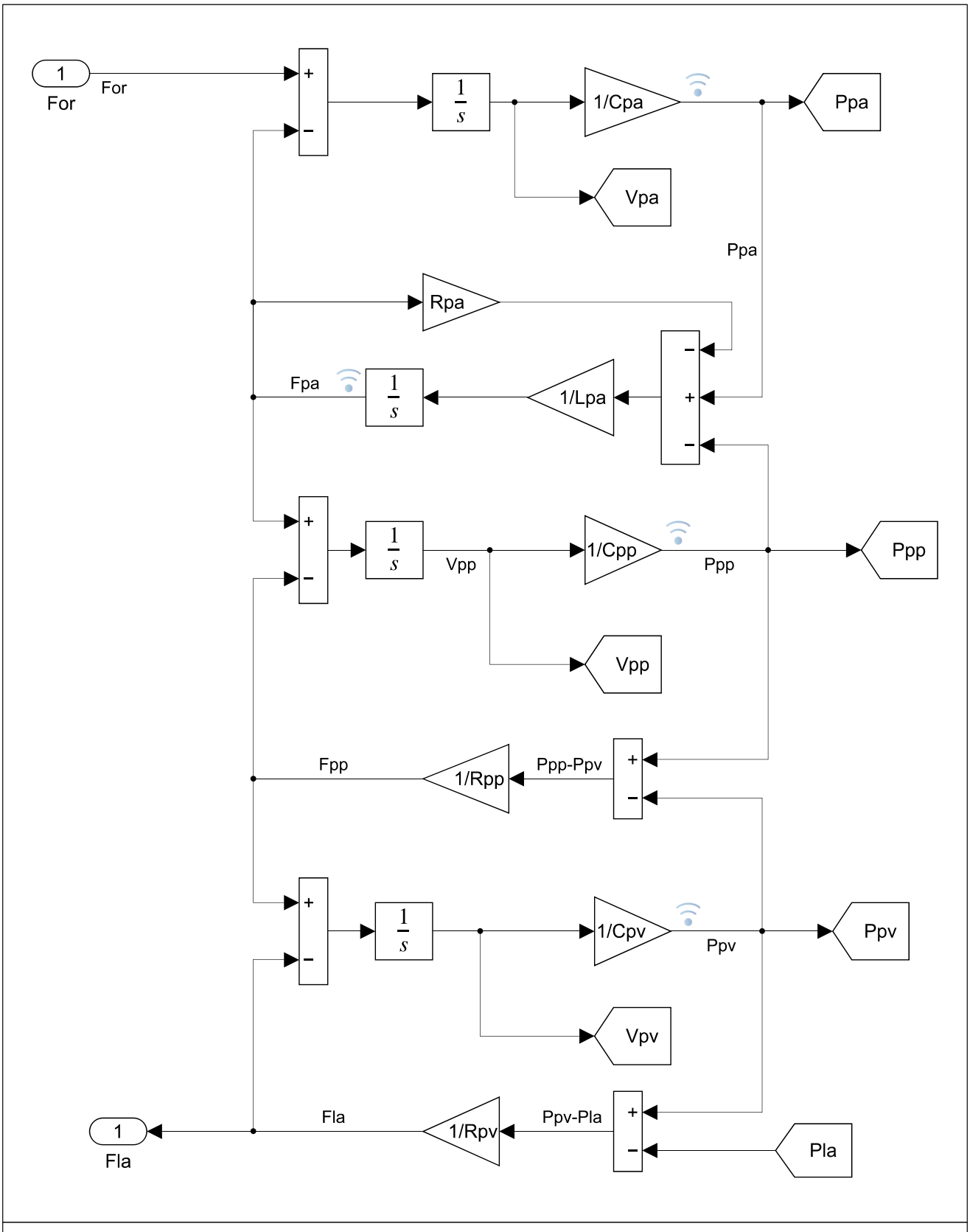

Pulmonary Circulation

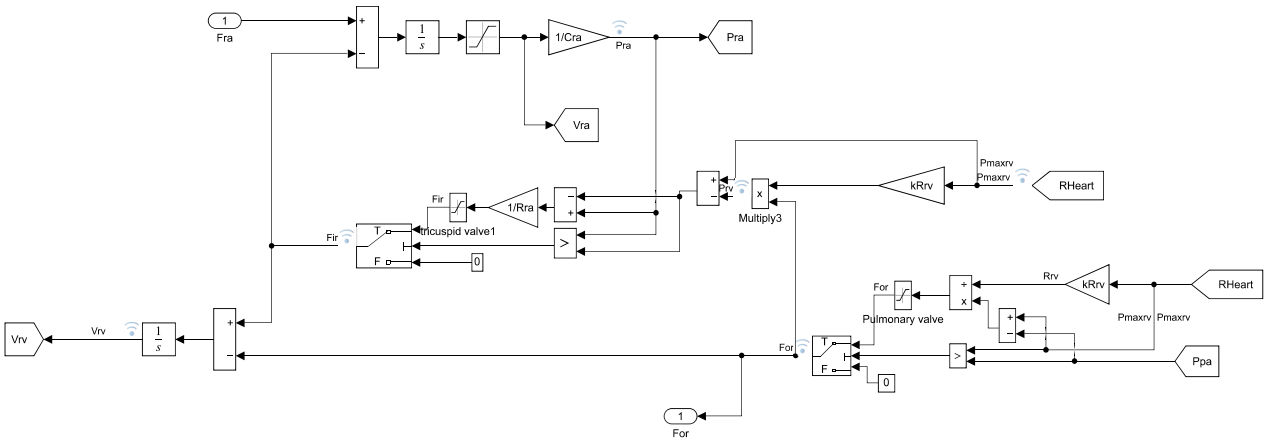
1
Fra
1/Cra
Pra
Vra
Pmaxrv
Pmaxrv
RHeart
kRrv
Prv
Multiply3
Fir
1/Rra
Fir
tricuspid valve1
T
F
0
Rrv
kRrv
RHeart
For
Pulmonary valve
Pmaxrv
Pmaxrv
Ppa
Vrv
Vrv
For
T
F
0
1
For

Right Heart

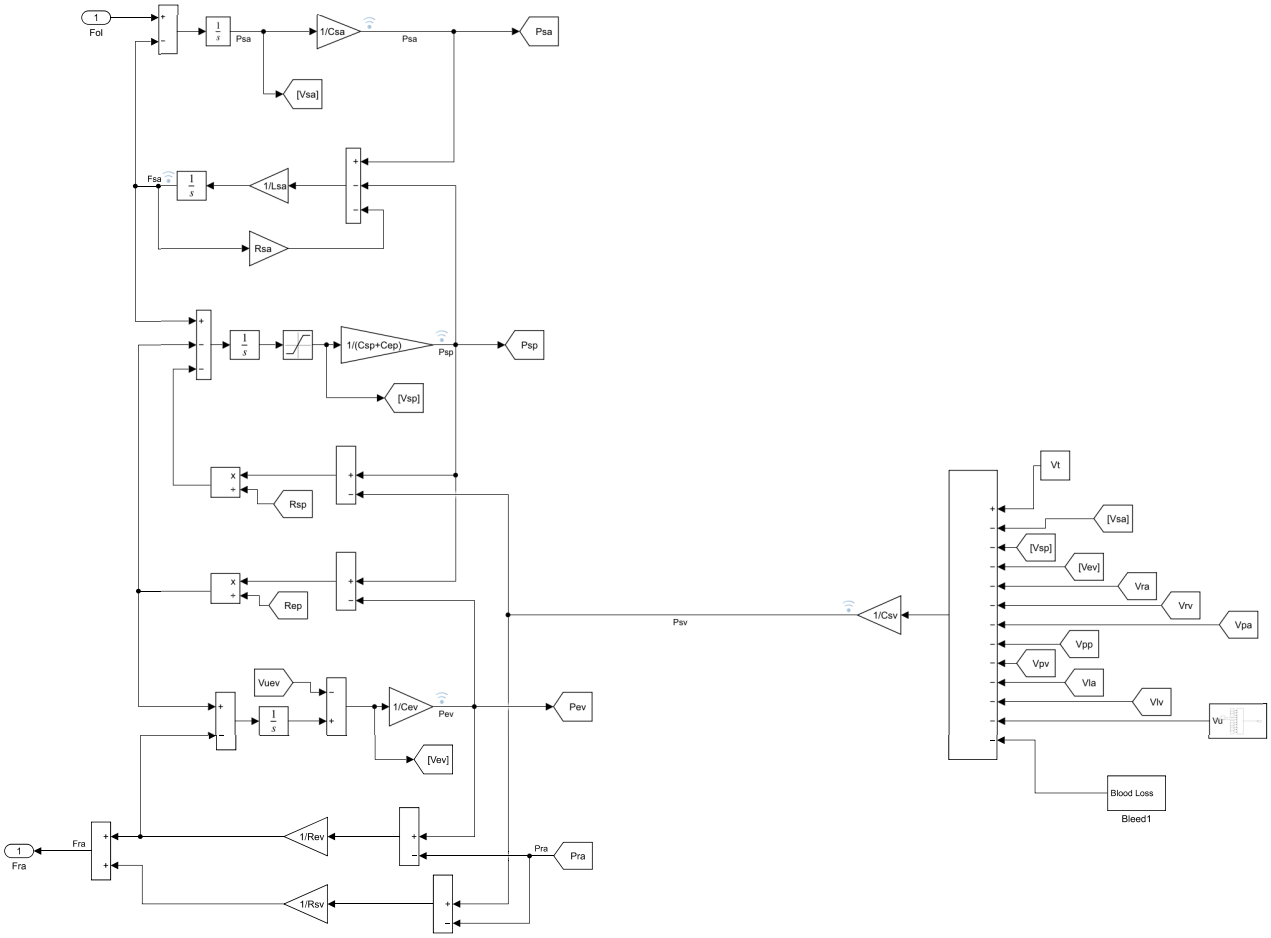

Systemic Circulation

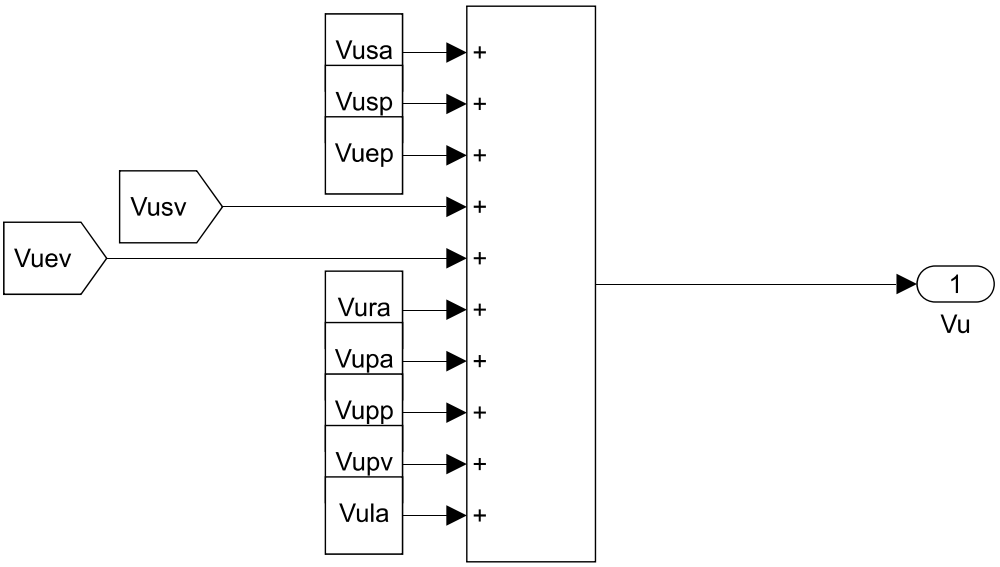

Subsystem6

Appendix B

LabVIEW: The Baroreflex Model

1. Solve for the controlled parameter the output of the static function

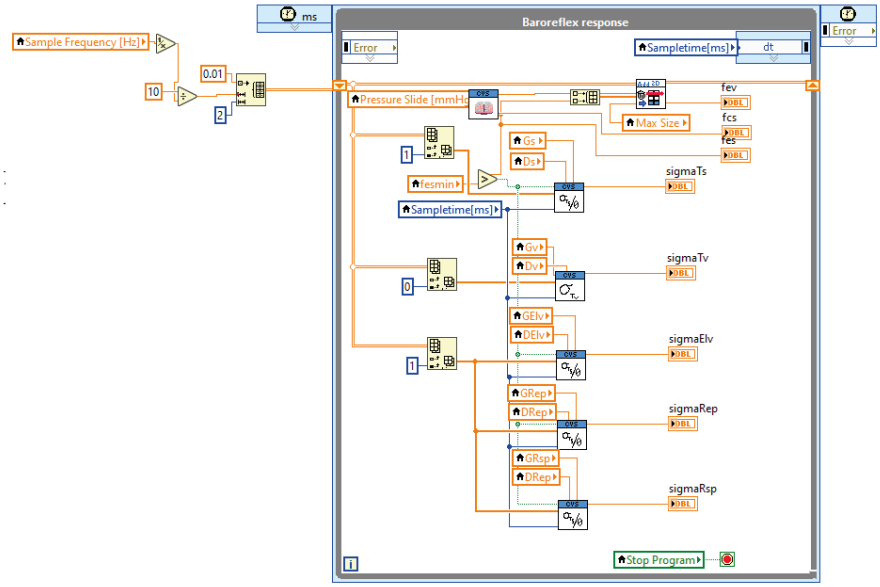

2. Solve transfer functions of thebaroroeflex

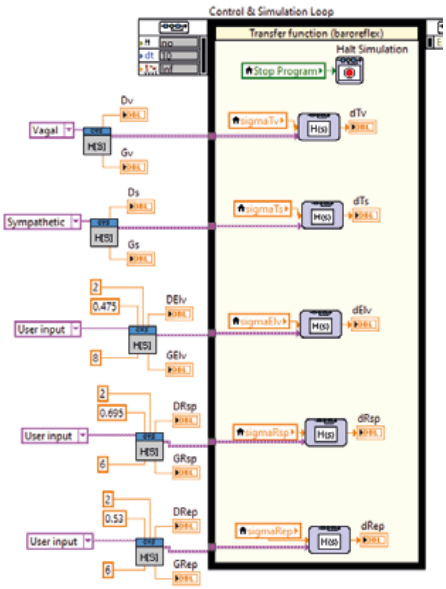

3. Calculate the variable change

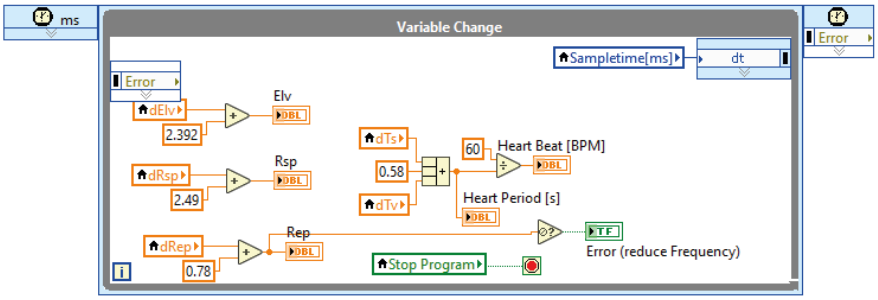

Appendix C

LabVIEW: the Left Ventricle Simulator

1. Initialise the Linear Motor

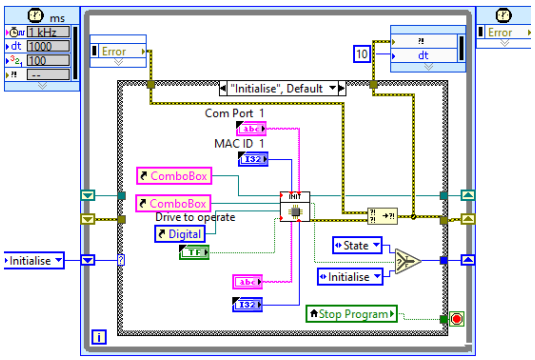

2. Homing of the Linear Motor

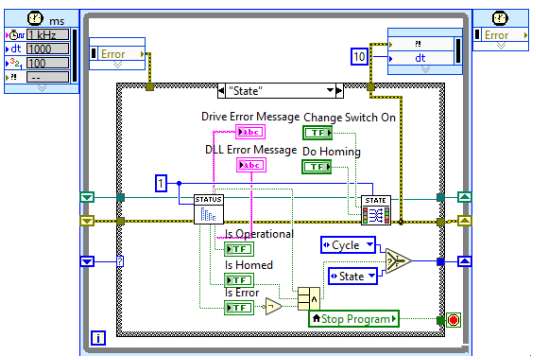

3. Cycle Motion of the Linear Motor

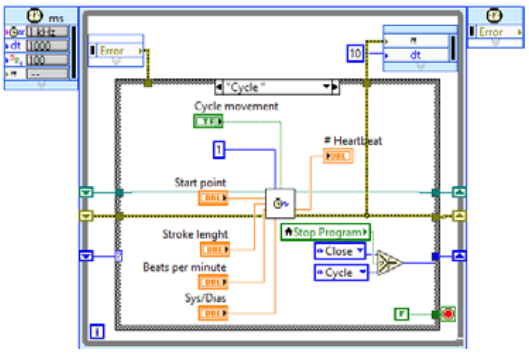

4. Disconnect the Linear Motor

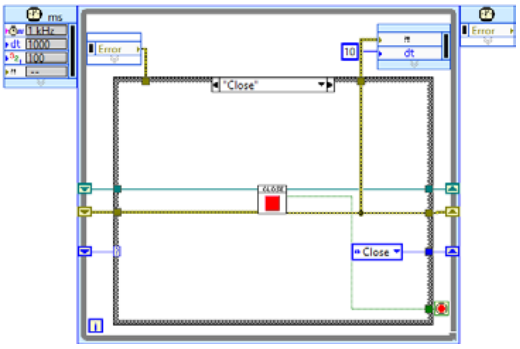

Sub VI: Cycle Motion

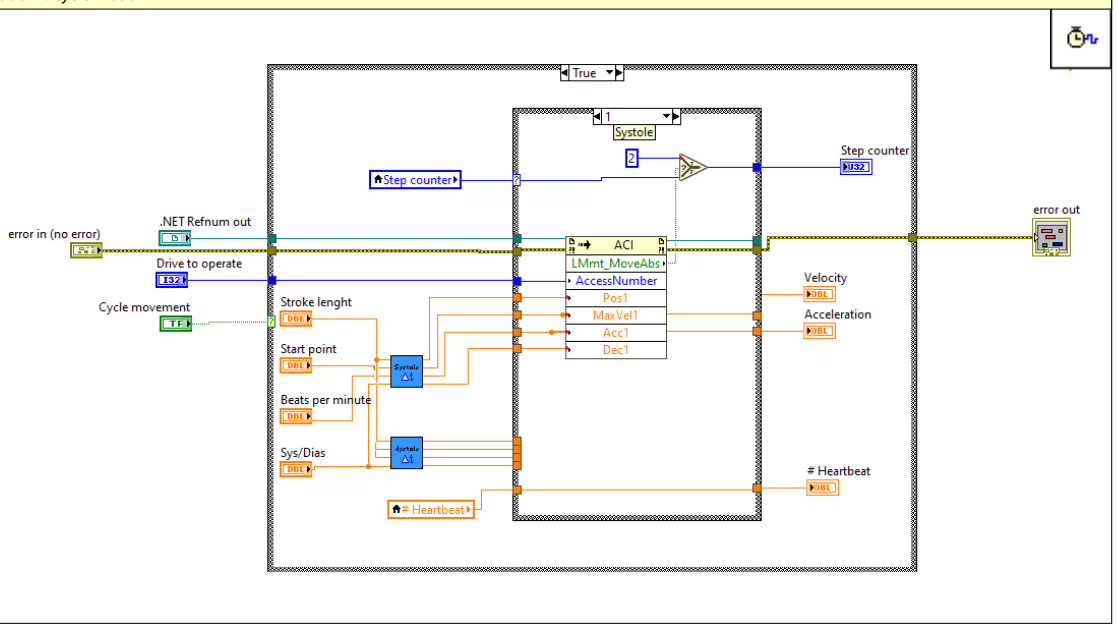

Sub VI: Cycle Motion: Case Structure

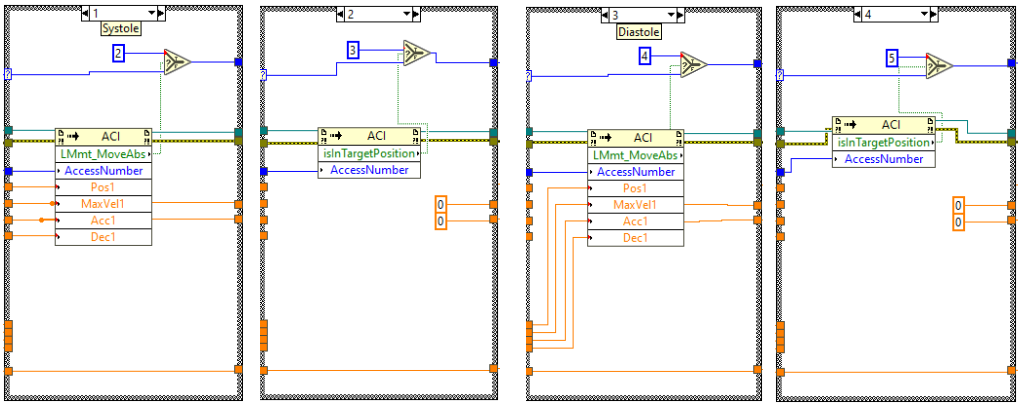

Sub VI: Cycle Motion: Systolic Calculations

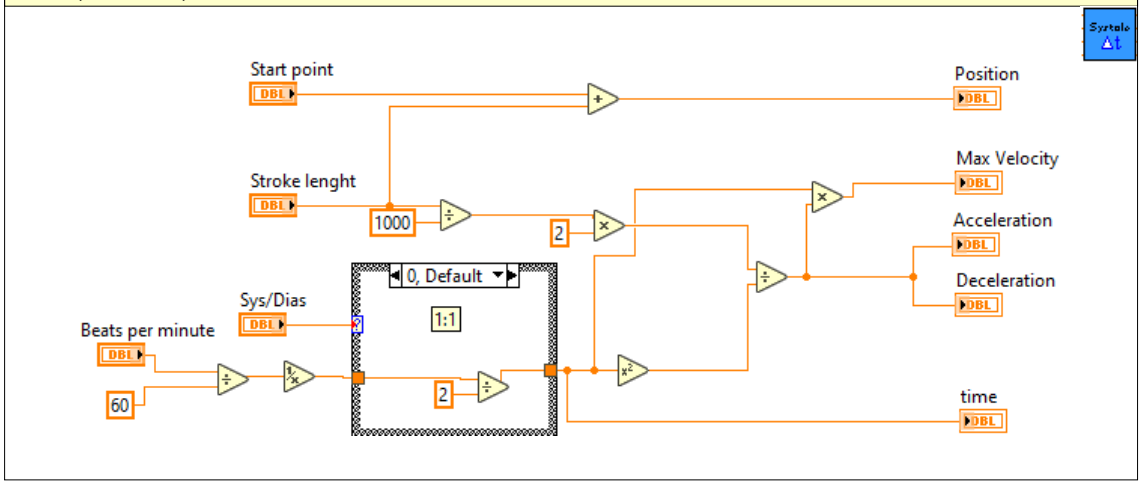

Sub VI: Cycle Motion: Diastollic Calculations

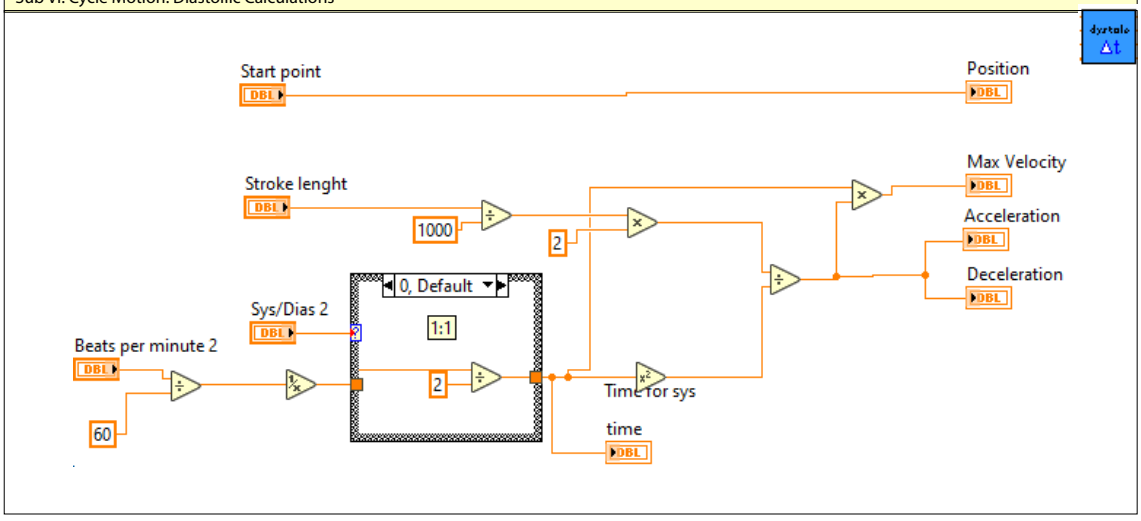

Appendix D

Technical drawing of the resistor

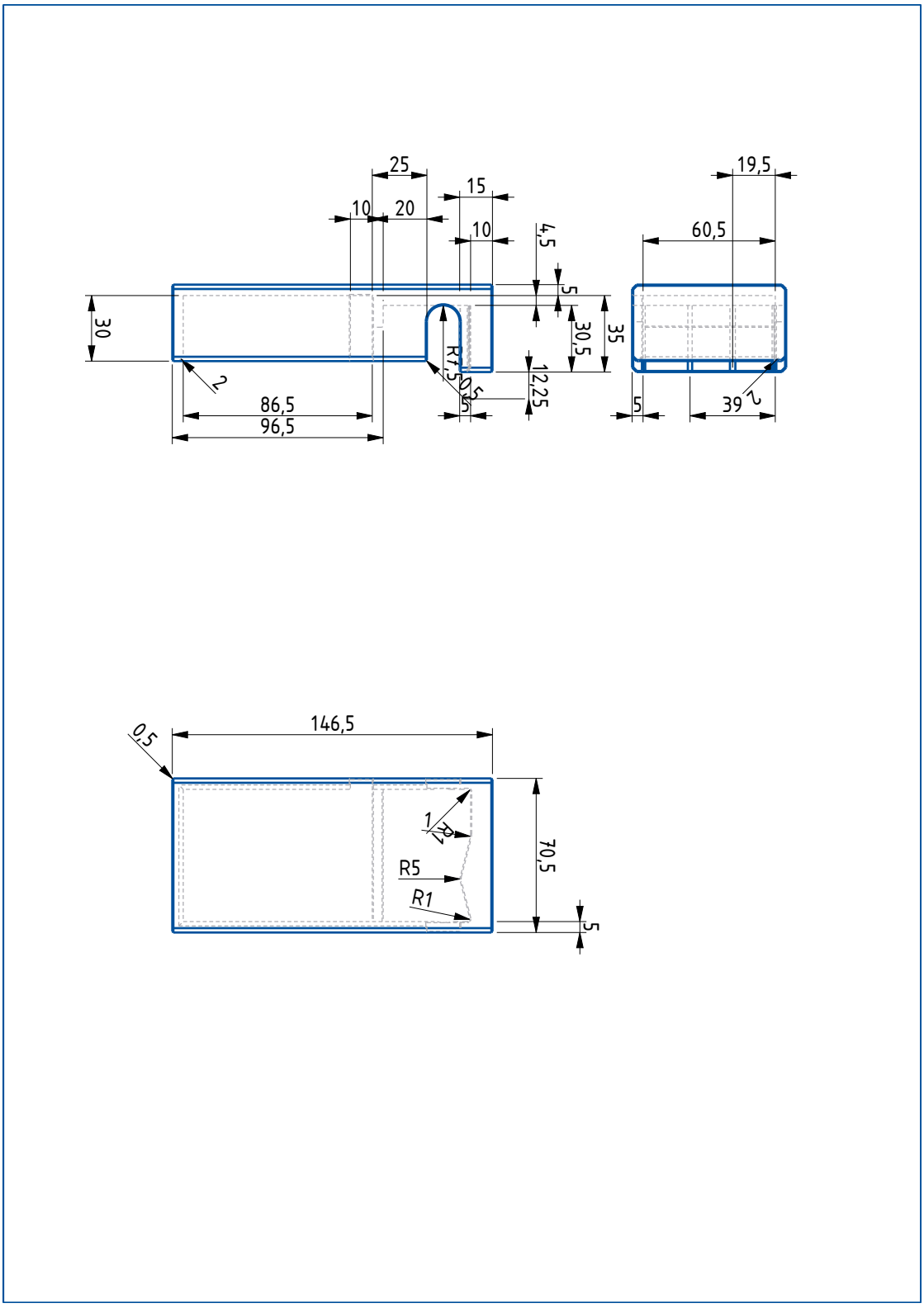

Figure D.1: Technical drawing of the 3D printed case of the resistor in mm.

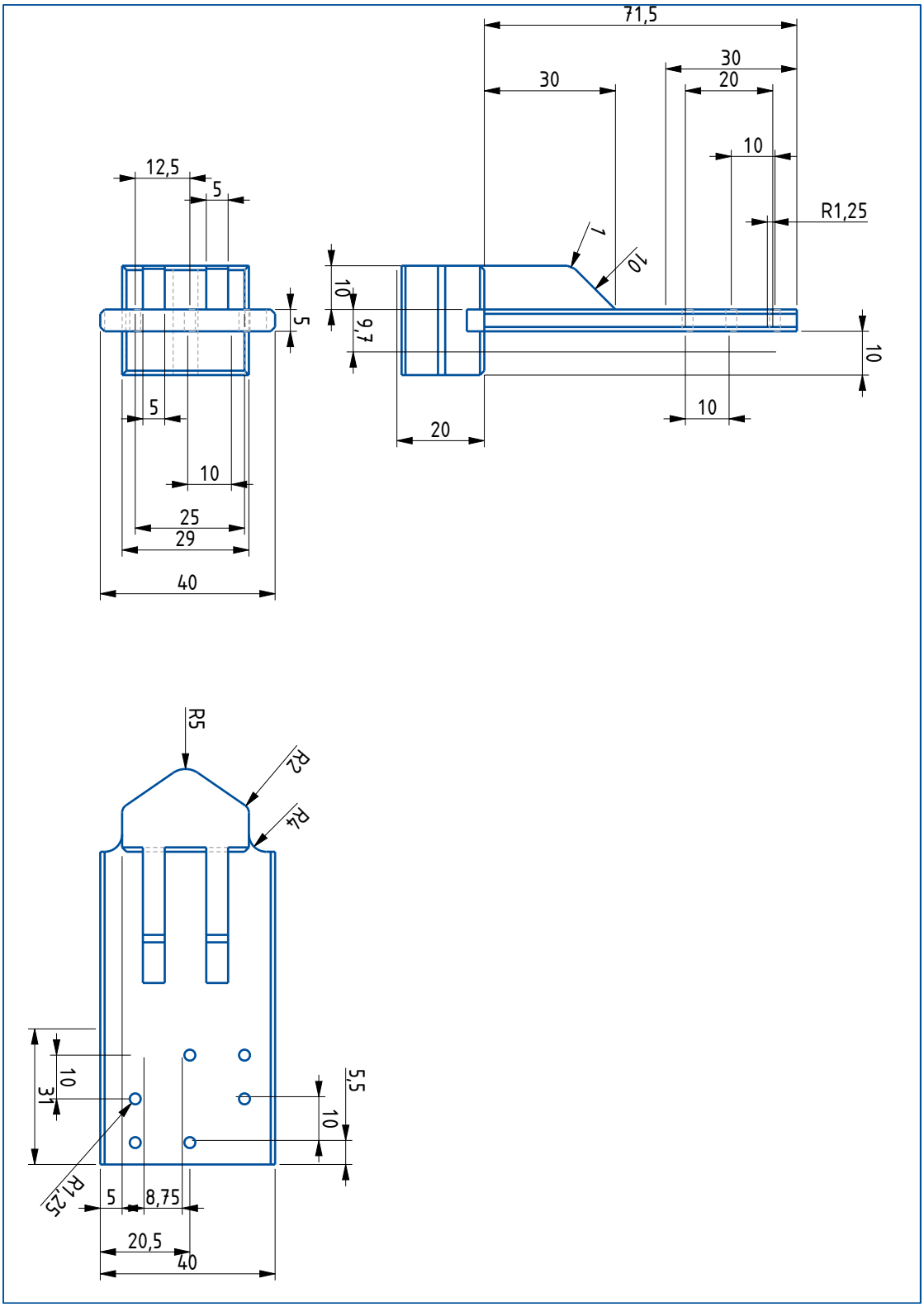

Figure D.2: Technical drawing of the 3D printed pusher of the resistor in mm.

Appendix E

Flowchart Control of the Resistor under Pulsatile Flow

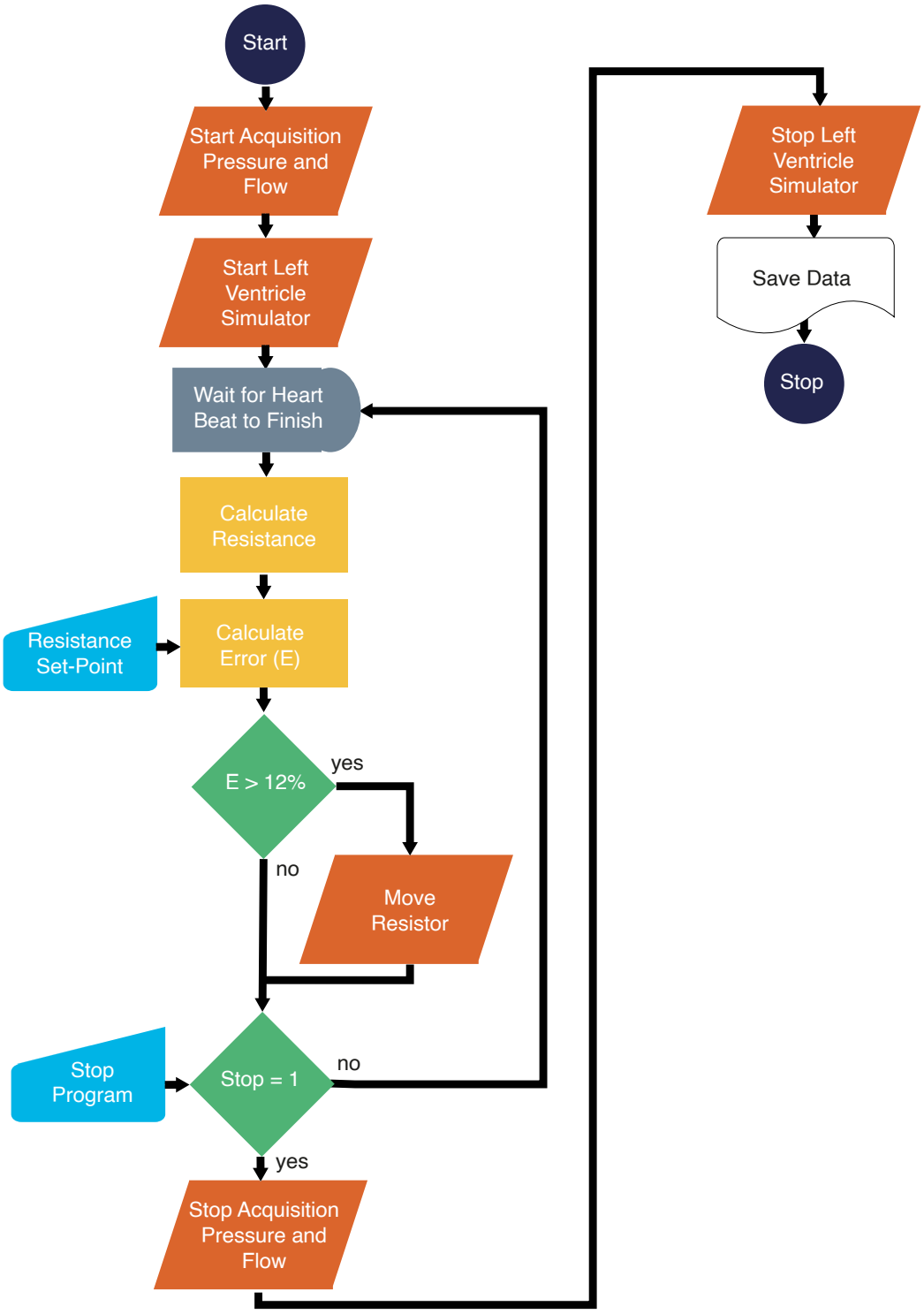

Figure E.1: Flowchart 3

Appendix F

LabVIEW: the Resistor

Sub VI: Resistor moves to set position

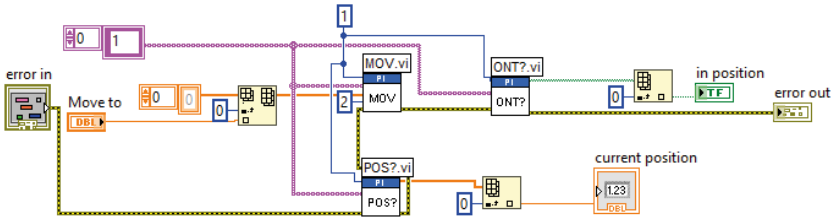

Sub VI: Determine what position the resistor needs to move to

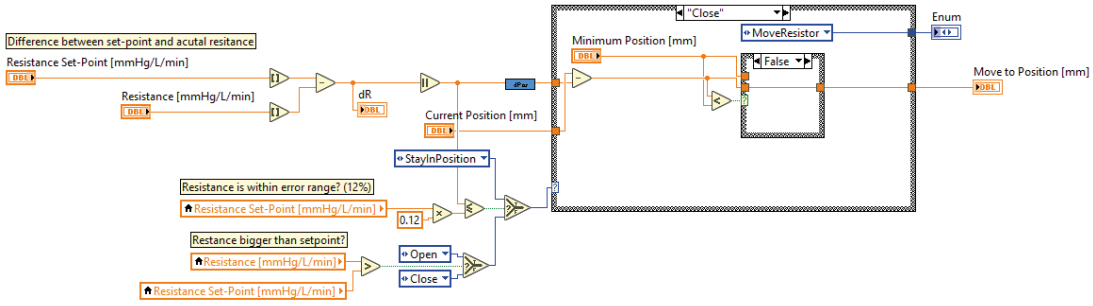

Sub VI: Determine what position the resistor needs to move to

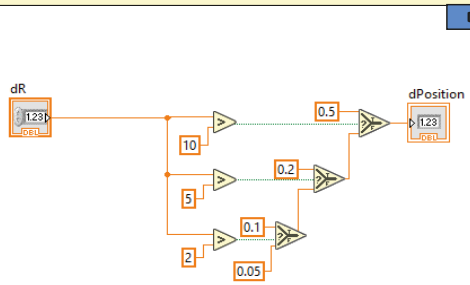

Sub VI: Resistor Current Position